Journal of Materials Chemistry A

REVIEW

View Article Online
View Journal | View Issue

Cite this: J. Mater. Chem. A, 2018, 6, 8159

Sb-based electrode materials for rechargeable batteries

Zhiming Liu, Taeseup Song * and Ungyu Paik *

The demand for green energy conversion and storage for various applications, such as portable electronics, electric vehicles, and large-scale power stations, has boosted the exploration of advanced energy storage technologies. Lithium-ion batteries (LIBs), sodium-ion batteries (SIBs), and liquid-metal batteries (LMBs) meet the different requirements of high-energy density, low cost, and large-scale energy storage, respectively. Currently, designing and synthesizing appropriate electrode materials with high performance, abundant natural availability, and low cost are the main challenges for rechargeable battery technology. Recent studies have demonstrated that Sb-based materials are promising electrode candidates for LIBs, SIBs, and LMBs because of their relatively low cost and high electrochemical performance. This review critically presents recent developments in Sb-based electrode materials, including storage mechanisms, synthesis strategies, and applications in LIBs, SIBs, and LMBs. It also presents challenges and prospects on further improving Sb-based electrode materials for real applications.

Received 23rd February 2018
Accepted 4th April 2018

DOI: 10.1039/c8ta01782d

rsc.li/materials-a

1. Introduction

Renewable energy conversion and storage have become key issues as concerns have grown about pollution and the end of fossil fuel availability. To meet the different demands for energy storage, various energy storage devices such as lithium (sodium)-ion batteries, liquid-metal batteries, and metal–air batteries have been designed and studied.[1–7] Among these candidates, lithium-ion batteries (LIBs) have penetrated many aspects of daily life since their first commercialization in 1991, and their applications have expanded from portable electronics to electric vehicles because of their high energy density.[1,2] Recently, the expectation of large-scale market penetration has raised significant concern about the high cost and limitations of lithium resources. Sodium-ion batteries (SIBs) have attracted increasing attention as a viable alternative to LIBs in light of the natural abundance of sodium and their low-voltage operation.[3,4,8] Given the similar atomic features of lithium ions and sodium ions (except for their atomic radius), the same electrode materials can be applied in both LIBs and SIBs, which has been verified by previous reports.[9–12]

LIBs have been commercialized for almost 30 years. However, the most commonly used graphite and lithium cobalt oxides ($LiCoO_2$), which have been applied as the anode and cathode materials for commercial rechargeable LIBs, cannot meet requirements for higher output capacity because of their

Department of Energy Engineering, Hanyang University, 222 Wangsimni-ro, Seongdong-gu, Seoul, 04763, Korea. E-mail: tssong@hanyang.ac.kr; upaik@hanyang.ac.kr

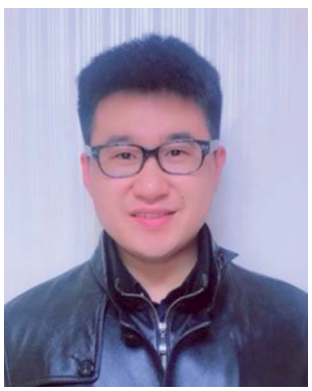

Zhiming Liu received his B. S. Degree from the Department of Materials Science and Engineering at the Harbin Institute of Technology (HIT) in 2012. He is presently a Ph.D. candidate in the Department of Energy Engineering at Hanyang University, Korea, under the supervision of Professor Taeseup Song. His research focuses on the design and synthesis of nanostructured materials and their applications in energy storage devices.

Taeseup Song received his Ph.D. degree from the Department of Materials Science and Engineering at Hanyang University, Korea in 2012. He joined Hanyang University as an assistant professor in 2017. His research interest is mainly focused on the synthesis of nanostructured materials for energy device applications.

relatively low theoretical capacities of 372 and 274 mA h g^{-1}, respectively.[13,14] SIBs remain in the experimental stage; no one has yet found the right electrode materials for practical application. Therefore, designing and synthesizing appropriate electrode materials with high energy density, long and stable cycling life, and suitable working potential is a primary challenge currently facing both LIBs and SIBs. Unremitting efforts have been devoted to discovering new high-performance electrode materials, such as carbonaceous materials, alloy materials, metal oxides, and metal sulfides.[15–24] Among these materials, metallic antimony (Sb) and Sb-based materials (alloys, sulfides, oxides, and their composites) have attracted tremendous attention recently and show great potential as electrode materials due to their relatively low prices and high reversible capacities between 400 and 800 mA h g^{-1} over numerous cycles of lithiation or sodiation.[25–30] For instance, Wang's group synthesized a yolk–shell structured Sb@C anode material for SIBs that showed a 92% capacity retention of 510 mA h g^{-1} over 200 cycles.[31] Li and his colleagues developed a porous-nickel-supported SnSb alloy that demonstrated a high specific capacity and good cyclability for both LIBs and SIBs.[32] It retained 580 mA h g^{-1} after 100 cycles at a high current density of 2 A g^{-1} in LIBs. Zhou *et al.* even reported a Sb_6O_{13}/graphene composite with an ultrahigh capacity of 1090 mA h g^{-1} after 140 cycles.[33]

Nevertheless, most Sb-based electrode materials suffer from large volume expansion after full lithiation or sodiation, which eventually pulverizes the active material and electrically isolates it from the current collector, consequently diminishing cycle stability.[9,34,35] To alleviate these problems, a range of Sb-based materials with different components and structures has been designed and prepared.[29,36–40] Generally, materials with nanoscale structures can alleviate the mechanical stress caused by large volume changes during repeated charging/discharging processes and enhance the reaction kinetics by reducing the transport length for electrons and shortening the diffusion path of ions, thereby improving the electrochemical performance.[16,41] He and co-workers fabricated Sb nanocrystals (NCs) with an average size of 20 nm, which improved the lithium and sodium storage capacities and cycling stability, especially at higher rates of charge and discharge.[36] Zn_4Sb_3 intermetallic nanowires (NWs) synthesized by Yassar's group displayed about 161% volume expansion after the first sodiation and then cycled with an 83% reversible volume expansion.[42] Despite their massive expansion, the nanowires could be cycled without any cracking or fracture during ultrafast sodiation/desodiation processes.

Combining Sb-based materials with buffers, such as carbonaceous materials, is another effective strategy to enhance their electrochemical properties.[28,43–46] Carbon not only acts as a buffer to mitigate pulverization, but also works as a conductive matrix during cycling. Yu *et al.* reported an Sb_2S_3/graphene composite that had a high capacity of 730 mA h g^{-1} at 50 mA g^{-1}, an excellent rate capability up to 6C, and good cycle performance.[47] Sb nanoparticles encapsulated in 1D N-doped porous carbon synthesized by Qian's group exhibited a high reversible capacity of 556 mA h g^{-1} at 200 mA g^{-1} after 100 cycles for LIBs and a reversible capacity of 400.9 mA h g^{-1} at 100 mA g^{-1} after 100 cycles for SIBs.[10] Meanwhile, researchers applying advanced characterization techniques such as *in situ* transmission electron microscopy (TEM), *in situ* X-ray diffraction (XRD), and first-principles calculations have published many new findings related to Li/Na-ion storage mechanisms in Sb-based electrode materials, including phase transformation, morphological evolution, the relationship between the structure and electrochemical performance, and kinetics, providing a theoretical basis for a rational design of high-performance Sb-based electrode materials for LIBs and SIBs.[28,31,35,42]

Recently, several review articles have considered different kinds of electrode materials for rechargeable batteries, one of which focused on Sb-based intermetallic compounds as anode materials.[9] However, to the best of our knowledge, no specific review has yet focused on the preparation and application of all kinds of Sb-based electrode materials for LIBs and SIBs. Therefore, we here consider the development of all Sb-based electrode materials for LIBs and SIBs including the storage mechanisms, the rational design strategies, and the electrochemical properties. In addition, we present the main issues and likely solutions and future prospects of Sb-based materials as potential electrode candidates.

Besides LIBs and SIBs, Sb has also been widely studied as a positive electrode material for liquid-metal batteries (LMBs) in recent years. LMBs, as a new battery technology, have shown their potential commercial application in large-scale energy storage systems because of their low cost, ultra-long cycle life, and facile cell fabrication.[7,48] Nevertheless, the high working temperature and low output voltage make LMBs significantly challenging on the road to viable energy storage devices. In light of the high open circuit voltage (OCV), relatively low operating temperature, and moderate price, Sb and some of its alloys have been considered as candidate electrodes for LMBs.[48,49] Therefore, we also briefly introduce the working mechanism of LMBs and recent developments in Sb-based LMBs in a later section of this review.

Ungyu Paik is a distinguished professor of the Department of Energy Engineering at Hanyang University, Korea. He received his Ph.D. degree from the Department of Ceramic Engineering at Clemson University in 1991. Prior to starting his professor position at Hanyang University in 1999, he conducted postdoctoral research at the National Institute of Standards and Technology, USA and was an assistant professor at Changwon National University, Korea. He published about 330 papers regarding nanoparticle patterning technology, inorganic–organic hybrid electronics and energy storage devices.

2. Li/Na-ion storage mechanism

A typical illustration of the reaction mechanisms for various kinds of Sb-based electrode materials is shown in Fig. 1. As can be observed, the sodiation/desodiation processes mainly contain two kinds of reactions: alloying and conversion.[28,35,42,50–53] Unlike intercalation-based anodes, in which the original crystalline structure remains unchanged after lithiation or sodiation, phase transition and structural evolution occur during both alloying and conversion reactions, forming new crystalline phases through the rearrangement of atoms. As a consequence, large volume expansion often occurs during lithiation and sodiation. Sb-based active materials show almost the same storage mechanisms in LIBs and SIBs; here, SIBs are chosen as the representative to facilitate the understanding of this scheme.

2.1 Li/Na-ion storage mechanisms in metallic Sb/Sb-based alloys

The insertion of Li^+/Na^+ ions into metallic Sb follows an alloying reaction that eventually forms Li_xSb or Na_xSb alloys.[31,35,54] The typical reaction of Sb with Na^+ ions is shown in Table 1. Theoretically, one mole of Sb can react with three moles of Na^+ ions and electrons, contributing to a theoretical capacity of 660 mA h g^{-1} with hexagonal Na_3Sb as the final stable phase. Correspondingly, it shows a large volume expansion of 293%.[55] The low puckered-layer structure of Sb and its suitable working voltage of 0.8–0.9 V facilitate the diffusion of Na^+ ions and the release of structural strains, making Sb a potential candidate as an electrode material for high-performance SIBs.[55] Many research groups have studied alloying storage mechanisms for SIBs and LIBs. Darwiche and co-workers found an unexpected electrochemical mechanism in SIBs by applying an *in situ* XRD technique.[35] They pointed out that bulk Sb experienced slightly different storage mechanisms in LIBs and SIBs. Fig. 2a and b present the representative voltage profiles of bulk Sb electrodes in SIBs and LIBs. For LIBs, the initial lithiation occurred at a single plateau of 0.8 V *vs.* Li^+/Li, which characterized the two phase transitions Sb into Li_2Sb and Li_2Sb into Li_3Sb (Fig. 2b). In the delithiation process, Li_3Sb directly converted back to crystalline Sb at a single voltage plateau of 1.05 V. The same lithium storage mechanism occurred in the subsequent charge and discharge processes. For SIBs, the first sodiation occurred at a single long plateau of 0.45 V *vs.* Na^+/Na, which indicated the alloying reaction from the crystalline Sb to hexagonal Na_3Sb (Fig. 2a). The long voltage plateau at 0.8 V upon desodiation represented an irreversible dealloying process from hexagonal Na_3Sb to amorphous Sb. In the second sodiation process, three distinct plateaus centered at 0.72, 0.55, and 0.50 V

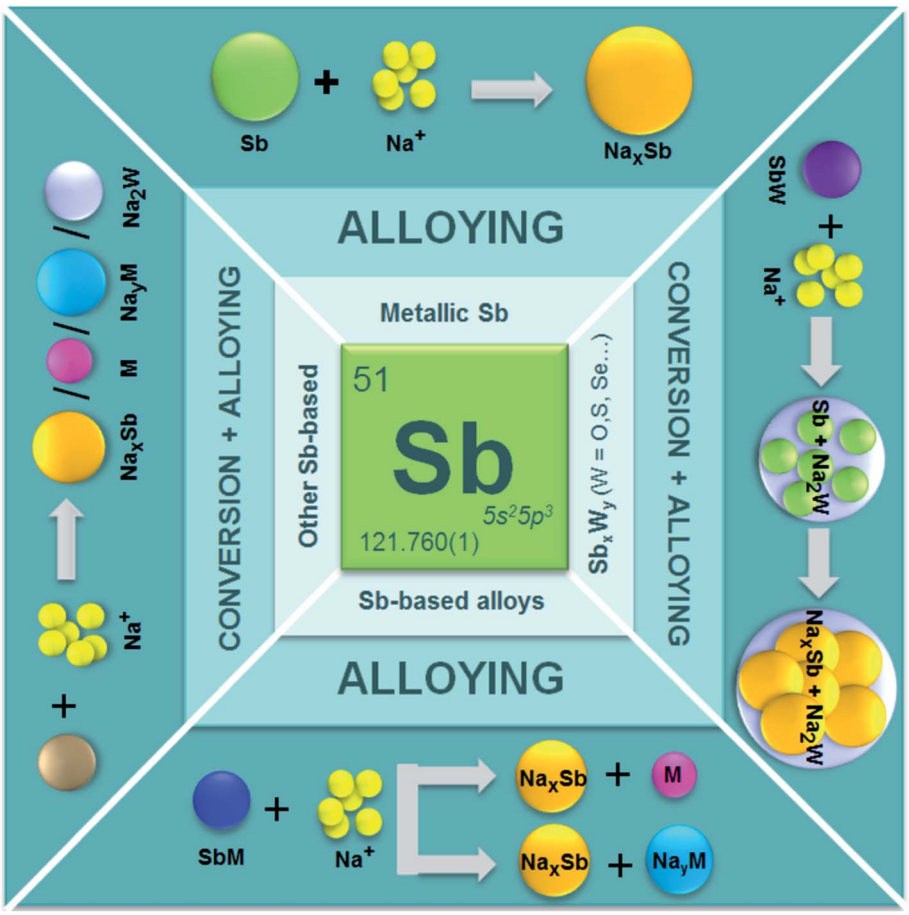

Fig. 1 Na storage mechanisms for different types of Sb-based electrode materials.

Table 1 Na-storage reactions of some typical Sb-based electrode materials

Typical materials	Possible Na-storage reactions	Gravimetric capacity [mA h g^{-1}]	Ref.
Sb	$Sb + 3Na^+ + 3e^- \rightarrow Na_3Sb$	660	35
SnSb	$SnSb + 6.75Na^+ + 6.75e^- \rightarrow Na_{3.75}Sn + Na_3Sb$	753	64
NiSb	$NiSb + 3Na^+ + 3e^- \rightarrow Na_3Sb + Ni$	446	65
Sb_2O_3	$Sb_2O_3 + 12Na^+ + 12e^- \rightarrow 2Na_3Sb + 3Na_2O$	1103	66
Sb_2S_3	$Sb_2S_3 + 12Na^+ + 12e^- \rightarrow 2Na_3Sb + 3Na_2S$	947	47

corresponded to a multistep sodiation process from amorphous Sb to hexagonal Na_3Sb with an amorphous phase Na_xSb as the intermediate. The subsequent cycles exhibited the same mechanism as the first charge and second discharge. Compared to LIBs, an intermediate amorphous phase (Na_xSb) formed upon sodiation, which might act as a buffer to relieve strain, accounting for improved cycling performance in SIBs. Mitlin's group used an *in situ* TEM technique to further confirm the formation of intermediate amorphous Na_xSb and fully sodiated Na_3Sb.[56] Moreover, they calculated a change in volume of 269%, which was less than the theoretical value of 293%. This slight difference was supposed to be the failure of Sb to reach full sodiation. Baggetto *et al.* reported that cubic Li_3Sb and hexagonal Li_3Sb coexist at full lithiation, with the former being predominant.[54] The coexistence of these polymorphs was consistent with their predicted voltages calculated from density functional theory (DFT). Despite the different discharge processes, metallic Sb experiences three electron reactions in both LIBs and SIBs, producing polymorph Li_3Sb and Na_3Sb as the fully lithiated and sodiated products, respectively.

Similarly, Sb-based intermetallic compounds also follow an alloying reaction mechanism, with large volume expansion occurring during the discharge process in LIBs and SIBs. According to the activity of the partner elements with Li^+/Na^+ ions, Sb-based alloys are divided into two categories: active–active and active–inactive alloys. The partner elements Sn, Bi, and Ge are the active–active type; both elements can alloy with Li^+ or Na^+ ions.[57–59] Active–inactive alloys contain electrochemically inert metal elements such as Ni, Cu, Co, Al, Fe, or Mo.[51,60–63] The active–active Sb-based intermetallics usually exhibit higher specific capacities than active–inactive ones because both elements can contribute to the overall capacity. Also, both metal elements can act as buffer materials to alleviate volume expansion. The SnSb alloy is a typical active–active type. The theoretical maximum capacity for sodium storage in SnSb is 752 mA h g^{-1} based on the fully sodiated products of Na_3Sb

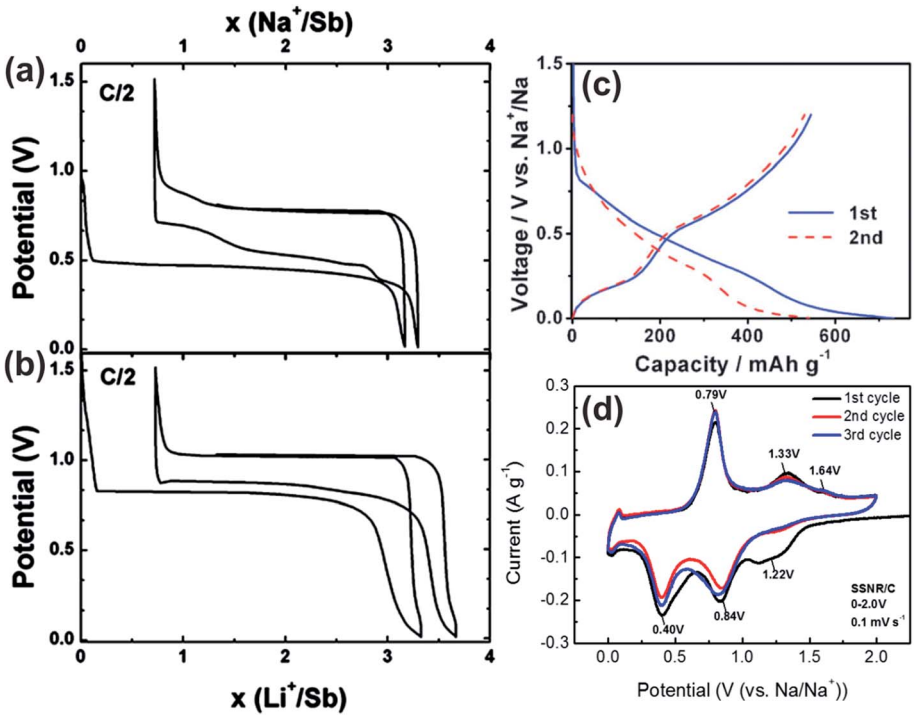

Fig. 2 Voltage profiles of bulk Sb in (a) SIBs and (b) LIBs cycled at C/2 rate between 0.02 and 1.5 V. Reproduced with permission.[35] Copyright 2012, American Chemical Society. (c) The initial two discharge/charge profiles of the SnSb electrode between 0.0 and 1.2 V at a current rate of 100 mA g^{-1}. Reproduced with permission.[64] Copyright 2012, Royal Society of Chemistry. (d) CV curves of a Sb_2S_3 electrode scanned at 0.1 mV s^{-1}. Reproduced with permission.[68] Copyright 2017, Wiley.

and $Na_{3.75}Sn$.[64] Fig. 2c shows the voltage profiles of the SnSb alloy electrode material. The plateaus at 0.45 V in discharge and 0.58 V in charge corresponded to the Na–SnSb alloying–dealloying processes to form Na_3Sb and metallic Sn, respectively. In addition, the plateaus at 0.05 V in discharge and 0.17 V in charge mainly resulted from the Na–Sn alloying–dealloying processes and the electrochemical reactions between Na^+ ions and super P carbon. In the active–inactive type, the intermetallic normally transforms into a composite of Sb and an inert metal after the initial cycle. The electrochemically inert metal acts as a mechanical buffer to alleviate the volume changes during cycling and enhances the electrical conductivity of the battery system. For instance, the NiSb alloy transform into $Na_{3.75}Sb$ and metallic Ni after the initial sodiation, and the Ni functions as both a buffer material and a conducting agent.[65] However, active–inactive Sb-based alloys always show relatively low theoretical capacity because the inert elements contribute little to sodium storage.

2.2 Li/Na-ion storage mechanisms in Sb_xW_y (W = O, S, Se…)

Sb_xW_y active materials mainly include antimony oxides, antimony sulfides, antimony selenide, and antimony nitride, in which both the conversion and alloying reactions occur.[47,53,66,67] A possible conversion reaction and associated alloying reaction are shown in eqn (2.1) and (2.2), respectively:

$$Sb_xW_y + zNa^+ \rightarrow xSb + yNa_{z/y}W \quad (2.1)$$

$$xSb + 3xNa^+ \rightarrow xNa_3Sb \quad (2.2)$$

Metallic Sb forms in the initial conversion reaction and further reacts with Na^+ ions to form the final product of Na_3Sb dispersed in a matrix of $Na_{z/y}W$. Generally, both the conversion and alloying reactions that occur during the sodiation process contribute to a high capacity and a large volume expansion. Table 1 gives the sodiation reaction equations for Sb_2O_3 and Sb_2S_3, which show theoretical capacities of 1103 and 947 mA h g^{-1}, respectively.

Yao and co-workers investigated the sodiation reaction mechanisms of Sb_2S_3 by applying an *in situ* TEM technique and first-principles calculations.[68] They found an anomalous Na-ion storage mechanism: an intercalation reaction initially occurred at 1.22 V, with Na^+ ions inserting themselves into the Sb_2S_3 crystals at an ultrafast speed during the first sodiation process (Fig. 2d). The resulting amorphous $Na_xSb_2S_3$ intermediate phase experienced sequential conversion (0.84 V) and alloying reactions (0.40 V) to form crystalline Na_2S, Na_3Sb, and minor metallic Sb. Upon desodiation, the Na^+ ions extracted from the nanocrystalline phases left behind fully desodiated Sb_2S_3 in an amorphous state. The three main anodic peaks at 0.79, 1.33, and 1.64 V characterized the reversible formation of Sb, Sb_2S_3, and extraction of Na^+ ions from the layered structure, respectively. The corresponding reaction equations are as follows:

$$Sb_2S_3 + xNa^+ + xe^- \rightarrow Na_xSb_2S_3\ (x < 12) \quad (2.3)$$

$$Na_xSb_2S_3 + (12 - x)Na^+ + (12 - x)e^- \leftrightarrow 2Na_3Sb + 3Na_2S \quad (2.4)$$

Other complex Sb-based compounds have also been reported as electrode materials for LIBs and SIBs, including $Ni_3Sb_4O_6F_6$ and $Mn_2Sb_3O_6Cl$.[52,69] Although the charging/discharging reactions are more complicated than those described above, the Li/Na-ion storage mechanisms are still composed of basic conversion and alloying reactions.

3. Synthetic strategies for preparing Sb-based electrode materials

Recently, many different methods have been reported for synthesizing Sb-based electrode materials with various morphologies and structures at the micro- and nanoscales. In this section, we review several typical strategies.

3.1 Hydrothermal/solvothermal methods

As a cost-efficient and environmentally benign strategy, hydrothermal/solvothermal reactions have become the most frequently used approach for synthesizing nanostructured materials with high crystallinity, high phase purity, and narrow particle size distributions under the conditions of high pressure and moderate temperature.[70] Generally speaking, hydrothermal/solvothermal methods are pressure-dependent, temperature-dependent, and time-dependent after the precursors and solvents are mixed. Many Sb-based electrode materials with desirable micro- or nanostructures and unique morphologies have been prepared using these methods, including Sb@C microspheres, Sb_2Se_3 nanowires, and a 3D porous Sb_2S_5-graphene architecture.[28,67,71–76]

Ji's group synthesized rod-like Sb_2S_3 anode materials using the solvothermal method.[77] A possible formation process for the Sb_2S_3 rods is depicted in Fig. 3a. An Sb–thiourea complex is initially formed when a thiourea solution is added to an $SbCl_3$ solution. During the heating process, the chelation of Sb–thiourea is weakened, and Sb^{3+} is gradually released. Simultaneously, the thiourea is broken, and S^{2-} is slowly released and reacts with the Sb^{3+} to form amorphous $(Sb_2S_3)_n$ particles. Under the high-pressure and high-temperature conditions of the solvothermal process, the amorphous Sb_2S_3 particles undergo nucleation, anisotropic growth, and recrystallization, eventually forming 1D rod-like structures. These Sb_2S_3 rods were uniform and mono-crystalline. Sb@C microspheres were first synthesized by Cao's group through a facile, self-catalyzing, solvothermal method associated with a carbonization process.[71] Fig. 3b and c reveal the homogeneous encapsulation of Sb nanoparticles (15–20 nm) in C microspheres. Luo *et al.* prepared Sb_2Se_3 ultralong nanowires through a hydrothermal method (Fig. 3d).[67] The as-synthesized nanowires featured an average diameter of 90 nm and a length of up to hundreds of micrometers. After a facile vacuum filtration process, a free-standing Sb_2Se_3 nanowire-based membrane was obtained (Fig. 3e) and used directly as an anode for LIBs/SIBs without any binders or conductive agent. rGO/SnSb nanocomposites were synthesized through a hydrothermal reaction by adding graphene oxide, $SnCl_2$, and $Sb(CH_3COO)_3$ to a hydrothermal solution.[78] TEM images confirm that SnSb nanoparticles with an average size of

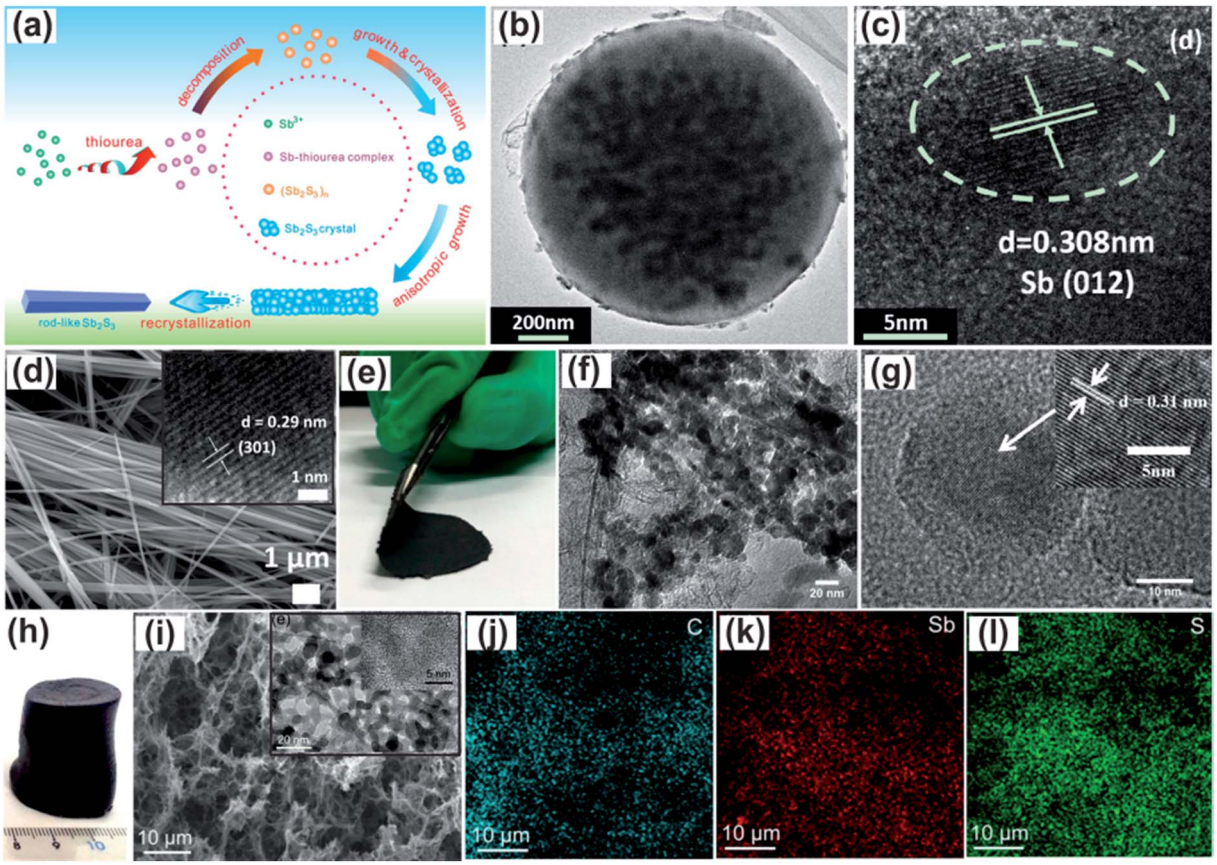

Fig. 3 (a) Schematic illustration of the formation of Sb_2S_3 rods. Reproduced with permission.[77] Copyright 2015, American Chemical Society. (b) TEM and (c) HR-TEM images of Sb@C microspheres. Reproduced with permission.[71] Copyright 2016, American Chemical Society. (d) Scanning electron microscopy (SEM) and high resolution-TEM (HR-TEM) images (inset) of Sb_2Se_3 nanowires. (e) Digital photographs of an Sb_2Se_3 nanowire-based membrane. Reproduced with permission.[67] Copyright 2016, American Chemical Society. (f) TEM and (g) HR-TEM images of rGO–SnSb nanocomposites. Reproduced with permission.[78] Copyright 2015, American Chemical Society. (h) Photograph, (i) SEM and inset TEM, and (j–l) elemental mapping images of an Sb_2S_5–GF composite. Reproduced with permission.[28] Copyright 2015, American Chemical Society.

20–30 nm were uniformly dispersed on the rGO surfaces (Fig. 3f and g). Lu and co-workers reported a facile one-step hydrothermal co-assembly that produced Sb_2S_5 nanoparticles (~5 nm) with a controllable mass ratio uniformly encapsulated in 3D porous graphene foam that could be directly used as a self-supported anode (Fig. 3h and i).[28] Fig. 3i clearly shows that the as-prepared material displayed an interconnected 3D conductive network with an open porous architecture constructed from graphene foam. The inset TEM images reveal that the amorphous Sb_2S_5 nanoparticles with an average size of ~5 nm were uniformly encapsulated within the graphene framework. Energy-dispersive spectrometry (EDS) showed the presence of C, O, Sb, and S in the as-obtained sample (Fig. 3j–l).

3.2 Galvanic replacement

Galvanic replacement has attracted attention as a way to fabricate nanoarchitectured electrode materials because of its simple, low-temperature synthesis process. Liu and colleagues prepared a novel Sb@C nanosphere anode with a biomimetic yolk–shell structure for LIBs and SIBs *via* a nanoconfined galvanic replacement route.[79] Initially, yolk–shelled Sn@C nanospheres were fabricated using a facile hydrothermal method combined with carbon-coating and hydrogen reduction processes. In the subsequent galvanic replacement process, Sn was oxidized to Sn^{4+}, and Sb^{3+} was simultaneously reduced to Sb at 80 °C. During this process, the encapsulated solid Sn cores were chemically transformed into hollow Sb; thus, unique hollow Sb@C yolk–shell spheres were finally obtained (Fig. 4a). The TEM image and corresponding elemental mapping shown in Fig. 4b and c clearly confirm that the hollow Sb yolks were fully encapsulated in thin carbon nanocages. Chen's group synthesized a scalable and binder-free Cu_2Sb/Cu electrode *via* a galvanic replacement reaction.[51] The thickness of the Cu_2Sb formed on Cu foil could be easily tuned by adjusting the concentration of Sb^{3+} and reaction time. In the HR-TEM image in Fig. 4d, the well-developed lattices with a *d*-spacing of 0.21 nm correspond to the (112) facets of the Cu_2Sb phase. The porous Cu_2Sb nanoparticle film and its intrinsic contact with the Cu foil resulted in good electrochemical properties. Yi *et al.* successfully fabricated a novel Sb/C polyhedral composite through a galvanic replacement reaction technique using metal organic frameworks (MOFs) as templates.[80] Fig. 4e and f reveal that the Sb nanoparticles (average size 15 nm) were homogeneously encapsulated into

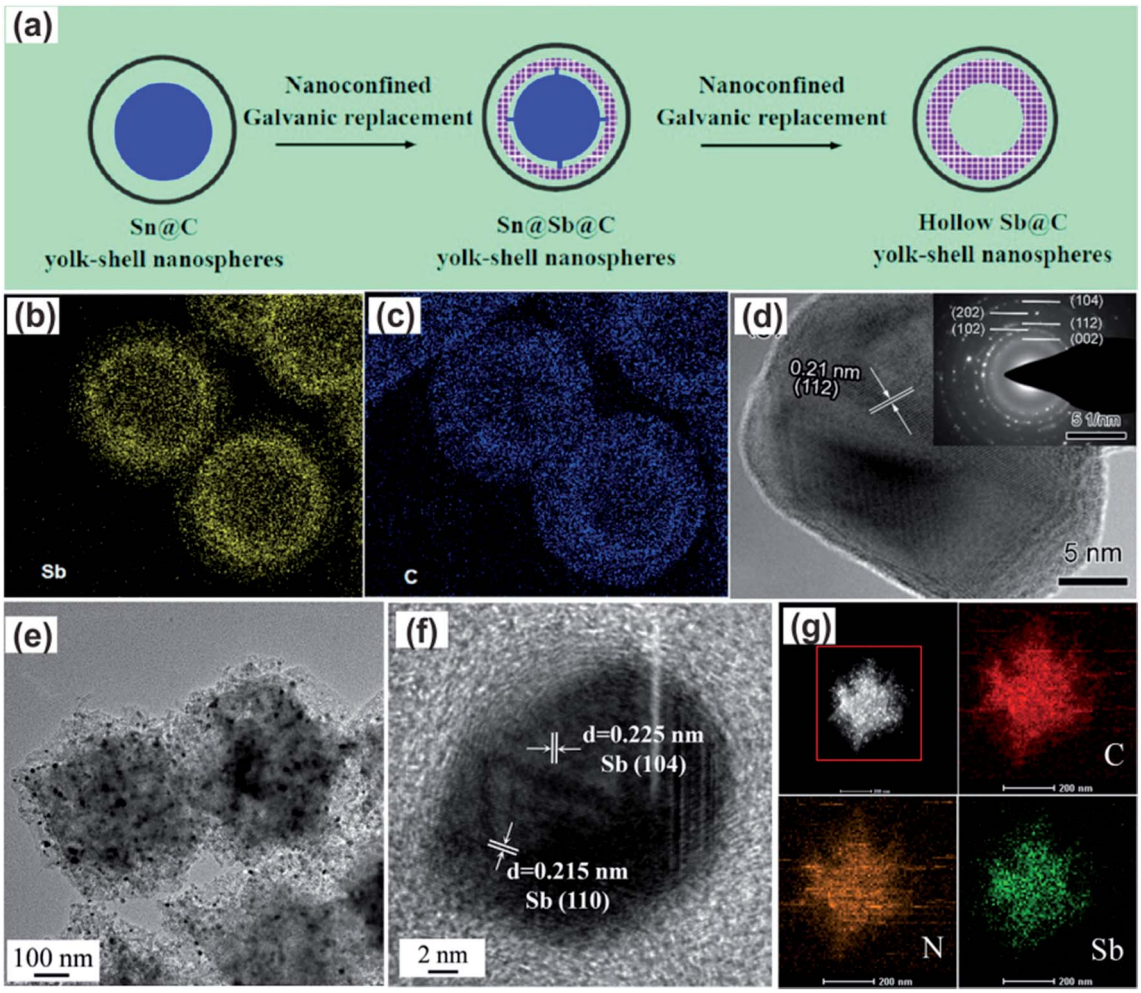

Fig. 4 (a) Schematic evolution of hollow Sb@C yolk–shell nanospheres. (b, c) Elemental mapping images of hollow Sb@C yolk–shell spheres. Reproduced with permission.[79] Copyright 2017, American Chemical Society. (d) HR-TEM image of Cu_2Sb nanoparticle and selected-area electron diffraction pattern (inset). Reproduced with permission.[51] Copyright 2017, American Chemical Society. (e) TEM image, (f) HR-TEM image and (g) EDS mapping of an Sb/C composite. Reproduced with permission.[80] Copyright 2016, Elsevier.

carbon matrixes, forming a hierarchical porous structure of nanosized building blocks. The uniform distribution of C, N, and Sb in the EDS mapping further confirms the highly distributed structure of the Sb/C composite (Fig. 4g).

Sb hollow nanospheres,[81] MOF-derived NiSb embedded in carbon hollow spheres,[60] rGO–Sb–Ni with a sandwiched structure,[82] and some other Sb-based electrode materials with unique structures and morphologies have also been successfully prepared using moderate galvanic replacement.[65]

3.3 High energy mechanical milling

The high energy mechanical milling (HEMM) technique is another efficient strategy for synthesizing Sb-based electrode materials due to its facile procedure and large-scale production.[83–92] In the HEMM process, the precursors react with one another through highly energetic collisions generated by the movements of tiny balls under high pressure at high temperature.

Sb–MO_x–C (M = Al, Ti, and Mo) nanocomposites have been synthesized through a mechanochemical reduction of Sb_2O_3 with, respectively, Al, Ti, and Mo, in the presence of carbon (acetylene black).[83] A schematic illustration of the facile synthesis process is shown in Fig. 5a. TEM images (Fig. 5b) revealed that these nanocomposites were composed of uniformly dispersed nanostructured antimony in an amorphous Al_2O_3, TiO_2, or MoO_3 matrix, along with conductive carbon. Park and Sohn applied the HEMM method to transform micro-sized Sn and Sb powders into 10 nm SnSb crystallites.[93] These nanocrystallites were uniformly distributed in an amorphous carbon matrix, resulting in a SnSb/C nanocomposite structure (Fig. 5c). Lee *et al.* introduced S powder into precursors and synthesized a CoSbS/C nanocomposite by HEMM associated with a heat treatment process (Fig. 5d).[94] The HR-TEM image in Fig. 5e indicates the presence of 5–10 nm CoSbS nanocrystallites in an amorphous carbon matrix.

3.4 Sintering and heat treatment

As one of the most commonly used synthesis methods, sintering and heat treatment are usually associated with other

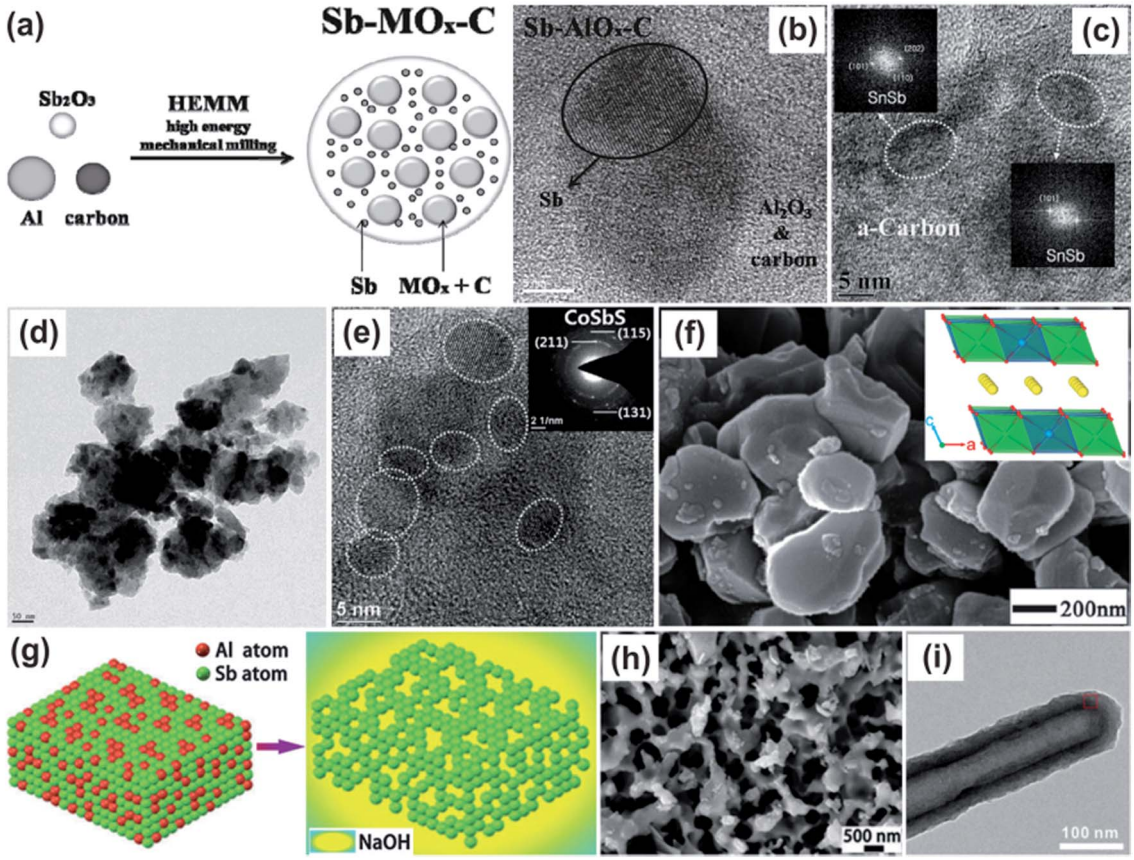

Fig. 5 (a) Schematic description and (b) HR-TEM image of Sb–AlO_x–C nanocomposites. Reproduced with permission.[83] Copyright 2009, American Chemical Society. (c) HR-TEM image with the corresponding lattice spacing of an SnSb/C nanocomposite. Reproduced with permission.[93] Copyright 2009, Elsevier. (d) Bright-field TEM and (e) HR-TEM images of a CoSbS/C nanocomposite. Reproduced with permission.[94] Copyright 2013, Elsevier. (f) SEM image of the as-prepared O3-$Na_3Ni_2SbO_6$ and projections of its structure along the [010] direction (inset). Reproduced with permission.[105] Copyright 2014, Wiley. (g) Schematic of the evolution of the NP-Sb structure *via* chemical dealloying. (h) SEM image of the NP-Sb structure. Reproduced with permission.[38] Copyright 2016, Royal Society of Chemistry. (i) TEM image of a Sb@C coaxial nanotube. Reproduced with permission.[106] Copyright 2016, Royal Society of Chemistry.

procedures, such as hydrothermal/solvothermal processes and HEMM, to further deal with intermediate processes such as carbonization and increase of crystallinity. Many high-performance Sb-based electrode materials have been obtained using heat treatment procedures.[44,52,95–104]

Yang's group prepared a honeycomb-layered $Na_3Ni_2SbO_6$ cathode material *via* a solid-state reaction by simply heating a stoichiometric amount of a Na_2CO_3, Sb_2O_3, and NiO mixture at 900 °C for 12 h.[105] The resulting O3-$Na_3Ni_2SbO_6$ powder consisted of well-dispersed sub-microparticles with an irregular morphology (Fig. 5f). The inset molecular structure revealed that each SbO_6 octahedron was surrounded by six NiO_6 edge-sharing octahedrons to form a superstructure lattice that hosted the Na^+ ions in-between the $NiSbO_6$ slabs. Liu and co-workers synthesized a nanoporous (NP) antimony anode material by heating precursors associated with a dealloying process.[38] A schematic of the evolution of the nanoporous Sb structure is shown in Fig. 5g. Initially, an Al–Sb alloy precursor was prepared by high-frequency induction heat treatment, and it was then immersed into a 20 wt% NaOH aqueous solution at 60 °C to remove the Al atoms. Fig. 5h displays SEM images of the obtained coral-like nanoporous Sb. By adjusting the ratio of Al to Sb, honeycomb-like nanoporous Sb and Sb particles with different sizes were also prepared. Paik's group developed a facile carbon-coating process coupled with a thermal-reduction strategy to synthesize Sb@C coaxial nanotubes.[106] With different annealing times, the hollow space and amount of Sb inside the tube could be easily tuned by the partial evaporation of Sb. The TEM image of an Sb@C nanotube with a heating time of 5 min displayed in Fig. 5i clearly reveals the nanotube structure with a diameter of around 120 nm.

3.5 Electrodeposition

Electrodeposition, as an important synthesis technique, has also been applied to fabricate Sb-based electrode materials with various nanostructures.[37,107–116] Bryngelsson *et al.* synthesized a pure Sb coating, Sb/Sb_2O_3 coating, and Sb_2O_3 coating by adjusting the amounts of HCl and NaOH in the electrolyte during electrodeposition.[117] Fig. 6a indicates that Sb particles obtained in the presence of HCl were larger than particles obtained in the absence of HCl. Janek's group reported high-

aspect-ratio antimony nanowires at room temperature using a template-free electrodeposition strategy (Fig. 6b).[37] The nanowires with diameters around 30 nm and lengths up to several tens of micrometers were of high quality and grew densely on different substrates such as copper and glassy carbon. Hierarchical fern-leaf-like Sb was successfully fabricated *via* a simple and cost-effective electrochemical deposition method (Fig. 6c).[118] Morphological and structural characterization showed that the as-prepared Sb had a uniform fern-leaf-like structure composed of well-crystallized Sb nanoparticles.

Lee *et al.* realized a compositionally gradational heterostructure composed of a Ni core, NiSb interface, and attached Sb crystals (3D Sb/NiSb/Ni) *via* pulsed electrodeposition under controlled conditions.[119] Fig. 6d illustrates the fabrication process of the 3D Sb/NiSb/Ni electrodes. 3D Ni rod arrays were initially prepared *via* pulsed electrodeposition using a Ni foil, AAO membrane, filter paper, and Ni foil stack. The Sb nanocrystals were subsequently electrodeposited in a Sb–citrate-complex solution under the controlled mass flux of the Sb–citrate complex. The NiSb interfaces were formed by *in situ* interfacial alloying between the Ni and Sb. HR-TEM images confirm the existence of the NiSb and Sb phases (Fig. 6e and f). Fig. 6g and h show the dark-field image, line-scan profiles, and elemental mapping results of the Sb/NiSb/Ni heterostructure and clearly demonstrate that Sb particles were present on the surface of the NiSb shell. Porous-Ni-scaffolded SnSb anodes were also fabricated using this facile electrodeposition method.[32] The SEM image and elemental mapping in Fig. 6i and j clearly reveal the porous structure and uniform distribution of Sb, Sn, and Ni.

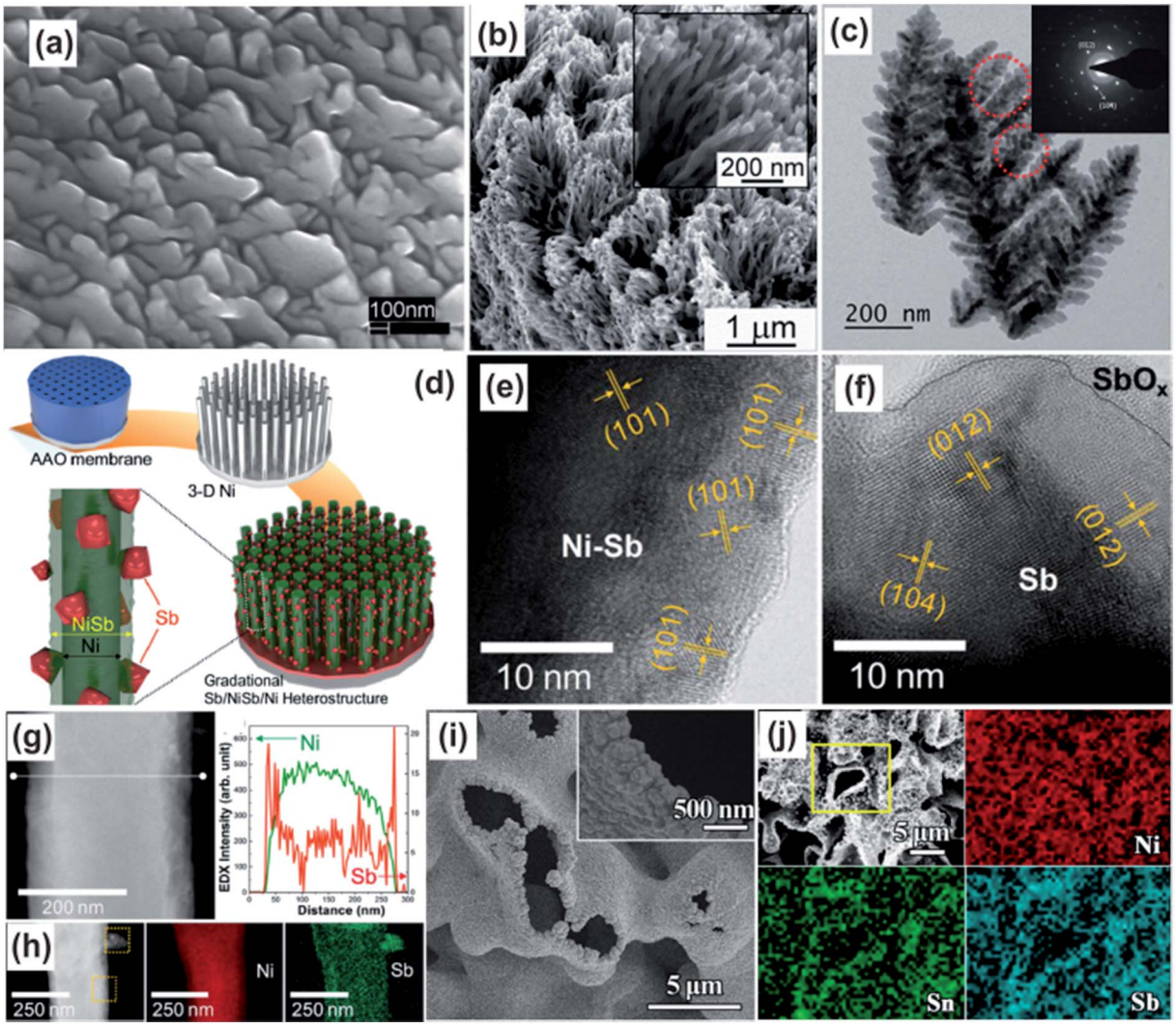

Fig. 6 (a) SEM image of a pure Sb coating deposited in the presence of 0.110 M HCl. Reproduced with permission.[117] Copyright 2007, American Chemical Society. (b) SEM image of Sb nanowires. Reproduced with permission.[39] Copyright 2016, Royal Society of Chemistry. (c) TEM image and selected area electron diffraction (SAED) pattern (inset) of fern leaf-like Sb. Reproduced with permission.[118] Copyright 2017, Royal Society of Chemistry. (d) Fabrication process of 3D Sb/NiSb/Ni electrodes. HR-TEM images of (e) Sb particles and (f) NiSb shell. (g) High-angle annular dark-field (HAADF) image and line scan profiles and (h) scanning transmission electron microscopy-energy dispersive X-ray spectra (STEM-EDS) mapping of the Sb/NiSb/Ni heterostructure. Reproduced with permission.[119] Copyright 2015, Elsevier. (i) SEM image and (j) elemental mapping of PNS@SnSb. Reproduced with permission.[32] Copyright 2017, American Chemical Society.

3.6 Other conventional methods

Other regular methods including solution chemical reduction, magnetron sputtering, electrospinning, co-precipitation, and chemical vapor deposition (CVD) have also been widely used to fabricate Sb-based electrode materials with advanced nanostructures.

The solution chemical reduction approach is often employed to prepare nanoscale materials with a uniform size distribution.[36,120–127] The applied temperature and pressure are more moderate than those used in hydrothermal/solvothermal processes. He *et al.* reported Sb nanocrystals with a mean size tunable in the 10–20 nm range and narrow size distributions (Fig. 7a).[36] Nithya and Gopukumar synthesized an rGO/nano-Sb composite *via* a solution chemical reduction route.[43] The TEM image in Fig. 7b clearly shows the spherical morphology of the Sb particles, with sizes varying from 10 to 20 nm, on the surface of rGO sheets.

The magnetron sputtering technique is often applied to prepare thin films of metal and semiconductor materials on substrates.[54,56,128–130] Mitlin's group deposited a Sb film on a supported surface of TiN/Ge nanowires using magnetron sputtering from a high-purity elemental target.[56] All depositions were conducted at room temperature as the substrate was continuously rotated. The TEM image in Fig. 7c and XEDS line scan in Fig. 7d reveal that the overall thickness and morphology of the Sb film were uniform along the length of the wire.

Electrospinning has been widely used as a facile and versatile strategy for preparing 1D nanomaterials with controllable

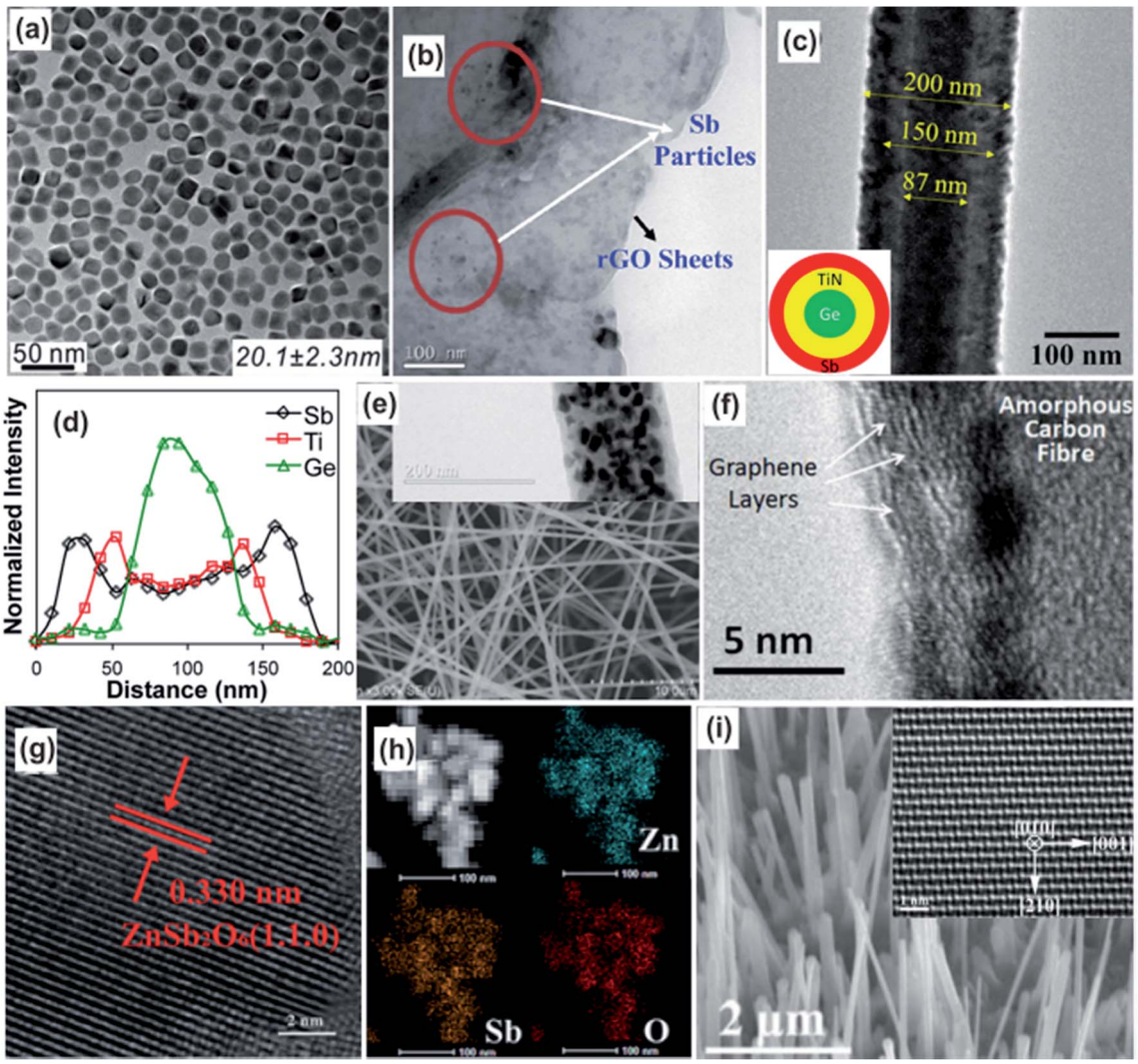

Fig. 7 (a) TEM image of monodisperse Sb nanocrystals. Reproduced with permission.[36] Copyright 2014, American Chemical Society. (b) TEM image of the rGO/Sb composite. Reproduced with permission.[43] Copyright 2014, Royal Society of Chemistry. (c) TEM image and (d) XEDS line scan of 50 nm Sb/NW. Reproduced with permission.[56] Copyright 2015, American Chemical Society. (e) SEM and TEM (inset) images of carbon-encapsulated Sb fibers. Reproduced with permission.[136] Copyright 2013, American Chemical Society. (f) HR-TEM of antimony particles embedded in carbon fibers with a few layers of graphene wrapped in an amorphous carbon fiber. Reproduced with permission.[137] Copyright 2015, Elsevier. (g) HR-TEM image and (h) dark-field TEM image and (i) corresponding elemental mapping of $ZnSb_2O_6$. Reproduced with permission.[138] Copyright 2017, Royal Society of Chemistry. SEM and HR-TEM (inset) images of Zn_4Sb_3 nanowires. Reproduced with permission.[42] Copyright 2016, Wiley.

diameters and composition. A high voltage is applied to a polymer solution to eject a nanoscale fiber form, followed by stabilization and heat treatment to obtain the final product.[131–136] Wang's group used a simple and scalable electrospinning method to fabricate Sb/C fibers with ~30 nm Sb nanoparticles uniformly encapsulated in interconnecting 1D 400 nm carbon fibers (Fig. 7e).[136] Li *et al.* used an electrospinning/spray process to prepare Sb–C–graphene fibrous composites as freestanding anodes for SIBs.[137] Sb nanoparticles were distributed in conductive carbonized polymer fibers and graphene flakes. The HR-TEM image in Fig. 7f shows a few layers of graphene wrapped in amorphous carbon fiber. These graphitic carbon layers were carbonized by the catalytic effect of small Sb nanoparticles during high temperature carbonization.

The co-precipitation method has been intensively used to prepare electrode materials owing to its suitability for large-scale-production.[138–141] Li and co-workers synthesized nano-sized $ZnSb_2O_6$ particles using a facile co-precipitation method and post-annealing.[138] The lattice spacing of ~0.33 nm in HR-TEM was indexed to the (310) plane of a $ZnSb_2O_6$ crystal (Fig. 7g). The elemental mapping with a matching dark-field-TEM image in Fig. 7h reveals that Zn, Sb, and O were uniformly distributed.

CVD has also been used to synthesize Sb-based electrode materials with various architectures.[42,142] Nie *et al.* prepared β-Zn_4Sb_3 nanowires by the CVD method.[42] Zn_4Sb_3 nanowires were grown on Zn metal foils *via* a self-catalysis mechanism using reactive vapor transport in a three-zone hot-walled CVD chamber. The $SbCl_3$ precursor was heated to a temperature of

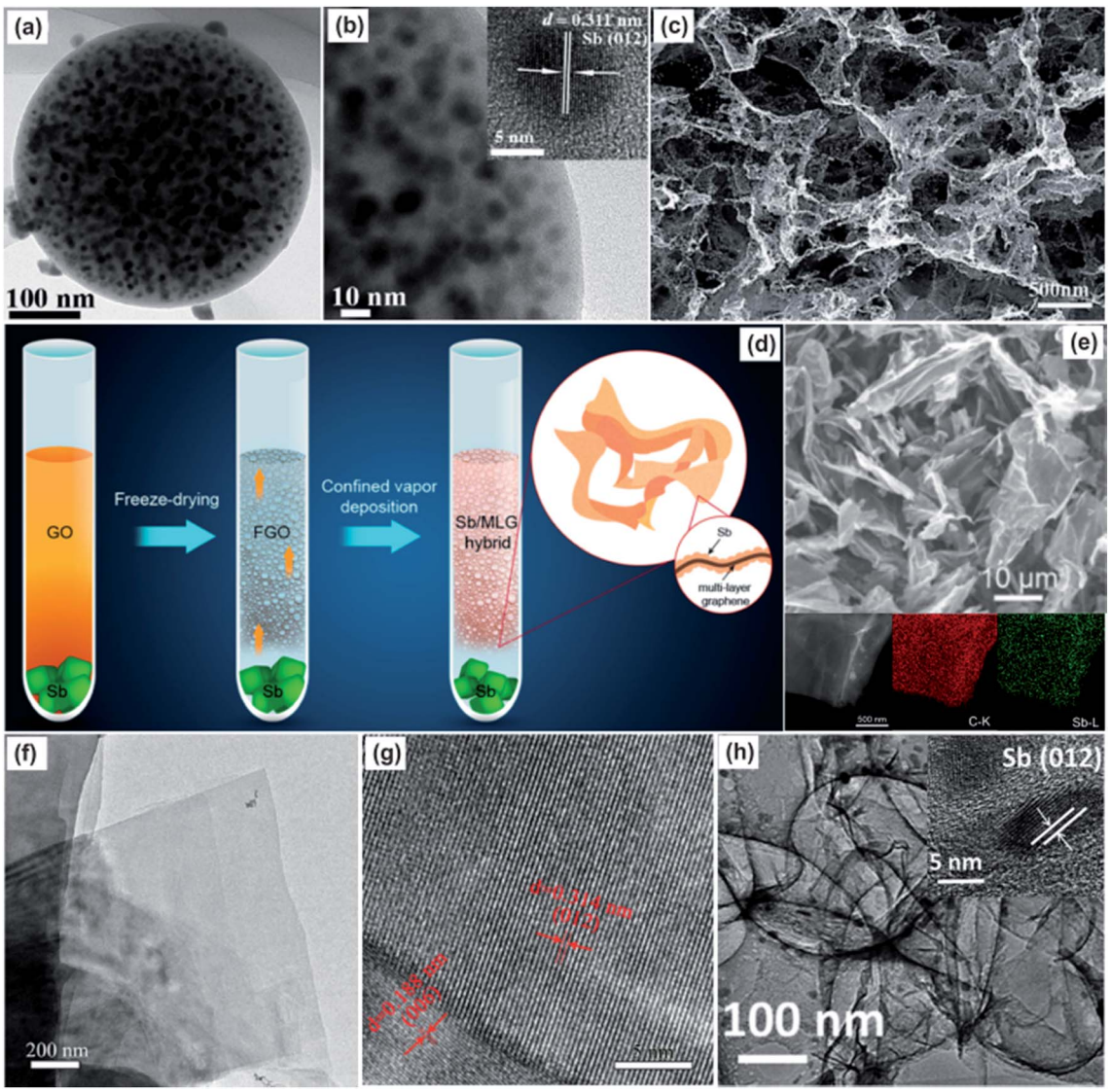

Fig. 8 (a) TEM image and (b) magnified TEM image of the Sb@C composite. Inset: HR-TEM image. Reproduced with permission.[146] Copyright 2015, Springer. (c) SEM of Sb_2O_3/Sb@graphene–CSN. Reproduced with permission.[154] Copyright 2015, Royal Society of Chemistry. (d) Schematic illustration of the preparation process of an Sb/MLG hybrid. (e) SEM and elemental mapping images of the Sb/MLG hybrid. Reproduced with permission.[153] Copyright 2015, American Chemical Society. (f) TEM and (g) HR-TEM images of Sb nanosheets. Reproduced with permission.[144] Copyright 2017, Wiley. (h) TEM and HR-TEM (inset) images of SbNPs@3D-C. Reproduced with permission.[145] Copyright 2016, Elsevier.

Table 2 Summary of the preparation of various Sb-based electrode materials

Types of materials	Synthetic method	Sb source	Ref.
Sb/G nanohybrid	Solvothermal (180 °C, 24 h)	$SbCl_3$	155
Sb_6O_{13}/rGO	Solvothermal (120 °C, 12 h)	Sb_2O_3	33
Sb_2O_3/rGO	Solvothermal (140 °C, 12 h)	Sb_2O_3	27
Sheaf-like Sb_2S_3	Hydrothermal	Antimony acetate	75
1D Sb_2Se_3 nanostructure	Hydrothermal (120 °C, 24 h)	Antimony acetate	156
rGO/SnSb nanocomposites	Hydrothermal (170 °C, 24 h)	Antimony acetate	78
Sb@C microspheres	Solvothermal (140 °C, 10 h)	$SbCl_3$	71
Sb_2S_3@C rods	Solvothermal (180 °C, 12 h)	$SbCl_3$	77
Sb_2Se_3 nanowire membrane	Hydrothermal (180 °C, 12 h)	Antimony acetate	67
Sb_2O_4/rGO	Solvothermal (180 °C, 20 h)	$SbCl_3$	157
Sb_2MoO_6/rGO	Hydrothermal (180 °C, 24 h)	$SbCl_3$	30
Sb_2S_5–graphene foam	Hydrothermal (90 °C, 6 h)	$Na_3SbS_4 \cdot 9H_2O$	28
Sb_4O_5Cl	Hydrothermal (120 °C, 12 h)	$SbCl_3$	76
$(NH_4)InSb_2S_5 \cdot$phen	Solvothermal (160 °C, 6 days)	Sb powder	158
1D Sb/N-doped porous C	Solvothermal (150 °C, 12 h)	$SbCl_3$	10
rGO–Sb_2S_3	Sulfurization & heating	$SbCl_5$	159
Sb/TiC/C	Heat-treatment & HEMM	Sb powder	160
$TiSb_2$	Heat-treatment (900 °C, Ar)	Sb metal	26
$NbSb_2$	Heat-treatment (900 °C, Ar)	Sb metal	26
Sb/Cu_2Sb/C	Heat-treatment (700 °C, H_2/Ar)	Antimony acetate	161
$Li_{1.15}Ni_{0.47}Sb_{0.38}O_2$	Sintering (800–900 °C)	Sb_2O_3	162
Layered $LiNi_{2/3}Sb_{1/3}O_2$	Sintering (800–1000 °C, air)	Sb_2O_3	163
$Li_xNi_{2-4x/3}Sb_{x/3}O_2$	Sintering (800 or 900 °C, O_2)	Sb_2O_3	164
$Na_3Ni_2SbO_6$	Sintering (900 °C)	Sb_2O_3	105
$Fe_{1.18}Sb_{1.82}$	Sintering (720 °C)	Sb powder	165
Nanoporous Sb	Sintering & etching	Sb block	38
Sb–CNC	Ball-milling & heat-treatment	Sb powder	166
SbO_x@C-flakes	Heat-treatment (600 °C, Ar)	$SbCl_3$	167
Sb@N–C	Heat-treatment (600 °C, H_2/Ar)	$SbCl_3$	25
Sb/N–C–CNTs	Ball-milling & pyrolysis	Sb powder	168
Nanostructured C/Sb	Carbon thermal reduction (600 °C, Ar)	$SbCl_3$	169
Sb@TiO_2 1D composite	Thermal reduction (500 °C, H_2/N_2)	Sb powder	170
Sb@TiO_{2-x} nanotubes	Solvothermal & thermal reduction	$SbCl_3$	55
Sb@C coaxial nanotubes	Hydrothermal & carbon thermal reduction	$SbCl_3$	106
Sandwich-like G@Sb@C	Solution method & thermal reduction	$SbCl_3$	39
Sb@S, N-3D-porous C	Template method & thermal reduction	$SbCl_3$	171
Self-wrapped Sb/C nanocomposite	Freezing-dry & thermal reduction	$SbCl_3$	44
Sb@C yolk–shell structure	Solution-coating & thermal reduction	Sb_2O_3	31
Sb/Al_4C_3/C	High-energy mechanical milling (HEMM)	Metallic Sb	172
Sb–MO_x–C (M = Al, Ti, or Mo)	HEMM	Sb powder	83
SnSb/C nanocomposite	HEMM	Sb powder	93
CoSbS	HEMM & heat-treatment	Sb powder	94
Sb/C/graphite	HEMM	Sb powder	173
NiSb–Al_2O_3–C	HEMM	Sb_2O_3	174
$Bi_{0.57}Sb_{0.43}$–C	HEMM	Sb powder	58
Sb–CuP_2-cc	HEMM	Sb powder	175
Graphite/Sb	Solution chemical reduction (KC_8)	$SbCl_5$	176
$SnSbAg_{0.1}$–rGO	Solution chemical reduction ($NaBH_4$)	$SbCl_3$	177
Sb–O–G	Solution chemical reduction ($NaBH_4$)	$SbCl_3$	178
Sb/NPC	Solution chemical reduction ($NaBH_4$)	$C_8H_{10}O_{15}Sb_2K_2$	179
Sb nanocrystals	Solution chemical reduction (Oleylamine)	$SbCl_3$ or $Sb(DMA)_3$	36
Sb–G nanocomposite	Solution chemical reduction ($NaBH_4$)	$SbCl_3$	180
rGO/nano-Sb composite	Solution chemical reduction ($NaBH_4$)	$SbCl_3$	43
Porous Sb/Sb_2O_3 nanocomposite	Solution chemical reduction ($NaBH_4$)	$SbCl_3$	125
Sb nanocrystals	Solution chemical reduction ($NaBH_4$)	$SbCl_3$	181
NiSb-embedded C hollow spheres	Galvanic replacement (80 °C, 24 h)	$SbCl_3$	60
rGO–Sb–Ni sandwiched structure	Galvanic replacement (100 °C, 12 h)	$SbCl_3$	82
Sb/C polyhedral composite	Galvanic replacement (100 °C, 12 h)	$SbCl_3$	80
Cu_2Sb nanoparticles on Cu foil	Galvanic replacement (90 °C, 12 h)	$SbCl_3$	51
Sb hollow nanospheres	Galvanic replacement (100 °C, 10 h)	$SbCl_3$	81
Hollow Sb@C yolk–shell spheres	Galvanic replacement (80 °C, 24 h)	$SbCl_3$	79
Cypress leaf-like Sb	Chemical replacement (Mg)	$SbCl_3$	182
Sb/Sb_2O_3 nanoparticle coatings	Electrodeposition	$K_2(Sb_2(C_4H_2O_6)_2) \cdot 3H_2O$	117

Table 2 (*Contd.*)

Types of materials	Synthetic method	Sb source	Ref.
CoSb nanowire arrays	Electrodeposition	$KSbOC_4H_4O_6 \cdot 1/2H_2O$	61
3D microporous Sb–Sb–Ni alloy	Electrodeposition	Antimony chloride	183
Cu_2Sb film	Electrodeposition	Sb_2O_3	107
Micrometer-long Sb nanowires	Electrodeposition	$SbCl_3$	37
Fern leaf-like Sb	Electrodeposition	$SbCl_3$	118
3D Sb–NiSb–Ni heterostructures	Electrodeposition	$SbCl_3$	119
Porous-Ni-scaffold@SnSb	Electrodeposition	$SbCl_3$	32
$Sn_{50}Ge_{25}Sb_{25}$	Magnetron sputtering	Sb target	59
Cu_2Sb	Magnetron sputtering	Sb target	129
Sb film on TiN/Ge nanowires	Magnetron sputtering	Sb target	56
Sb film	Magnetron sputtering	Sb target	54
SnSb–C fibers	Electrospinning & heat-treatment	$SbCl_3$	131
Sb/C fibers	Electrospinning & heat-treatment	$SbCl_3$	136
$SnSbS_x$/porous CNFs	Electrospinning & sulfidation	Sb_2O_5	184
Sb–C–G fibers	Electrospinning & heat-treatment	$SbCl_3$	137
Sb_2O_3 thin film	Pulsed laser deposition	Sb_2O_3 target	185
Sb_2Se_3	Pulsed laser deposition	Sb powder	186
SbSb–P nanocomposite thin films	Pulsed laser deposition	Sb powder	187
$ZnSb_2O_6$	Co-precipitation & heat-treatment	$K(SbO)C_4H_4O_6 \cdot 1/2H_2O$	138
$SnSbCu_x$/MCMB/C	Co-precipitation & heat-treatment	$SbCl_3$	139
Nano-SnSb/MCMB	Co-precipitation	$SbCl_3$	140
Sb–N/C nanosheets	Sol–gel route & heat-treatment	$SbCl_3$	188
SbO_x/rGO	Wet-milling	Sb powder	45
m-Sb@G	Ball milling	Sb_2O_3	189
Sb/O nano-composites	Spark discharge generation	Sb rod (6 mm diameter)	190
SnSb/G	Microwave heat-treatment	$SbCl_3$	143
Sb nanosheets	Liquid-phase exfoliation	Sb powder	144
Zn_4Sb_3 nanowire	Chemical vapor deposition (CVD)	$SbCl_3$	42
SnSb nanorods in CNTs	CVD (700 °C, C_2H_2/N_2)	Sb_3O_4	142
Sb_2O_3/Sb@graphene–CSN	Microwave plasma enhanced CVD	Antimony acetate	154
SbNPs@3D-C	NaCl template-assisted self-assembly	$SbCl_3$	145
Spherical nano-Sb@C	Aerosol spray pyrolysis	$SbCl_3$	146
Hexagonal and amorphous Sb	Electrochemical cathodic corrosion	Sb rod	147

280 °C to transport the vapor phase onto Zn foils maintained at 400 °C. Fig. 7i demonstrates that the as-prepared β-Zn_4Sb_3 nanowire was a single crystal with a uniform diameter.

3.7 Other typical methods

In addition to these approaches, many other effective strategies have been developed to prepare Sb-based electrode materials with advanced nanostructures.[57,143–154] Chen's group synthesized a spherical nano-Sb@C composite *via* an aerosol spray pyrolysis technique.[146] The TEM images in Fig. 8a and b reveal that the sub-microsphere with an optimized Sb ratio of 68.8 wt% was composed of ultra-small Sb nanoparticles (10 nm) uniformly embedded within a porous carbon matrix. Li *et al.* reported a novel route to encapsulate Sb_2O_3/Sb nanoparticles within a graphene shell nanostructure *via* microwave plasma irradiation of antimony acetate and a subsequent graphene growth process.[154] Fig. 8c shows that the as-prepared material exhibited a 3D network and porous structure.

Hu and colleagues produced an Sb/multilayer graphene (Sb/MLG) hybrid by a confined vapor deposition strategy, in which Sb was homogeneously anchored on multilayer graphene.[153] Fig. 8d illustrates the synthesis process of the Sb/MLG hybrid. Sb and graphene oxide aqueous solution were successively loaded into a single-head sealed glass tube, followed by freeze-drying. Afterward, the glass tube was heated to transform Sb into vapor that was continuously and gradually deposited onto the MLG surface. The SEM image and EDX elemental mapping in Fig. 8e demonstrate that carbon and Sb were homogeneously combined in the hybrid. Gu *et al.* fabricated free-standing metallic Sb nanosheets by liquid-phase exfoliation of gray Sb powder.[144] The TEM image in Fig. 8f shows the ultrathin and foldable features of the as-obtained Sb nanosheets. Fig. 8g reveals that the crystalline lattice fringes correspond to gray Sb. Mai's group prepared a novel composite with Sb nanoparticles anchored in a 3D carbon network through a NaCl template-assisted self-assembly strategy, followed by freeze-drying and one-step *in situ* carbonization.[145] Fig. 8h clearly shows that the uniform Sb nanoparticles (10–20 nm) were dispersedly embedded in the interconnected carbon network.

Various Sb-based electrode materials associated with different synthesis strategies are summarized in Table 2. As can be seen, hydrothermal/solvothermal methods, galvanic replacement, sintering/heat-treatment, HEMM, and electrodeposition are the most widely used strategies for the synthesis of

different types of Sb-based electrode materials owing to their facile synthetic processes and cost-efficient feature. Other frequently used methods such as solution chemical reduction, electrospinning, and magnetron sputtering were often applied to prepare Sb-based active materials with certain structures and morphologies such as fibers and coatings. The diversity of synthetic methods ensures the diversity of the structure and morphology for Sb-based electrode materials, which makes it possible to find suitable Sb-based electrode materials for real batteries.

4. Applications of Sb-based electrode materials in LIBs/SIBs

4.1 Sb-based anode materials

4.1.1 Metallic Sb and its composites. Metallic Sb has demonstrated its potential as a high-performance anode material for LIBs and SIBs owing to its high theoretical capacity of 660 mA h g^{-1}, small electrode polarization, moderate working voltage (0.8–0.9 V), and unique puckered-layer structure.[34,55] Specifically, its small electrode polarization and moderate working voltage could reduce the self-heating effect during cycling and prevent the formation of dendritic lithium crystals on the surface, respectively, making Sb a relatively safe active material. Moreover, the puckered-layer structure with low stacking density could facilitate the diffusion of Li^+ and Na^+ ions and the release of structural strain, thereby resulting in high rate capability and good electrochemical stability.

Darwiche and co-workers studied the electrochemical performance of bulk Sb and its corresponding storage mechanism in LIBs and SIBs and found an unexpected electrochemical mechanism in SIBs.[35] Generally, the lithium storage reactions of bulk Sb were consistent with the sequential formation of crystalline Li_2Sb and crystalline rock salt Li_3Sb, both occurring at one voltage plateau. In SIBs, however, *in situ* XRD observations (Fig. 9a) clearly indicate that Sb initially transformed into an intermediate amorphous phase of Na_xSb and then converted into cubic-hexagonal Na_3Sb mixture phases before stabilizing as hexagonal Na_3Sb upon sodiation. All transformations also occurred at almost the same voltage plateau. During the charge process, Na_3Sb gradually disappeared, leading to the formation of a completely amorphous Na_xSb phase, which then transformed into amorphous Sb metal. Second sodiation thus started from the completely amorphous Sb metal, which then transformed sequentially into amorphous Na_xSb and Na_3Sb. Subsequent cycles underwent a reversible mechanism like that in the first charge and second discharge, with amorphous Na_xSb as the intermediate compound. As shown in Fig. 9b, the better cycling performance of bulk Sb in SIBs than in LIBs is partly attributable to the buffering effect of the amorphous intermediate Na_xSb. Besides, fluoroethylene carbonate (FEC) was shown to improve the cycling performances in both LIBs and SIBs. Although bulk Sb showed good cycling stability at a low current density in SIBs with the addition of FEC, it suffered from serious capacity decay at high current density in SIBs and at both low and high current densities in LIBs. When FEC was absent from the electrolyte, the capacity seriously collapsed after about only 15 cycles in both LIBs and SIBs independent of the current rate. The inferior cycling performance of bulk Sb mainly results from its large volume expansion during sodiation and lithiation.

As reported in previous studies, Sb has a large theoretical volume expansion of 147% and 293% in LIBs and SIBs,

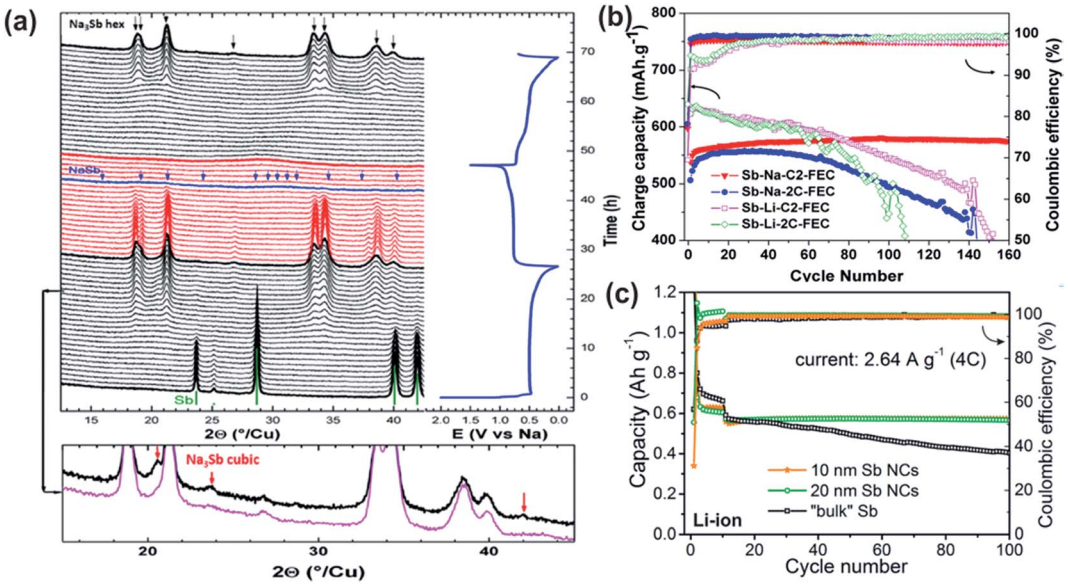

Fig. 9 (a) Operando evolution of the XRD pattern (top left). The black and red patterns were recorded during the discharges and charge, respectively (the corresponding voltage profile is at the top right, and a magnified image illustrating the diffraction peaks from cubic Na_3Sb is at the bottom). (b) Cycling performance of Sb electrodes at C/2 and 2C for LIBs and SIBs. Reproduced with permission.[35] Copyright 2012, American Chemical Society. (c) Cycling performance of Sb NC and bulk electrodes in LIBs at 4C rate. Reproduced with permission.[36] Copyright 2014, American Chemical Society.

respectively, which pulverizes the active particles and causes capacity degradation.[31,55,106] Designing porous and hollow structures, tuning the morphology and structure at the nanoscale, and hybridizing with buffer materials such as carbonaceous materials are all efficient strategies for addressing this issue.

He *et al.* reported monodisperse Sb nanocrystals as an anode material for LIBs and SIBs and compared them with bulk Sb.[36] As shown in Fig. 9c, the nanosized Sb electrodes demonstrated excellent cycling stability at 4C-rate (1C = 660 mA g^{-1}), whereas the capacity of bulk Sb faded quickly in both LIBs and SIBs. Note that the specific capacities were always higher for 20 nm Sb nanocrystals than for 10 nm nanocrystals and bulk Sb in both LIBs and SIBs. The lower capacities of the 10 nm Sb crystals most likely resulted from the high proportion of surface oxides on the small Sb nanocrystals, which caused the irreversible formation of Li_2O and Na_2O during the initial discharge. The even lower capacity of 10 nm nanocrystals in SIBs (compared with that in LIBs) was attributed to the poorer conductivity of Na_2O compared with Li_2O. In the case of the rate capacities of LIBs, the 10 and 20 nm Sb nanocrystals exhibited capacities close to their theoretical capacities at 0.5C and a capacity retention of 78% and 85% at 20C, respectively, whereas the bulk Sb anodes retained only 40% of their initial capacity. In SIBs, the 10 and 20 nm nanocrystals exhibited a rate-capability similar to that in LIBs with an increase in the current rate, retaining 80–85% of their initial capacities at 20C, whereas a retention of only 50% was obtained for bulk Sb.

Janek's group synthesized high-aspect-ratio Sb nanowires by template-free electrodeposition at room temperature.[37] The Sb nanowires with diameters down to 30 nm and lengths up to several tens of micrometers were uniform and grew densely on different substrates. These high-quality Sb nanowires demonstrated good electrochemical performance when they were used as anode materials for LIBs. As shown in Fig. 10a, the specific capacities of the Sb nanowires quickly stabilized at around 580 and 540 mA h g^{-1} at current densities of ~210 and 420 mA g^{-1}, respectively. Sb hollow nanospheres (HNSs) were successfully synthesized by Hou and co-workers and applied as anode materials for LIBs and SIBs.[81] The cycle performance of the Sb nanospheres in SIBs is shown in Fig. 10b. They demonstrated superior cycling stability, delivering a high reversible capacity of ~622 mA h g^{-1} after 50 cycles, which was close to the theoretical capacity of Sb (600 mA h g^{-1}). The initial coulombic efficiency was around 77%, and it then stabilized at around 98% for the subsequent cycles. The good electrochemical properties are largely attributable to the hollow interiors, which acted as buffer spaces for the volume change of the Sb thin shell. The benefits of this unique structure could also be extended to LIBs, resulting in a reversible capacity of 627 mA h g^{-1} at 100 mA g^{-1} after 50 cycles. Liu *et al.* reported a nanoporous Sb anode for SIBs:[38] depending on the Sb ratio in the Al–Sb alloy composition, coral-like NP-Sb (NP-Sb70, 70 stands for the weight ratio of Sb in the Al–Sb alloy), honeycomb-like NP-Sb (NP-Sb80), and Sb particles of different sizes (Sb10, Sb30 and Sb45) were prepared. As displayed in Fig. 10c, the NP-Sb70 showed a capacity of 573.8 mA h g^{-1} after 200 cycles at a current density of 100 mA g^{-1}, which corresponded to 86.9% of its theoretical capacity. After the initial capacity loss, the columbic efficiency of the NP-Sb70 approached 100%, indicating excellent reversibility. The honeycomb-like NP-Sb80 electrodes also showed a high capacity of 546.7 mA h g^{-1} after 100 cycles. Their excellent electrochemical performance resulted from their unique design, which ensured strong structural integrity, high Na^+ ion accessibility, and fast electron transport.

Ji's group studied the influences of the crystalline and amorphous phases of Sb nanomaterials on the electrochemical performance of LIBs and SIBs.[147] The galvanostatic charge/discharge curves of hexagonal Sb and amorphous Sb in LIBs and SIBs were tested at 100 mA g^{-1}. In LIBs, similar Li^+ ion storage behavior was observed for both hexagonal and amorphous Sb (Fig. 10d and e). The plateau around 1.3 V during the initial discharge, which then disappeared in the subsequent cycles, could be attributable to the irreversible reduction of surface Sb_2O_3, which formed Sb and Li_2O. The reduction process below 0.9 V involved alloying reactions between Sb and Li, as well as the formation of a solid electrolyte interface (SEI) layer. As can be seen in the figure, the shape of the voltage profiles did not change much for all cycles, indicating the good stability of both Sb electrodes. As for SIBs, hexagonal Sb and amorphous Sb also revealed similar voltage profiles but more complex electrochemical behavior than that seen in LIBs. In rate tests, the hexagonal and amorphous Sb showed comparable rate capability in LIBs. However, the hexagonal Sb demonstrated much better rate performance than the amorphous Sb in SIBs. The limited rate performance of amorphous Sb in SIBs could be ascribed to the thick SEI layer and presence of Na_xO and Sb_2O_3, whose low conductivity would slow the charge transfer rate. Ji's group also compared the cycling performance of an amorphous Sb anode in LIBs using a poly (vinylidene difluoride) (PVDF) or water-soluble carboxymethyl cellulose (CMC) binder with or without adding FEC to the electrolyte. Fig. 10f clearly shows that a CMC binder and FEC additive could synergistically enhance the electrochemical performance.

Combination carbonaceous materials, such as graphene with nanosized Sb, can further improve electrochemical performance. During the cycling process, carbon not only acts as a buffer material to mitigate pulverization, but also works as a conductive matrix to enhance the rate capacity. Wang *et al.* designed and prepared a carbon-coated graphene/Sb composite with a sandwich-like structure (G@Sb@C) and applied it as a SIB anode material.[39] As shown in the schematic illustration of the sodiation/desodiation processes (Fig. 11a), the carbon layer and graphene sheets associated with the unique sandwich-like structure well accommodated the large volume changes of Sb synergistically during the periodic sodiation/desodiation processes, thereby significantly enhancing the stability of the G@Sb@C electrode. Moreover, the graphene framework and carbon layer also enhanced electrical conductivity and dispersed the Sb particles uniformly. These merits allowed the G@Sb@C electrode to show much better electrochemical performance than G@Sb and pure Sb electrodes (Fig. 11a). A high reversible capacity of 569.5 mA h g^{-1} could be retained for

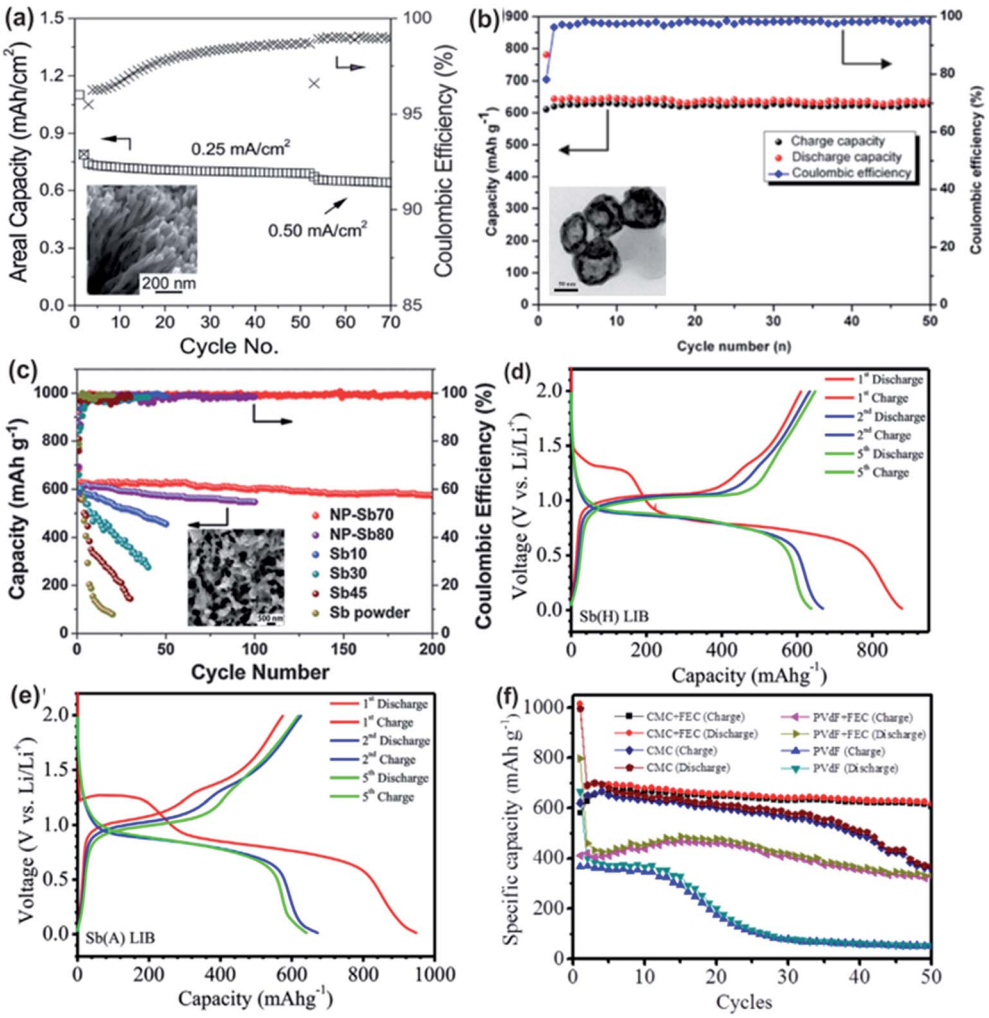

Fig. 10 (a) Capacity retention and coulombic efficiency of Sb NW electrodes in Li cells. Reproduced with permission.[37] Copyright 2016, Royal Society of Chemistry. (b) Cycle performance of the Sb HNS anode in SIBs. Reproduced with permission.[81] Copyright 2014, American Chemical Society. (c) Cycling performance of the NP-Sb70, NP-Sb80, Sb10, Sb30, Sb45 and commercial Sb powder electrodes at 100 mA g^{-1} in 0.1–1.5 V *versus* Na^+/Na. Reproduced with permission.[38] Copyright 2016, Royal Society of Chemistry. Galvanostatic charge/discharge curves of (d) amorphous Sb and (e) hexagonal Sb for LIBs at 100 mA g^{-1} in 0.01–2.0 V. (f) Cycling performance of the amorphous Sb anode in LIBs at 100 mA g^{-1} using an ordinary PVDF or water-soluble CMC binder with or without the FEC electrolyte additive. Reproduced with permission.[147] Copyright 2015, Elsevier.

G@Sb@C after 200 cycles without any obvious capacity loss. The pure Sb electrode displayed the fastest capacity decay, with only 133 mA h g^{-1} remaining after 200 cycles. Liu and colleagues prepared Sb@C coaxial nanotubes as an anode material for SIBs.[106] With different annealing times, the hollow space and amount of Sb inside the tube could be easily tuned by the partial evaporation of Sb. As a result, Sb@C-5 (with 5 minutes of annealing) exhibited the highest specific capacity, with an excellent rate capacity and long, stable cycling performance due to a relatively large amount of Sb and suitable hollow space. Fig. 11b remarkably shows that Sb@C-5 delivered a high capacity of 350 mA h g^{-1} even at a high current density of 10 A g^{-1}, a value comparable to that of graphite in LIBs. When the current rate returned to 0.1 A g^{-1}, the Sb@C-5 electrode was able to quickly retain a reversible capacity of 441 mA h g^{-1}, which then remained stable for extended cycles.

Yang's group fabricated free-standing metallic Sb nanosheets and blended them with graphene to prepare several hybrid films (SbNS-G) with tunable densities.[144] The large volume changes of metallic Sb could be efficiently alleviated with the aid of the flexible graphene, and the volumetric capacities of the electrode films could be greatly improved by harnessing the high density of Sb nanosheets. Fig. 11c and d show the cycling and rate performance of SbNS-G films with different mass loadings. The SbNS-G film with a mass loading of 1.6 mg cm^{-2} exhibited a high reversible volumetric capacity of 1226 mA h cm^{-3} in the initial cycle at 0.1 mA cm^{-2} and gradually stabilized at 650 mA h cm^{-3} after 50 cycles. Increasing the mass loading to 2.4 and 3.2 mg cm^{-2} decreased the volumetric capacities of these hybrid films due to the unfavorable diffusion of Na^+ ions in such compacted films. Song *et al.* fabricated yolk–shell structured Sb@C anodes for SIBs and used *in situ* TEM to

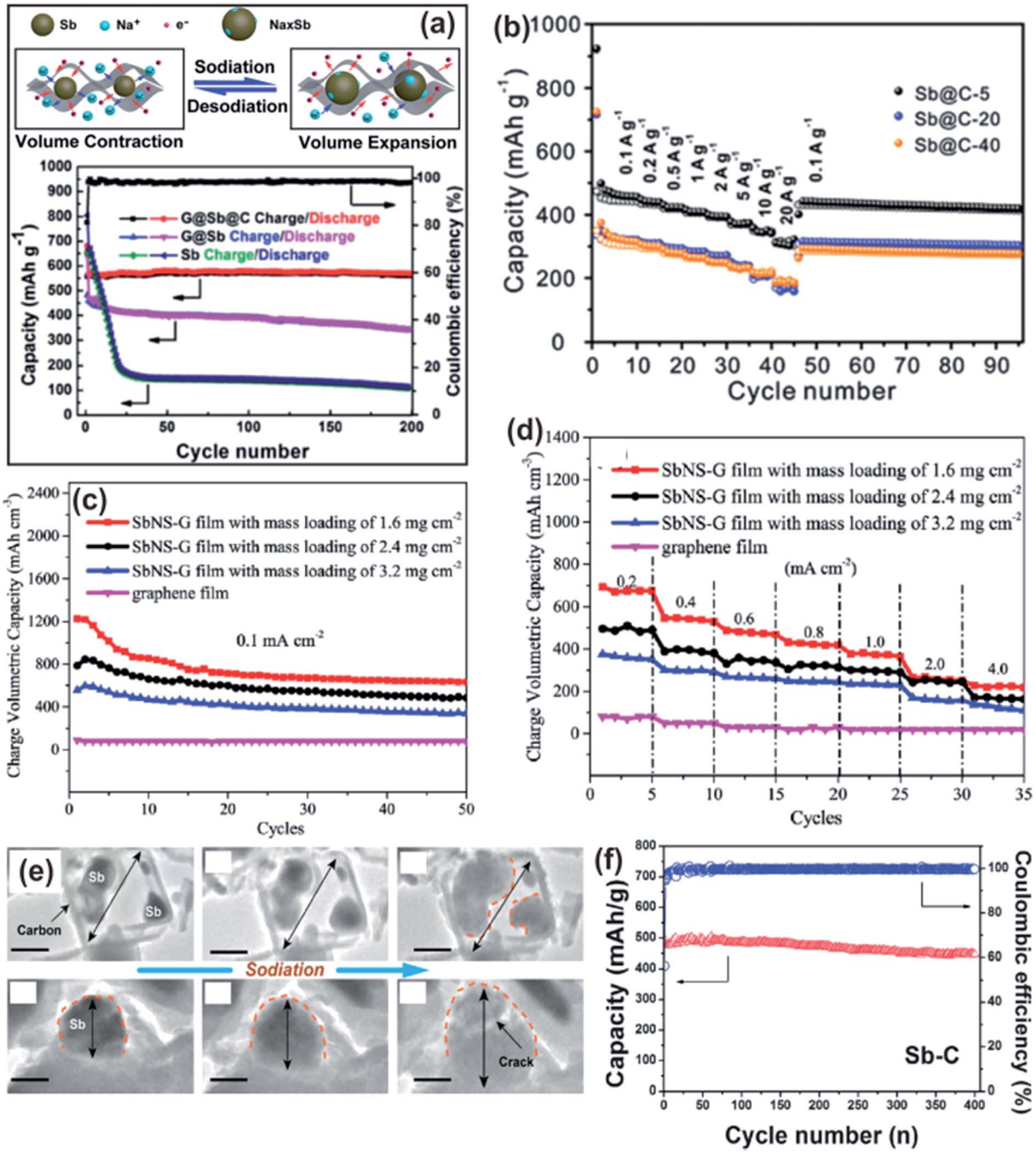

Fig. 11 (a) Schematic illustration of the sodiation/desodiation process of a sandwich-like G@Sb@C composite and cycling performances of G@Sb@C, G@Sb, and Sb electrodes at 0.1 A g^{-1}. Reproduced with permission.[39] Copyright 2017, Royal Society of Chemistry. (b) Rate performance of coaxial Sb@C nanotubes with different annealing times. Reproduced with permission.[106] Copyright 2016, Royal Society of Chemistry. (c) Cycling performances of SbNS-G and graphene films at 0.1 mA cm^{-2}. (d) Rate performances of SbNS-G and graphene films. Reproduced with permission.[144] Copyright 2017, Wiley. (e) *In situ* TEM snapshots showing the structural evolution of the Sb@C yolk–shell structure and bare Sb nanoparticle upon sodiation. Reproduced with permission.[31] Copyright 2017, Elsevier. (f) Cycling performance of the Sb–C nanofiber electrode at a cycling rate of C/3 (200 mA g^{-1}). Reproduced with permission.[191] Copyright 2014, Royal Society of Chemistry.

show the structural evolution of the Sb@C yolk–shell structure and bare Sb nanoparticles upon sodiation.[31] Fig. 11e clearly reveals that Sb nanoparticles encapsulated in the carbon shell underwent large volume expansion, but the whole yolk–shell structure showed a smaller volume increase. In contrast, Sb without a host structure suffered from large volume expansion, with cracks forming upon sodiation. Therefore, the yolk–shell structure effectively accommodated the large volume changes of Sb and mitigated the pulverization of Sb particles in real batteries. As a consequence of these features, the yolk–shell Sb@C active material showed long cycling stability, with a capacity retention up to 92% over 200 cycles. Cao's group

synthesized Sb–C nanofibers with Sb nanoparticles embedded homogeneously in carbon nanofibers by a facile electrospinning method.[191] The nanofiber electrode exhibited excellent cycling stability with 90% capacity retention after 400 cycles (Fig. 11f).

Hybridization with materials other than carbonaceous materials, such as titanium oxide or alumina, can also enhance the electrochemical performance of Sb. Yoon and Manthiram prepared Sb–MO_x–C (M = Al, Ti, and Mo) nanocomposites for use as SIB anode materials.[83] The nanostructured Sb was confirmed to disperse uniformly in amorphous Al_2O_3, TiO_2, and MoO_3 matrices, along with conductive carbon. Fig. 12a shows that these composite electrodes exhibited much higher electrochemical cycling performance than pure Sb. In addition, all three nanocomposites displayed excellent rate capability (Fig. 12b). Sb–AlO_x–C in particular delivered a high capacity of 489 and 487 mA h g^{-1} at 3C and 5C, respectively. The excellent electrochemical performance was attributed to the buffering effect provided by the amorphous metal oxide and conductive carbon matrix during the cycling process. Double-walled Sb@TiO_{2-x} nanotubes were synthesized by Yang's group.[55] This nanotube anode material showed excellent electrochemical performance in both LIBs and SIBs. As shown in Fig. 12c, Sb@TiO_{2-x} exhibited outstanding capacity retention at various current densities from 0.132 to 13.2 A g^{-1}, and it preserved 75.8% and 70.8% of the initial capacity even at high rates of 6.6 and 13.2 A g^{-1}, corresponding to a capacity of 526 and 488 mA h g^{-1}, respectively. Excellent rate performance was also seen in full cells that used Sb@TiO_{2-x} and $LiCoO_2$ as anode and cathode materials, respectively. Fig. 12d displays typical voltage profiles at various current rates. Even when the rate increased greatly, the reversible capacities and voltage plateaus decreased only slightly, indicating the good reaction kinetics between Sb@TiO_{2-x} and Li^+ ions.

4.1.2 Sb-based alloys and composites. As explained above, Sb-based alloys can be divided into active–active and active–inactive types. Both types have a self-buffering effect to alleviate the volume changes of Sb or both Sb and the other active element during charging/discharging processes, which makes Sb-based intermetallic compounds attractive as electrode materials.[9,34] Despite this desirable feature, the electrochemical properties of Sb-based alloys are often limited by the cracking and pulverization of active particles during long-term cycling processes. Recently, many Sb-based alloys have been reported to exhibit superior electrochemical performance due to novel structural designs and composition optimization.[50,51,62,91,93,116,139,187,192,193]

The SnSb alloy is an attractive active material for LIBs and SIBs owing to the high theoretical capacities of both elements. For lithium storage, both components of this alloy contribute to a high theoretical capacity of 824 mA h g^{-1} through the formation of the fully lithiated products of Li_3Sb and $Li_{4.4}Sn$.[50] Similarly, the theoretical capacity for SIBs is 752 mA h g^{-1} based on the formation of Na_3Sb and $Na_{3.75}Sn$.[50,64] Walter *et al.* reported a simple and inexpensive colloidal synthesis of SnSb nanocrystals with a size of around 20 nm. They applied the SnSb nanocrystals as an anode material for LIBs and SIBs.[50] As shown

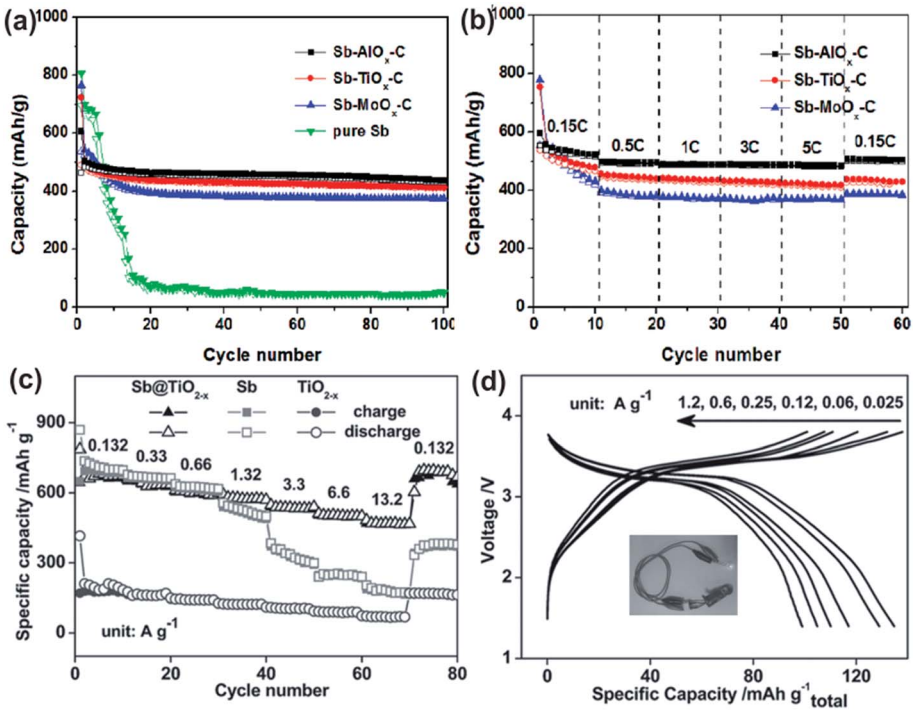

Fig. 12 Comparison of the cycling performances of Sb–MO_x–C (M = Al, Ti, and Mo) nanocomposites (a) at the C/5 rate and (b) at various C rates at 25 °C. Reproduced with permission.[83] Copyright 2009, American Chemical Society. (c) Rate capability of the Sb@TiO_{2-x}, Sb, and TiO_2 electrodes in LIBs. (d) Charge/discharge curves of Sb@TiO_{2-x}||$LiCoO_2$ full batteries at different rates. Reproduced with permission.[55] Copyright 2016, Wiley.

in Fig. 13a, they demonstrated high reversible capacities and excellent rate capabilities in LIBs, with retained capacities of around 890, 680, and 510 mA h g^{-1} after 100 cycles at current rates of 200, 1000, and 5000 mA g^{-1}, respectively. The observation of capacity higher than the theoretical capacity possibly resulted from reversible interfacial lithium storage mechanisms and the reversible lithium storage of a polymeric gel-like layer formed by the electrolyte. Similarly, the SnSb nanocrystals exhibited outstanding sodium storage properties, with only an ~5% capacity loss after 100 cycles at 5000 mA g^{-1} (Fig. 13c). Moreover, the relatively low delithiation and desodiation potentials made the SnSb nanocrystals a highly attractive material for full-cell applications. The SnSb nanocrystals exhibited stable cycling performance in full cells with specific anodic capacities of 600 and 400 mA h g^{-1} for LIBs and SIBs, respectively (Fig. 13b and d). Wang and Lee reported CNT-encapsulated SnSb nanorods with a diameter of 90 nm and a wall thickness of 7–10 nm (Fig. 13e).[142] The measured Sn/Sb atomic ratio of around 8 : 1 corresponded to the ratio in the antimony tin oxide (ATO) precursor. 7.6 wt% of CNTs and 92.4 wt% of Sn–Sb associated with the 1D nanorod structure contributed to high specific capacities and good cycling performance for these CNT-encapsulated Sn–Sb nanorods in LIBs (Fig. 13f). Specifically, they sustained a high specific capacity of above 900 mA h g^{-1} for at least 30 cycles at 0.2C within a voltage range of 0.05–2.0 V. When tested in a narrower voltage range of 0.1–1.2 V, the CNT-encapsulated Sn–Sb nanorod anode exhibited even more stable cycling performance, with a 94.9% retention of the initial capacity (708 mA h g^{-1}) after 80 cycles. Ji and co-workers prepared nanocomposites made of

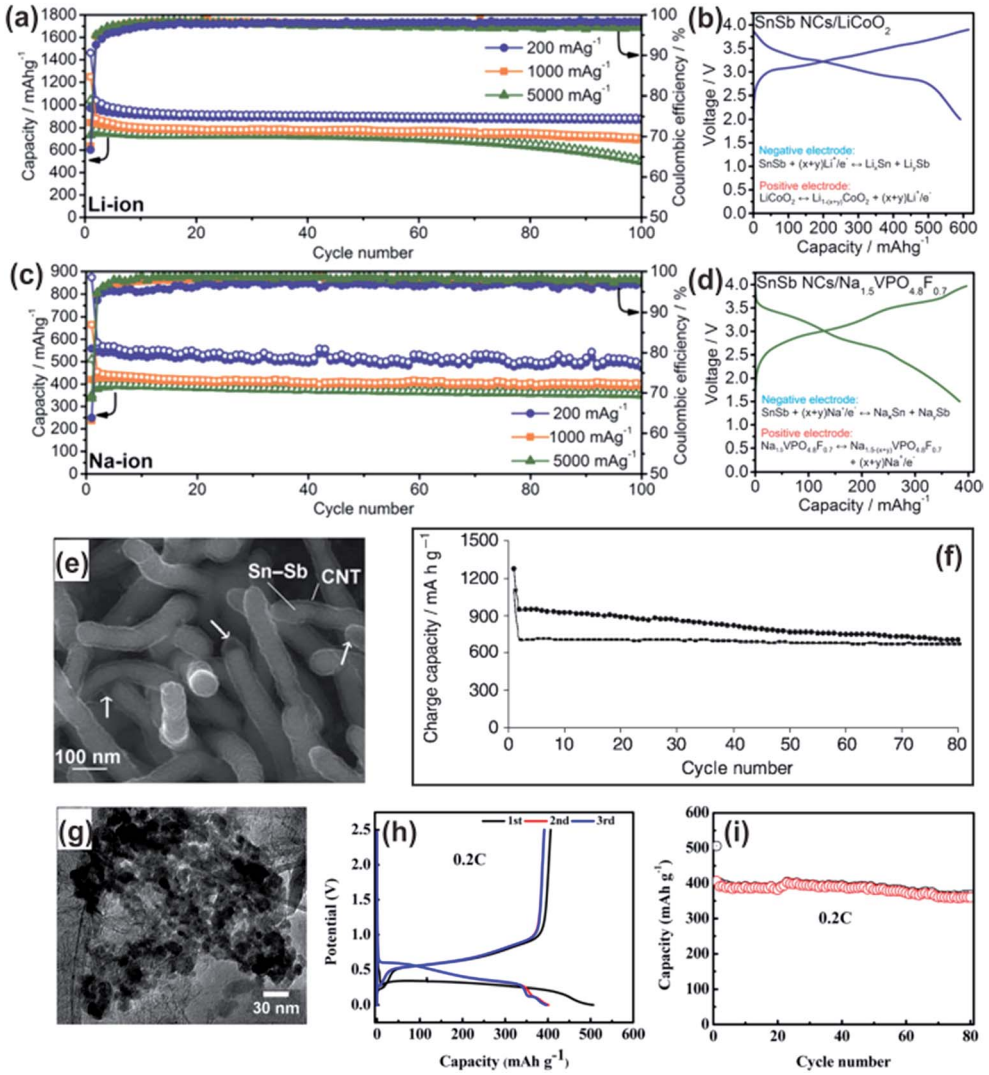

Fig. 13 Electrochemical performance of SnSb NCs. Capacity retention in (a) Li-ion and (c) Na-ion half-cells at currents of 200, 1000 and 5000 mA g^{-1}. Galvanostatic charge/discharge curves of (b) Li-ion and (d) Na-ion full-cells. Reproduced with permission.[50] Copyright 2016, Royal Society of Chemistry. (e) SEM image of CNT encapsulated Sn–Sb nanorods. (f) Cyclability of CNT-encapsulated Sn–Sb nanorods in 5 mV–2 V and 0.1 V–1.2 V (*vs.* Li^+/Li) at 0.2C. Reproduced with permission.[142] Copyright 2006, Wiley. (g) TEM image of rGO–SnSb nanocomposites. (h) Voltage profiles and (i) cycling performance of rGO–SnSb electrodes in 0.001–2.5 V at 0.2C. Reproduced with permission.[78] Copyright 2015, American Chemical Society.

reduced graphene oxide loaded with SnSb (rGO–SnSb).[78] As can be seen in Fig. 13g, the as-synthesized SnSb nanoparticles with a size of 20–30 nm homogeneously coated the rGO surfaces. When applied as an anode material for SIBs, the rGO–SnSb nanocomposite exhibited good electrochemical performance. Fig. 13h shows that the electrode delivered a high charge capacity of ~407 mA h g^{-1}, with a high initial coulombic efficiency of 80.34% in the first cycle. After 80 cycles, a reversible capacity of 361 mA h g^{-1} remained, with a capacity retention of 88.7% (Fig. 13i). The improved sodium storage properties were attributed to the synergetic effects of the rGO-based flexible framework and the nanoscale dimensions of the SnSb alloy particles. During sodiation/desodiation, the rGO framework played multiple roles, providing high electronic conductivity, suppressing the agglomeration of SnSb nanoparticles, and accommodating the volume changes of the SnSb particles. The nanosized SnSb compounds exhibited improved structural stability and conductivity compared to corresponding Sn or Sb particles.

In addition to SnSb intermetallic compounds, other Sb-based alloys have also been reported to show excellent electrochemical performance in LIBs and SIBs. The β phase of Zn_4Sb_3 shows a good electrical conductivity of 5×10^4 S m^{-1} at room temperature, which is 25 times higher than that of amorphous carbon.[42] Orthorhombic ZnSb has a puckered layer structure that greatly facilitates Li^+ or Na^+ ion diffusion.[9,194] These intrinsic features make Zn–Sb alloys potential electrode materials for LIBs and SIBs. Nie *et al.* demonstrated that Na^+ ions could be reversibly stored in β-Zn_4Sb_3 nanowires.[42] They constructed a nanosized sodium-ion battery with individual β-Zn_4Sb_3 nanowires as the working electrode and used *in situ* TEM to observe the sodiation/desodiation processes. During the initial sodiation process, Zn_4Sb_3 first converted into an amorphous phase and further transformed into hexagonal Na_3Sb and cubic $NaZn_{13}$, with a 160% volume expansion (Fig. 14a). Upon desodiation, the electro-diffraction patterns (EDP) revealed that the nanocrystalline Na_3Sb and $NaZn_{13}$ transformed into tetragonal NaZnSb and hexagonal Zn (Fig. 14b). The formation of NaZnSb and Zn instead of β-Zn_4Sb_3 explained

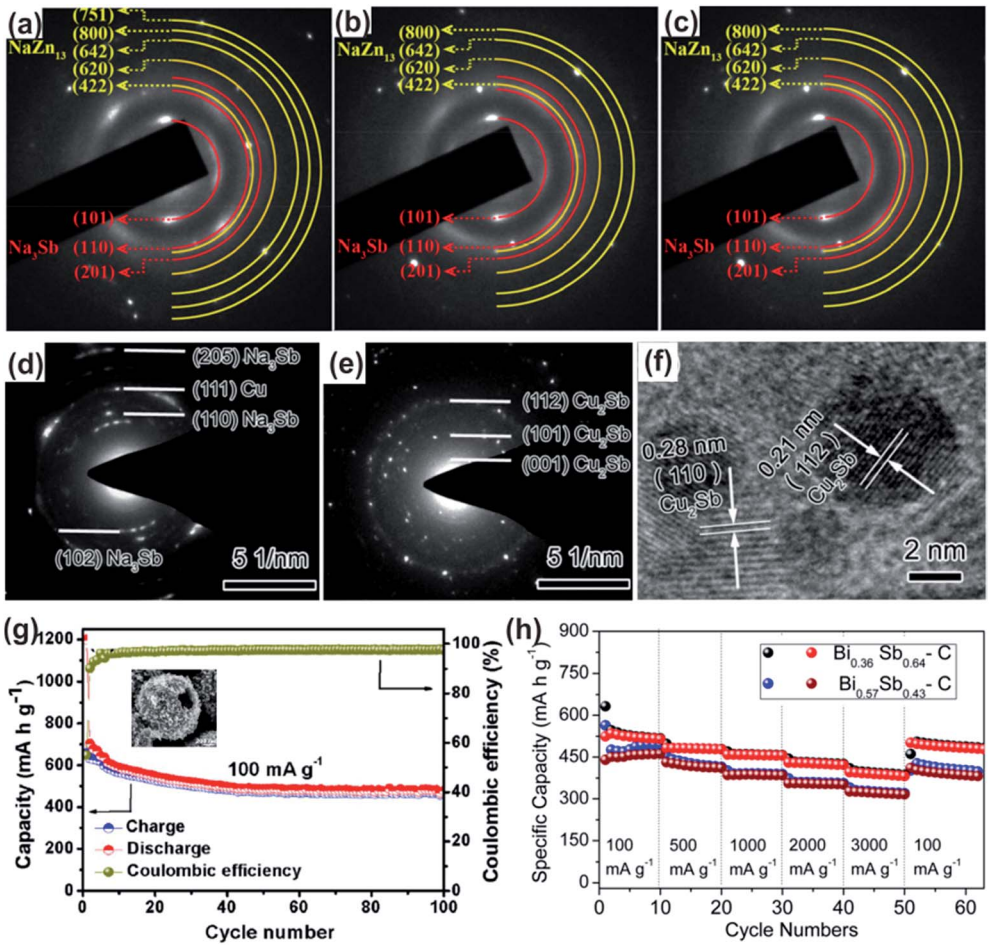

Fig. 14 Electron diffraction patterns of Zn_4Sb_3 nanowires after the (a) 1st sodiation, (b) 1st desodiation and (c) 2nd sodiation. Reproduced with permission.[42] Copyright 2016, Wiley. SAED patterns of the Cu_2Sb/Cu electrode (d) discharged to 0.05 V and (e) charged to 2.0 V. (f) HR-TEM image of the Cu_2Sb/Cu electrode charged to 2.0 V. Reproduced with permission.[51] Copyright 2016, American Chemical Society. (g) Cycling performance of NiSb–CHS anodes at 100 mA g^{-1}. Reproduced with permission.[60] Copyright 2017, American Chemical Society. (h) Rate capacity of $Bi_{0.57}Sb_{0.43}$–C and $Bi_{0.36}Sb_{0.64}$–C electrodes. Reproduced with permission.[58] Copyright 2015, American Chemical Society.

why the volume expansion was not completely recovered after the first desodiation. The EDP of the nanowire indicated the reformation of the crystalline Na_3Sb and $NaZn_{13}$ after the second sodiation (Fig. 14c), which suggested a reaction mechanism between β-Zn_4Sb_3 and Na^+ ions:

1st sodiation:

$$Zn_4Sb_3 + Na^+ + e^- \rightarrow Na_3Sb + NaZn_{13} \quad (4.1)$$

1st desodiation:

$$Na_3Sb + NaZn_{13} \rightarrow NaZnSb + Zn + Na^+ + e^- \quad (4.2)$$

After the first cycle:

$$NaZnSb + Zn + Na^+ + e^- \leftrightarrow Na_3Sb + NaZn_{13} \quad (4.3)$$

The β-Zn_4Sb_3 nanowire electrode was tested between 0.01 and 2.0 V at 0.5C. The initial discharge and charge capacities were 675 mA h g^{-1} and 395 mA h g^{-1}, respectively. The formation of NaZnSb and Zn instead of Zn_4Sb_3, as well as the formation of an SEI layer, could explain this irreversible capacity loss. The β-Zn_4Sb_3 nanowires demonstrated a high rate capacity of 187 mA h g^{-1} at 5C and cycling stability for 200 cycles, with a coulombic efficiency up to 99%.

Chen's group reported a scalable and binder-free Cu_2Sb/Cu electrode with Cu_2Sb nanoparticles integrated on Cu foil as an anode for SIBs. They also studied the reaction mechanism using *ex situ* XRD and TEM characterization.[51] The SAED patterns and TEM image in Fig. 14d–f, respectively, reveal the formation of Na_3Sb and Cu after the initial sodiation and the reformation of Cu_2Sb after desodiation, indicating a reversible process during charging and discharging processes. Based on this reversible reaction mechanism and the structural uniqueness of the nanoporous Cu_2Sb/Cu, the anode showed excellent rate capability and cycling performance, with a specific capacity of 256 mA h g^{-1} at 8 A g^{-1} and a capacity retention of 98.5% after 200 cycles. Yu and co-workers synthesized MOF-derived NiSb nanoparticles embedded in hollow carbon spheres (NiSb@CHS) and applied them as the anode material for LIBs.[60] The hollow structure associated with the porous carbon network effectively solved the problem of volume changes in the NiSb alloy and also provided a reduced pathway for fast Li^+ ion diffusion and electron transport. These features contributed to excellent cycling performance, high specific capacity, and rate capability. Fig. 14g shows that the discharge capacity remained 497.3 mA h g^{-1} after 100 cycles, with a coulombic efficiency of ~98%. Zhao and Manthiram synthesized homogeneous Bi–Sb alloys by a facile HEMM process with carbon and evaluated them as anode materials for LIBs and SIBs, showing improved electrochemical properties.[58] For instance, the $Bi_{0.57}Sb_{0.43}$–C sample demonstrated an initial delithiation capacity of 410 mA h g^{-1} and a capacity retention of 72% after 300 cycles, corresponding to 0.09% capacity decay per cycle. It also had high rate capabilities in LIBs, delivering capacities of 355 and 326 mA h g^{-1} at current rates of 5C and 7.8C, respectively (Fig. 14h).

Farbod and colleagues reported ternary Sn–Ge–Sb thin film alloys with various compositions for application as SIB anodes.[59] $Sn_{50}Ge_{25}Sb_{25}$ revealed the best sodium storage properties among them. Specifically, it delivered an initial reversible specific capacity of 833 mA h g^{-1} with a capacity retention of 79.5% after 50 cycles and an excellent rate capacity of 381 mA h g^{-1} at a high current density of 8500 mA g^{-1}. Yuan's group synthesized $SnSbAg_{0.1}$–rGO composite anode materials for LIBs.[177] The $SnSbAg_{0.1}$–10% rGO composite exhibited the best electrochemical performance among those tested, demonstrating a capacity of 538 mA h g^{-1} after 200 cycles.

4.1.3 Antimony oxides. Antimony oxides have the highest theoretical capacities among all kinds of Sb-based electrode materials because both the conversion and alloying reactions that occur during charging and discharging processes can contribute high capacities.[72,154,157,185,195,196] For instance, Sb_2O_3 and Sb_2O_4 have a theoretical capacity of 1103 mA h g^{-1} and 1227 mA h g^{-1}, respectively.[66,197] However, these anodes suffer from severe volume changes during cycling, leading to rapid structural failure. Wang's group synthesized 1D tube-like Sb_2O_4 with a submicron structure to address the volume expansion issue.[197] With the hollow structure to buffer the volume changes, these Sb_2O_4 tubes exhibited improved lithium and sodium storage properties. When evaluated as a LIB anode, the Sb_2O_4 submicron-structures delivered a high discharge capacity of 700 mA h g^{-1} after 50 cycles at a current rate of 100 mA g^{-1}, with coulombic efficiencies close to 100% (Fig. 15a). In addition, the tube-like Sb_2O_4 demonstrated high rate capabilities (Fig. 15b). The average discharge capacity could reach as high as 371 mA h g^{-1}, even at a high current rate of 2000 mA g^{-1}, and it could also be retained when the current density returned to a low value.

Zhou *et al.* reported a Sb_2O_3 and reduced graphene oxide composite (Sb_2O_3/rGO) with Sb_2O_3 nanoparticles uniformly anchored onto rGO sheets.[27] To verify the electrical conductivity of the obtained samples, they conducted electrochemical impedance spectroscopy (EIS) measurements for electrodes made with bulk Sb_2O_3, Sb_2O_3/rGO (with L-ascorbic acid (L-AA) in the synthesis process), and Sb_2O_3–rGO (without L-AA in the synthesis process) (Fig. 15c). It is worth noting that the Sb_2O_3/rGO composite exhibited the smallest charge-transfer resistance, indicating that the electrical contact between Sb_2O_3 and rGO was further enhanced by a stronger electrical coupling effect and a great increase in the reduction degree of GO with the addition of L-AA. Therefore, the Sb_2O_3/rGO composite revealed a high rate and high reversibility in conversion–alloying lithium storage. Fig. 15d shows the cycling performance of the as-prepared electrodes at 100 mA g^{-1}. The Sb_2O_3/rGO composite delivered a high reversible capacity of 1335 mA g^{-1}, with an initial coulombic efficiency of 60%. After 120 cycles, a reversible capacity up to 808 mA h g^{-1} could still be achieved, which was much higher than that in the other samples. Remarkably, the obtained Sb_2O_3/rGO electrode exhibited a reversible specific capacity of 525 mA h g^{-1} after 700 cycles.

Li and colleagues reported a novel strategy for encapsulating Sb_2O_3/Sb nanoparticles within a graphene shell nanostructure (Sb_2O_3/Sb@graphene) *via* microwave plasma irradiation and

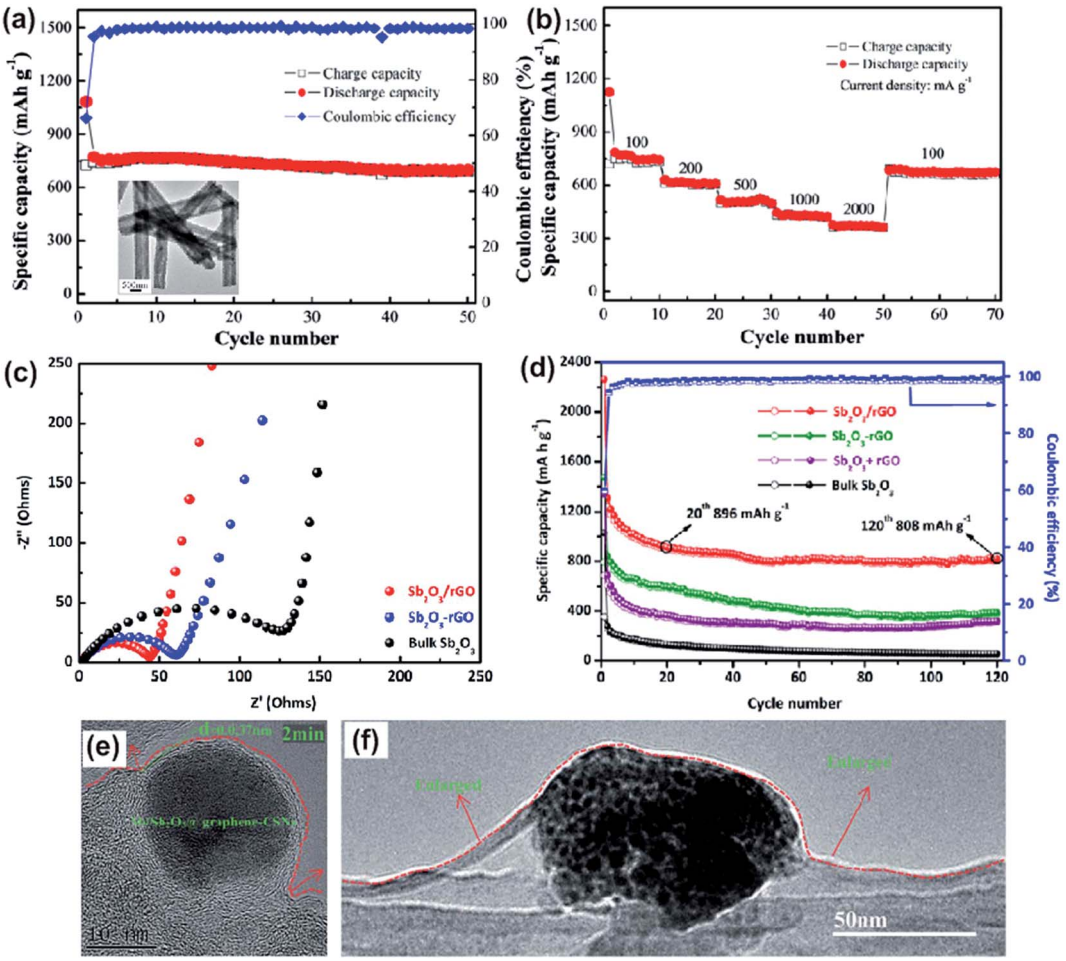

Fig. 15 (a) Cycle performance and (b) rate performance of tube-like Sb_2O_4 submicron-structures. Reproduced with permission.[197] Copyright 2017, Elsevier. (c) Nyquist plots of Sb_2O_3/rGO (with L-AA) and Sb_2O_3–rGO (without L-AA) composite electrodes and a bulk Sb_2O_3 electrode at an open-circuit potential. (d) Cycling performance and coulombic efficiencies of the Sb_2O_3/rGO electrode at 100 mA g^{-1}, in comparison with that of the Sb_2O_3–rGO composite, Sb_2O_3 + rGO mixture, and bulk Sb_2O_3. Reproduced with permission.[27] Copyright 2017, American Chemical Society. TEM micrographs of an encapsulated nanoparticle of Sb_2O_3/Sb@graphene–CSN (e) before and (f) after the cycling process. Reproduced with permission.[154] Copyright 2015, Royal Society of Chemistry.

a subsequent graphene growth procedure.[56] The designed structure, Sb_2O_3/Sb@graphene nanoparticles anchored on carbon sheet networks (Sb_2O_3/Sb@graphene–CSN), provided an ultra-thin and flexible graphene shell to accommodate volume changes and introduce a large effective area, good conductivity, and short transportation length for both Na^+ ions and electrons. The HR-TEM image in Fig. 15e clearly reveals the structure of the few-layer graphene encapsulated Sb_2O_3/Sb nanoparticles. Upon sodiation, the Sb_2O_3/Sb core expanded with the insertion of Na^+ ions. The graphene shell was accordingly enlarged by the volume expansion of the core and partly detached from the carbon sheet, but it maintained good electrical contact. After desodiation, the initial core–shell structure was retained and appeared to remain in good contact with the carbon sheet networks. The Sb_2O_3/Sb cores were pulverized into small particles; however, they were still well encapsulated in the graphene shells, as shown in Fig. 15f. With these structural merits, the Sb_2O_3/Sb@graphene–CSN exhibited excellent electrochemical cycling stability for sodium storage. The composite showed a desodiation capacity retention of 92.7% after 275 cycles at a current density of 0.1 A g^{-1}. By contrast, Sb_2O_3/Sb–CSN without graphene shells suffered from serious capacity decay owing to the pulverization and exfoliation of the active materials.

Recent studies showed that bimetallic oxides with two different metal cations exhibit improved electrochemical properties due to interfacial effects and the synergistic effects of the multiple metal species. $ZnSb_2O_6$ nanoparticles were reported to exhibit advanced lithium storage properties.[138] Specifically, they demonstrated a high reversible capacity of 513 mA h g^{-1} at 100 mA g^{-1} after 100 cycles, a long cycle life with a reversible capacity of 394 mA h g^{-1} after 300 cycles at 500 mA g^{-1}, and a high rate capacity of 315 mA h g^{-1} at 2000 mA g^{-1}. Jibin *et al.* prepared $CoSb_2O_4$ and $NiSb_2O_4$ anode materials for LIBs using a solid state synthesis method.[97] The $CoSb_2O_4$ and $NiSb_2O_4$ displayed similar electrochemical behavior, with a reversible capacity of 490 and 412 mA h g^{-1}, respectively, in the first cycle.

4.1.4 Antimony sulfide. Antimony sulfide is an anisotropic material with a layered structure and has a tendency to grow along the [001] direction to form wire/rod shapes.[16] Similar to antimony oxide materials, antimony sulfide has been considered a promising anode material for LIBs and SIBs because of its high theoretical capacity.[28,75,149,159,198] The main challenge for antimony sulfide is accommodating the large volume changes during sodiation/desodiation processes. Zhang's group synthesized a flower-like Sb_2S_3 structure assembled from nanosheets and tested it as an anode material for SIBs.[149] This material delivered a high reversible capacity of 835.3 mA h g^{-1} after 50 cycles at 50 mA g^{-1} and retained a capacity of 641.7 mA h g^{-1} after 100 cycles at 200 mA g^{-1} (Fig. 16a). When the current density increased to 2000 mA g^{-1}, a high specific capacity of 553 mA h g^{-1} was obtained, corresponding to 72% capacity retention. The enhanced cycling stability and rate capability resulted from the 2D nanosheet structure, which not only accommodated the strain generated during cycling, but also shortened the diffusion paths for Na^+ ions and electrons. Hou *et al.* investigated the sodium storage properties of 1D rod-like Sb_2S_3 covered by a thin carbon layer on the surface (Sb_2S_3@C).[77] Fig. 16b reveals that the Sb_2S_3@C delivered a high specific capacity of 699.1 mA h g^{-1} at 100 mA g^{-1} after 100 cycles, corresponding to 95.7% of the initial capacity. Moreover, a high reversible capacity of 429 mA h g^{-1} was retained at a high current rate of 3200 mA g^{-1}. This electrochemical performance is attributed to the thin carbon layers, which alleviate the strain caused by the large volume changes during cycling and simultaneously enhance the conductivity of the electrode.

Lu and co-workers reported Sb_2S_5 nanoparticles (~5 nm) uniformly encapsulated in 3D porous graphene foam (Sb_2S_5–

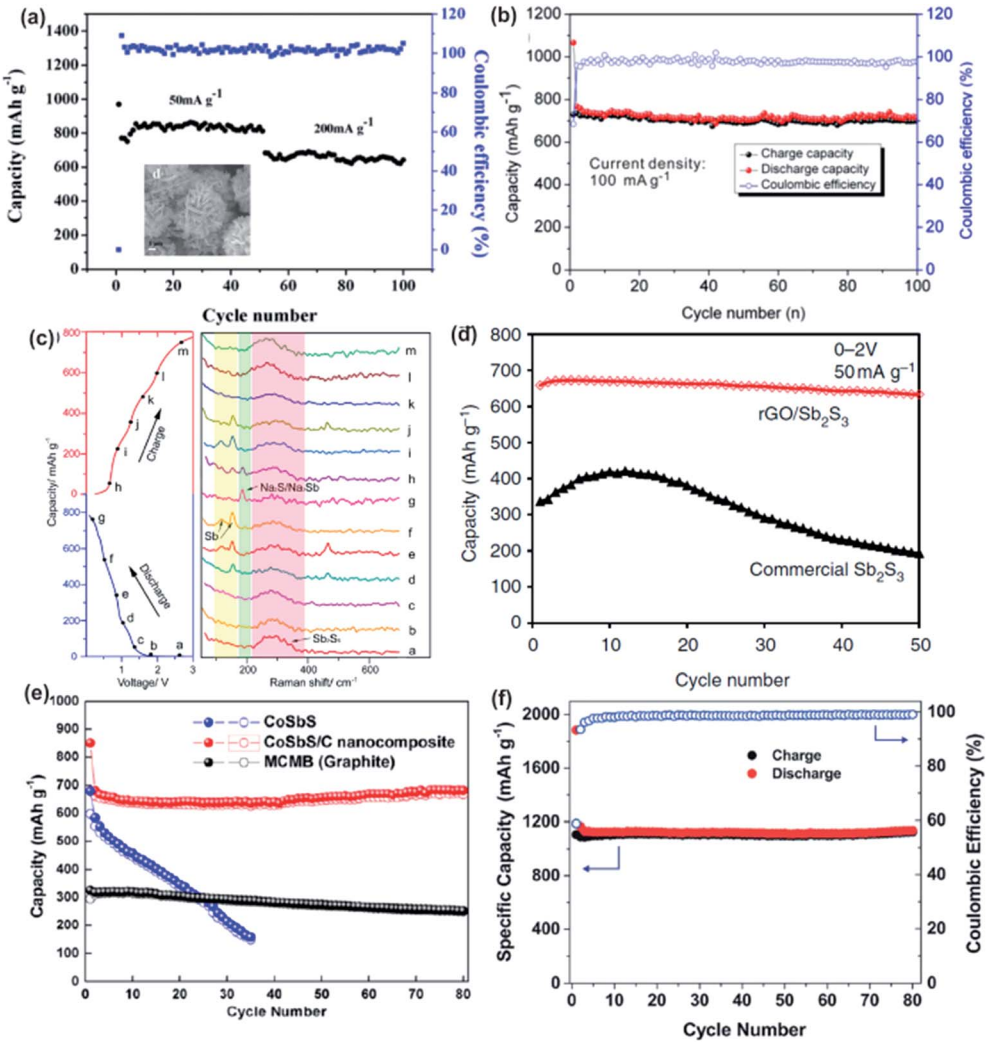

Fig. 16 (a) Cycle performance of Sb_2S_3 at a current rate of 50 and 200 mA g^{-1}, respectively. Reproduced with permission.[149] Copyright 2015, Royal Society of Chemistry. (b) Cycle performances of Sb_2S_3@C rods. Reproduced with permission.[77] Copyright 2015, American Chemical Society. (c) *In situ* Raman spectra of an Sb_2S_5–GF electrode collected in the second cycle with a current density of 0.1 A g^{-1}. Reproduced with permission.[28] Copyright 2017, American Chemical Society. (d) Cycle performance of bulk Sb_2S_3 and rGO/Sb_2S_3 at 50 mA g^{-1}. Reproduced with permission.[47] Copyright 2013, Nature. (e) Cycle performances of a CoSbS/C nanocomposite electrode at 100 mA g^{-1}. Reproduced with permission.[94] Copyright 2013, Elsevier. (f) Cycling performance and corresponding coulombic efficiencies of an In–Sb–S framework at 143 mA g^{-1}. Reproduced with permission.[158] Copyright 2017, Royal Society of Chemistry.

GF) as an anode material for SIBs.[28] The sodiation and desodiation processes were studied using an *in situ* Raman technique, as shown in Fig. 16c. Upon sodiation, Sb_2S_5 peaks gradually decreased with the emergence of Na_xS and Sb. At the end of sodiation, the Na_3Sb and Na_2S peaks were clearly observed without any impurities. During the desodiation process, the Na_3Sb and Na_2S peaks gradually disappeared, accompanied by the emergence of Na_xS and Sb. Finally, Sb_2S_5 could again be observed at the end of desodiation, with the intermediate products vanishing entirely. The experimental results suggest a reversible reaction of $Sb_2S_5 + 16Na \leftrightarrow 5Na_2S + 2Na_3Sb$ during cycling, contributing to a theoretical capacity of 1061 mA h g^{-1}. These binder- and current collector-free electrodes demonstrated a high reversible capacity of 845 mA h g^{-1} at 0.1 A g^{-1}, indicating that the specific capacity of pure Sb_2S_5 was close to the theoretical capacity. Moreover, they delivered a high cycling stability, with 91.6% capacity retention after 300 cycles at 0.2 A g^{-1}, and a high rate capacity of 525 mA h g^{-1} at 10 A g^{-1}. The excellent sodium storage properties of Sb_2S_5–GF are attributable to the synergistic effect of the ultra-small Sb_2S_5 nanoparticles and the 3D porous graphene foam, which significantly shorten the diffusion path for Na^+ ions, increase the electrical conductivity, and facilitate the strain relaxation of Sb_2S_5 during cycling. Lev's group reported an rGO/Sb_2S_3 composite with Sb_2S_3 uniformly coating the graphene.[47] When evaluated as an anode material for SIBs, the rGO/Sb_2S_3 demonstrated a reversible capacity of around 670 mA h g^{-1}, with a capacity retention of ~95% after 50 cycles (Fig. 16d). They also conducted full cell testing by coupling the rGO/Sb_2S_3 with a $Na_{2/3}Ni_{1/3}Mn_{2/3}O_2$ cathode, showing the potential feasibility of achieving only a small amount of degradation after 10 cycles.

Furthermore, Lee and co-workers reported a ternary compound (CoSbS) and carbon nanocomposite (CoSbS/C) synthesized using a facile solid-state method and investigated its electrochemical performance in LIBs.[94] This nanocomposite showed excellent electrochemical stability, with a high specific capacity of 666 mA h g^{-1} after 80 cycles (Fig. 16e) and a high rate capacity of 555 mA h g^{-1} at a current rate of 3C. This high electrochemical performance resulted from the uniform distribution of the CoSbS nanocrystallites within the amorphous carbon matrix. Zhang's group synthesized a crystalline In–Sb–S framework.[158] The as-obtained material had a 2D layer structure with cationic ammonium and molecular phen in the interlayers. With these unique structural features, it demonstrated a high capacity of 1138 mA h g^{-1} after 80 cycles, exhibiting a remarkably high retention of 97.6% of its second discharge capacity (Fig. 16f).

4.1.5 Other Sb-based anode materials. In addition to metallic Sb, Sb-based alloys, antimony oxides, and antimony sulfides, other Sb-based materials such as Sb_2Se_3 have also been applied in LIBs and SIBs.[52,67,88,186,199–202] Mai's group fabricated an ultralong Sb_2Se nanowire-based free-standing membrane anode for LIBs and SIBs.[67] When evaluated in LIBs, it delivered high initial discharge and charge capacities of 836 and 630 mA h g^{-1} at 100 mA g^{-1}, respectively (Fig. 17a). After 50 cycles, a reversible capacity of 614 mA h g^{-1} remained, with a capacity retention of 95% (Fig. 17b). Compared to LIBs, this free-standing membrane electrode delivered a relatively inferior

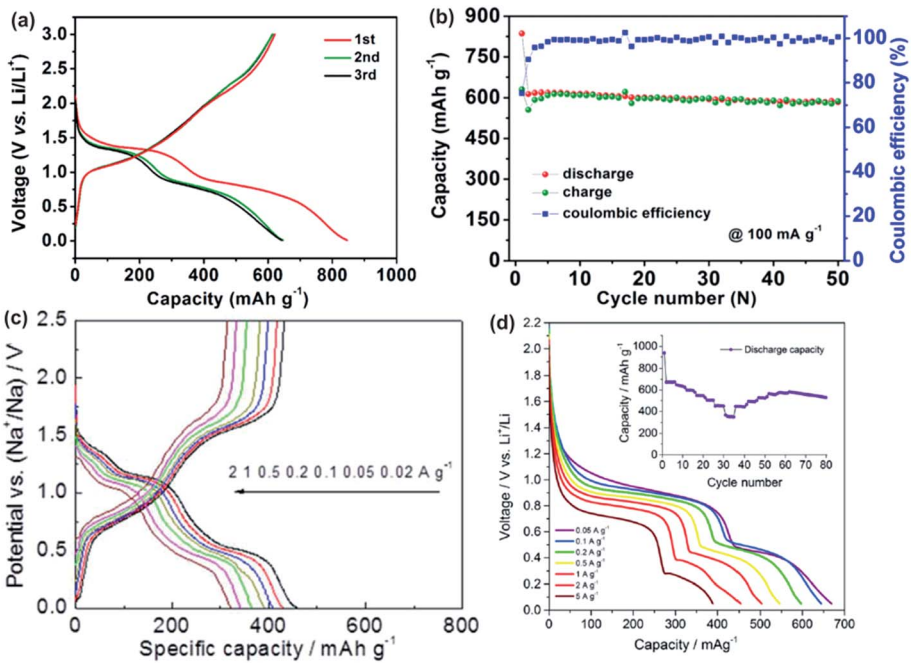

Fig. 17 (a) Charge–discharge profiles and (b) cycling performance and corresponding coulombic efficiency of an Sb_2Se_3 ultralong nanowire-based membrane as a LIB anode. Reproduced with permission.[67] Copyright 2016, American Chemical Society. (c) Discharge curves of an Sb_2Te_3/C electrode at various current densities. Reproduced with permission.[199] Copyright 2017, Elsevier. (d) Rate capability test of $Mn_2Sb_3O_6Cl$ showing the discharge voltage profiles and gravimetric discharge capacity retention (inset) for a series of current densities applied in sequence. Reproduced with permission.[52] Copyright 2017, American Chemical Society.

sodium storage performance, showing a reversible capacity of only 360 mA h g^{-1} at 100 mA g^{-1} and 80% capacity retention after 50 cycles. The difference in electrochemical performance could originate from the large radius of sodium ions, which would lead to a more complex sodiation process relative to the lithiation process. Yang *et al.* synthesized Sb_2Te_3 nanocrystals with a size of about 20 nm embedded in a carbon matrix (Sb_2Te_3/C).[199] The as-prepared Sb_2Te_3/C showed good rate capability (Fig. 17c). The values of the charge capacity were 437, 381, and 314 mA h g^{-1} when the current densities were 20, 200, and 2000 mA g^{-1}, respectively. After returning to 20 mA g^{-1} from the high current rates, the capacity quickly recovered to 409 mA h g^{-1}. Moreover, the as-obtained Sb_2Te_3/C demonstrated a specific capacity of 360 mA h g^{-1}, with a capacity retention of 93% after 400 cycles at 1 A g^{-1}. An *in situ* TEM observation confirmed that the synergistic effects of nanosized particles and the carbon matrix not only efficiently released stress during volume changes, but also prevented the aggregation of pulverized nanoparticles, which could be responsible for the excellent electrochemical properties. A Sb_3N thin film was successfully synthesized by the magnetron sputtering method, and its lithium storage properties were investigated for the first time.[53] The voltage profiles of Sb_3N/Li cells between 0.3 V and 3.0 V revealed reversible capacities above 600 mA h g^{-1} over 50 cycles, which was much better than that of an Sb thin film prepared by the same sputtering method. The selected area electron diffraction measurements revealed that the Sb_3N converted into Li_3Sb and Li_3N during the lithiation process.

Some Sb-based compounds that possess more complex compositions and crystal structures have also shown reasonable electrochemical performance.[52,69,76,88,200–206] $Ni_3Sb_4O_6F_6$, which belongs to the group of oxohalides, was investigated with respect to its lithium storage properties.[69] *In situ* and *ex situ* XRD characterization showed that the crystal structure of $Ni_3Sb_4O_6F_6$ collapsed with the insertion of Li^+ ions and gradually transformed into an amorphous phase. With continued lithiation, a nanocrystalline phase of NiSb formed and appeared reversibly in the subsequent cycles. Experimental results revealed that multiple processes, including the conversion and alloying reactions that occurred during cycling, contributed to a high initial discharge capacity of ~970 mA h g^{-1}. Another quaternary layered $Mn_2Sb_3O_6Cl$ compound was investigated as an anode material for LIBs.[52] Operando XRD, HR-TEM, and SAED measurements revealed that two pairs of reactions, the alloying of Li–Sb and the conversion of Mn_xO_y to metallic Mn^0 and Li_2O upon lithiation, were mainly responsible for the reversible lithium storage properties. A high reversible capacity of 780 mA h g^{-1} between 0.05 and 2.2 V was obtained in the first cycle, which decreased to 466 mA h g^{-1} after 100 cycles, with a capacity retention of around 60%. This compound also exhibited a good rate capability, as shown in Fig. 17d. At a high current density of 5 A g^{-1}, the electrode delivered a capacity of 400 mA h g^{-1}, corresponding to 65% of the initial capacity at a slow rate. The high electrical conductivity of Sb associated with its relatively simple lithiation/delithiation processes was expected to promote fast kinetics.

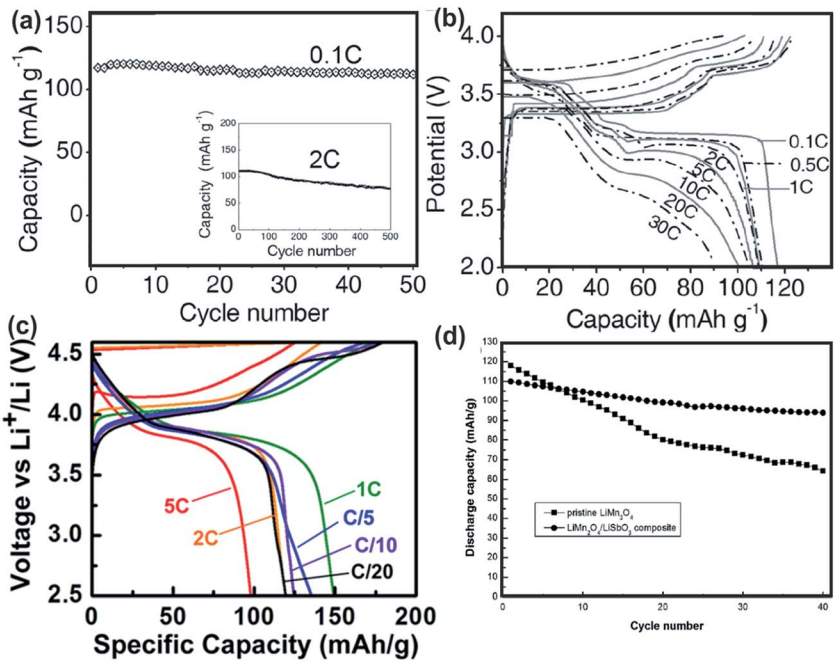

Fig. 18 (a) The capacity retention of a $Na_3Ni_2SbO_6$ electrode at 0.1C and the capacity retention of such cells at 2C (400 mA g^{-1}) (inset). (b) Rate capability of the cells at constant charge/discharge rates of 0.1C (20 mA g^{-1})–30C (6000 mA g^{-1}). Reproduced with permission.[105] Copyright 2014, Wiley. (c) First cycle voltage curves of LNSO-15 obtained from galvanostatic cycling between C/20 and 5C. Reproduced with permission.[162] Copyright 2017, American Chemical Society. (d) Cycling behavior of pristine $LiMn_2O_4$ and $LiMn_2O_4$/$LiSbO_3$ composites. Reproduced with permission.[209] Copyright 2014, Royal Society of Chemistry.

Table 3 Summary of the Li/Na-storage performance of typical Sb-based electrode materials[a]

Types of materials	Current density[a] [mA g^{-1}]	Cut-off voltage [V]	Cycle number	Specific capacity[b] [mA h g^{-1}]	Ref.
For Li-ion batteries					
Hexagonal Sb	100 (2000)	0.01–2.0	50	645 (422)	147
Amorphous Sb	100 (2000)	0.01–2.0	50	634 (379)	147
$Sb/Al_4C_3/C$	100	0.0–2.0	200	520	172
$Sb–AlO_x–C$	100 (2500)	0.0–2.0	100	455 (487)	83
$Sb–TiO_x–C$	100 (2500)	0.0–2.0	100	438 (∼415)	83
$Sb–MoO_x–C$	100 (2500)	0.0–2.0	100	393 (∼370)	83
rGO–Sb–Ni sandwich structure	100 (1000)	0.01–2.0	50	424 (158)	82
$Sb@TiO_2$ 1D composite	100 (2000)	0.01–3.0	100	450 (340)	170
Sb/C polyhedral composite	1000 (5000)	0.01–2.0	500	401 (315)	80
1D Sb/N-doped porous C	200 (5000)	0.01–2.5	100	556 (312)	10
Hollow Sb@C yolk–shell spheres	1000 (2000)	0.01–2.6	300	405 (385)	79
Sb nanocrystals (20 nm size)	330 (13 200)	0.02–1.5	100	∼645 (∼540)	36
$Sb/MoS_2/C$ composite	200 (5000)	0.01–3.0	250	680 (353)	207
NiSb-embedded C hollow spheres	100 (2000)	0.01–2.6	100	497 (302)	60
SnSb nanorods in CNTs	180	0.1–1.2	80	672	142
SbSb–C fibers	200 (5000)	0.05–2.0	100	590 (210)	131
InSb	—	0.65–1.4	12	∼250	208
$TiSb_2$	∼55	0.05–1.5	100	275	26
$NbSb_2$	∼48	0.05–1.5	100	90	26
$NiSb–Al_2O_3–C$	100 (1050)	0.0–2.0	1000	280 (∼270)	174
Ag_3Sb	0.16 mA cm^{-2}	0.0–1.2	40	∼280	101
Mg_3Sb_2	0.4 mA cm^{-2}	0.0–2.0	13	150	89
Cu_2Sb nanoparticle clusters	81 (1296)	0.01–1.5	180	312 (228)	111
Porous-Ni-scaffold@SnSb	2000 (6000)	0.01–2.0	100	580 (∼450)	32
Sb_6O_{13}/rGO	100 (3000)	0.01–3.0	140	1090 (201)	33
Sb_2O_3/rGO	600 (5000)	0.0001–3.0	700	525 (188)	27
$ZnSb_2O_6$	100 (2000)	0.01–3.0	100	513 (315)	138
$rGO–Sb_2S_3$	250 (2000)	0.0–2.5	50	720 (480)	159
CoSbS/C	100 (2040)	0.0–2.5	80	666 (555)	94
Bulk Sb_2S_3 (10–20 μm)	250 (2000)	0.0–2.5	50	∼730 (580)	73
$Ni_3Sb_4O_6F_6$	80	0.4–2.2	100	∼200	69
Sb_3N	0.02 mA cm^{-2}	0.3–3.5	55	∼700	53
$Mn_2Sb_3O_6Cl$	50 (5000)	0.05–2.2	100	467 (∼400)	52
Sb_2Se_3 nanowire membrane	100 (1600)	0.01–3.0	50	584 (255)	67
$(NH_4)InSb_2S_5 \cdot phen$	143 (3570)	0.005–3.0	80	1138 (607)	158
$Li_{1.15}Ni_{0.47}Sb_{0.38}O_2$ (cathode)	∼220 (∼1100)	2.5–4.6	20	∼95 (∼107)	162
$LiMn_2O_4/LiSbO_3$ (cathode)	0.25 mA cm^{-2}	2.85–4.8	40	94	209
For Na-ion batteries					
Hexagonal phase Sb	100 (2000)	0.01–2.0	50	610 (∼400)	147
Amorphous Sb	100 (2000)	0.01–2.0	50	605 (∼100)	147
Sb@C microspheres	180 (4800)	0.0–2.0	300	456 (190)	71
Sb/NPC	100 (3200)	0.01–2.0	100	530 (287)	179
Sb/C fibers	100 (6000)	0.0–2.0	300	350 (88)	136
$Sb@TiO_{2-x}$ nanotubes	2640 (13 200)	0.0–2.5	1000	∼300 (312)	55
Sb/multilayer graphene	100 (5000)	0.01–2.0	200	405 (210)	153
Sb@C coaxial nanotubes	100 (20 000)	0.01–2.0	240	407 (310)	106
Nanoporous Sb	100 (3300)	0.1–1.5	200	574 (420)	38
Cypress leaf-like Sb	100 (3200)	0.01–2.0	120	629 (300)	182
G@Sb@C	100 (5000)	0.01–2.0	200	570 (433)	41
Fern leaf-like Sb	500 (10 000)	0.01–2.0	150	589 (498)	118
Sb@S, N-3D-porous C	100 (5000)	0.001–2.0	500	450 (160)	171
Sb@C yolk–shell structure	500 (5000)	0.02–2.0	200	510 (315)	31
Spherical nano-Sb@C	100 (10 000)	0.01–2.0	500	385 (146)	146
Porous Sb/Sb_2O_3 nanocomposite	660 (10 000)	0.02–1.5	180	540 (412)	125
Sb nanocrystal	660 (13 200)	0.02–1.5	250	550 (∼535)	181
Sb hollow nanospheres	50 (1600)	0.01–2.0	50	622 (315)	81
Sb microparticles (sol–gel method)	330 (5280)	0.02–1.5	120	480 (356)	127
Bulk Sb	330 (2640)	0.02–1.5	160	576 (528)	35
1D Sb/N-doped porous C	100 (5000)	0.01–2.5	100	401 (50)	10
Hollow Sb@C yolk–shell spheres	1000 (2000)	0.01–2.6	200	280 (279)	79
Sb nanocrystals (20 nm size)	660 (13 200)	0.02–1.5	100	∼570 (∼520)	36

Table 3 (*Contd.*)

Types of materials	Current density[a] [mA g^{-1}]	Cut-off voltage [V]	Cycle number	Specific capacity[b] [mA h g^{-1}]	Ref.
Zn_4Sb_3 films	97	0.01–1.2	250	~400	113
rGO/SnSb nanocomposites	100 (15 000)	0.001–2.5	80	361 (85)	78
Cu_2Sb nanoparticles on Cu foil	800 (8000)	0.05–2.0	200	270 (256)	51
$Sn_{50}Ge_{25}Sb_{25}$	85 (8500)	0.01–2.0	50	662 (381)	59
Zn_4S_3 nanowires	414 (2070)	0.01–2.0	200	~300 (187)	42
$Bi_{0.57}Sb_{0.43}$–C	100 (1000)	0.05–2.0	50	293 (326)	58
NiSb hollow spheres	600 (6000)	0.01–2.0	150	400 (230)	65
Porous-Ni-scaffold@SnSb	1000 (5000)	0.01–2.0	1000	275 (360)	32
Sb/Sb_2O_3	66 (3300)	0.0.1–2.5	100	615 (212)	114
Sb_2O_4 thin film	18	0.01–3.5	20	724	130
Sb_2O_3/Sb@graphene-CSN	100 (5000)	0.001–2.0	275	487 (221)	154
SbO_x@C-flakes	100 (4000)	0.01–2.0	100	442 (114)	167
Sb_2S_3@C rods	100 (3200)	0.01–2.5	100	699 (429)	77
Flower-like Sb_2S_3	200 (2000)	0.01–2.0	100	642 (553)	149
rGO/Sb_2S_3	50 (3000)	0.0–2.0	50	~637 (520)	47
Sb_2S_5-graphene foam	200 (10 000)	0.1–3.0	300	748 (525)	28
Sb_2Se_3 nanowire membrane	100 (1600)	0.01–2.0	50	289 (153)	67
1D yolk–shell Sb@Ti–O–P	500 (10 000)	0.02–2.5	200	760 (360)	152
$(NH_4)InSb_2S_5 \cdot phen$	50 (938)	0.005–3.0	50	340 (439)	159
$Na_3Ni_2SbO_6$ (cathode)	20 (6000)	2.0–4.0	50	110 (90)	105

[a] The current density values in brackets of column[a] correspond to the specific capacity values in brackets of column[b].

In addition, Shaijumon's group prepared a $Sb_4O_5Cl_2$/graphene aerogel composite and evaluated its lithium storage properties.[204] The graphene interconnected networks effectively facilitated the charge transfer and alleviated the structural variation of $Sb_4O_5Cl_2$ during cycling, which provided the $Sb_4O_5Cl_2$/graphene electrode with a good cycling performance with a reversible capacity of 600 mA h g^{-1} after 50 cycles at a current density of 50 mA g^{-1}. $PbSbO_2Cl$ and $PbCl_2/Sb_4O_5Cl$ anode materials were reported by Shu's group, which showed high initial lithiation capacities of 993.8 mA h^{-1} and 1036.7 mA h g^{-1}, respectively.[205] Nie *et al.* used a surfactant-thermal strategy to synthesize crystalline thioantimonate $[NH(CH_3)_2][Sb_4S_5(S_3)]$, which was constructed from 1D $[Sb_4S_5(S_3)]$ neutral ribbons and dimethylamine molecules.[206] After grinding, ultrathin nanosheets with a thickness of around 20 nm were obtained. With the merits of its 2D structure, the $[NH(CH_3)_2][Sb_4S_5(S_3)]$ anode material delivered a high reversible specific capacity of 568 mA h g^{-1} over 50 cycles at 0.1 A g^{-1} and an excellent rate capability of 301 mA h g^{-1} at 5 A g^{-1}.

4.2 Sb-based cathode materials

Sb-based materials have also been applied as cathode materials for LIBs and SIBs, revealing high rate capability and good cycling stability.[99,105,162,163,209] Yang's group focused on layered alkali-transition metal oxides, $Na_3M_2SbO_6$ (M = Ni, Cu, Co, Zn, *etc.*), which are O_3-type honeycomb-ordered phases.[105] Generally, O3-type Na_xMO_2 materials can accommodate Na^+ ions reversibly even though their reversible capacities are limited to below 120 mA h g^{-1}. $Na_3Ni_2SbO_6$ was confirmed to have a considerably high capacity, excellent rate capability, and cycling stability. In the crystal structure of $Na_3Ni_2SbO_6$, each SbO_6 octahedron was surrounded by six NiO_6 edge-sharing octahedrons to form a superstructure lattice, and the Na^+ ions were hosted in-between the Ni_2SbO_6 slabs. During charging and discharging, this layered compound underwent complicated phase transformations. However, XRD patterns confirmed that the desodiation/sodiation reactions occurred with reversible three-phase transformations of the layered compound (O3-$Na_3Ni_2SbO_6$ ↔ P3-$Na_2Ni_2SbO_6$ ↔ O1-$NaNi_2SbO_6$). When evaluated in coin-type cells at 20 mA g^{-1} using Na metal as the counter electrode, $Na_3Ni_2SbO_6$ delivered an initial charge and discharge capacity of 122 and 117 mA h g^{-1}, respectively, with a high columbic efficiency up to 95%. The initial specific capacities corresponded to 58% of its theoretical 3 Na^+ ion reaction capacity (199 mA h g^{-1}). The high initial efficiency and reaction demonstrated that $Na_3Ni_2SbO_6$ has excellent electrochemical reversibility and strong corrosion resistance. After 50 cycles, it retained a high reversible capacity of 110 mA h g^{-1}, corresponding to a capacity retention of 95% (Fig. 18a). This layered cathode also demonstrated long cycle stability, with 70% capacity retention after 500 cycles at 40 mA g^{-1}. Moreover, $Na_3Ni_2SbO_6$ revealed a remarkably high rate performance (Fig. 18b). Even at 20C, it delivered a high discharge capacity of 100 mA h g^{-1}. The high Na^+ ion diffusion coefficient of $Na_3Ni_2SbO_6$ (2.3×10^{-9} cm^2 s^{-1}) is likely responsible for the excellent rate performance.

Ceder's group studied the electrochemical behavior of lithium-excess $Li_xNi_{2-4x/3}O_2$ cathode materials at slow and fast rates.[162] Interestingly, they found that $Li_{1.15}Ni_{0.47}Sb_{0.38}O_2$ exhibited higher discharge capacities at faster rates (Fig. 18c). When they characterized the redox activity of nickel, antimony, and oxygen at slow and fast rates, they found that nickel migration was responsible for the anomalous rate behavior. Cui *et al.* prepared a $LiMn_2O_4/LiSbO_3$ nanocomposite and investigated its lithium storage properties as a cathode material.[209]

This composite consisted of spherical nanoparticles ranging in size from 20 to 100 nm. Fig. 18d shows that a reversible capacity of ~94 mA h g^{-1} was retained after 40 cycles for the composite, which was much better than that of pure $LiMn_2O_4$. $LiSbO_3$ was supposed to buffer the structural distortion in the $LiMn_2O$ host during the repeated insertion and extraction of lithium ions and improve the structural stability of the $LiMn_2O_4$ electrode.

A comparison of the electrochemical performances of typical Sb-based electrode materials in LIBs and SIBs is given in Table 3. It can be observed that almost all kinds of Sb-based electrode materials delivered high specific capacities because of the intrinsic alloying and conversion mechanisms. However, these Sb-based active materials exhibited different levels of cycling stability and rate capability due to the difference in compositions and structures. Therefore, a rational design is essential to enhance the electrochemical properties of Sb-based electrode materials. The combination of nanostructured Sb-based materials with carbonaceous materials has been proved to be a promising strategy for potential commercial application.

5. Applications of antimony in liquid-metal batteries

Large-scale stationary energy storage is critical in facilitating the grid reliability and utilization and integration of renewable energy sources. However, the high cost of conventional batteries combined with their relatively short cycle life limits their real applications for grid energy storage. LMBs have attracted increasing attention as a novel battery technology because of their low cost, ultra-long cycle life, and facile cell fabrication.[7,48,49,210–218]

A liquid-metal battery is composed of two liquid metal electrodes separated by a molten salt electrolyte, which self-segregate into three layers based on density and immiscibility (Fig. 19a).[7,48,219] The negative electrode A on the top is a low-density liquid metal that readily donates electrons. The positive electrode B at the bottom is a high-density liquid metal that readily accepts those electrons. The electrolyte in the middle is a molten salt that transfers charged particles and won't mix with either of the electrode materials. The strong interaction between metals A and B provides the thermodynamic driving force (battery potential) for LMBs. Upon discharge, the negative electrode (metal A) is electrochemically oxidized ($A \rightarrow A^{x+} + xe^-$), and the cations A^{x+} are conducted across the molten salt electrolyte to the positive electrode as electrons are released to an external circuit, which reduces the thickness of the top layer A. Meanwhile, the cations are electrochemically reduced to form a liquid A–B alloy [$A^{x+} + xe^- \rightarrow$ A (in B)], leading to a growing thickness of the positive electrode layer. This process is reversed upon charging.

The working mechanism demonstrates that the creation and annihilation of the liquid metal electrodes are continuous

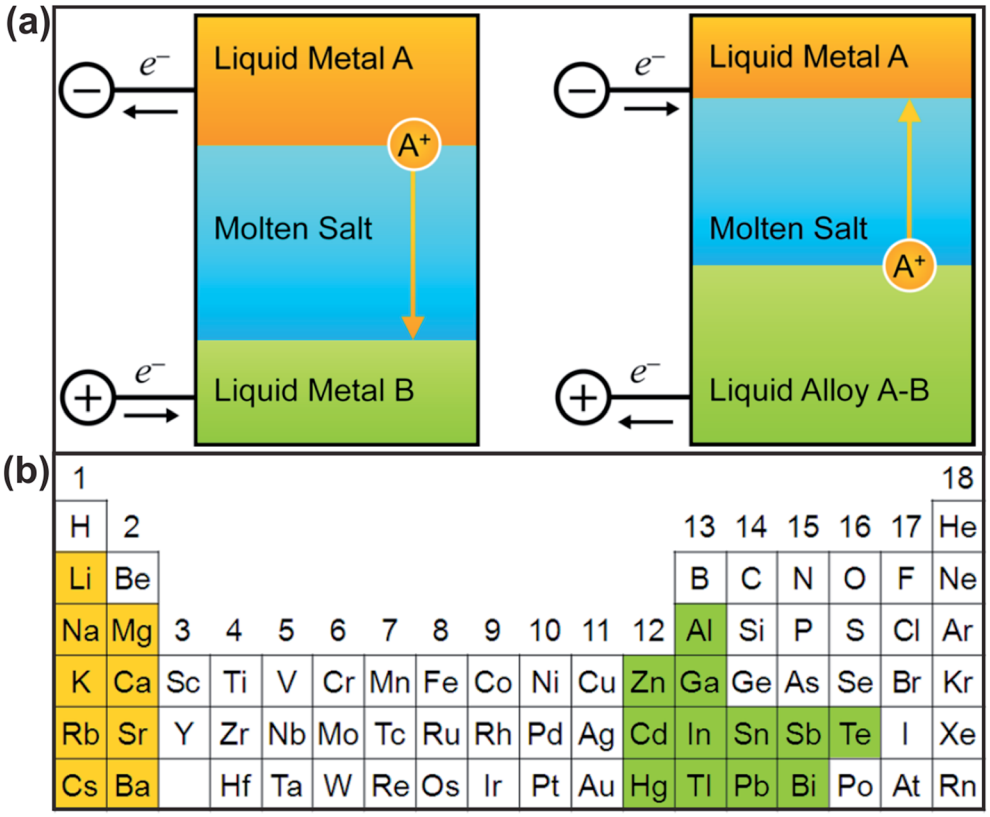

Fig. 19 Schematic diagram of a liquid-metal battery upon (a) discharging and charging. (b) Negative (orange) and positive (green) electrode material candidates for liquid metal batteries. Reproduced with permission.[7] Copyright 2013, American Chemical Society.

during the discharge and charge processes, which contributes to an unprecedented cycle life for LMBs by avoiding the microstructural electrode degradation mechanisms of a conventional battery. However, the high operating temperatures (typically above 200 °C), relatively low equilibrium cell voltages (generally lower than 1.0 V), and high self-discharge rates are significant challenges to the practical application of LMBs.[7] Generally, a high operating temperature leads to higher rates of corrosion and detracts from the overall storage efficiency, which finally increases the cost of the whole system.[49] An appropriate combination of electrode metals and electrolyte salts with widespread natural availability and a low melting point could effectively solve these problems. Possible compositions for liquid metal electrodes highlighted in the periodic table are shown in Fig. 19b.[7] Among these elements, Sb has been considered as a promising positive electrode candidate for LMBs owing to its high electronegativity, low-cost, and high open circuit voltage (OCV). Based on these merits, Sadoway's group first reported an Sb-based LMB with liquid Mg as the negative electrode, liquid Sb as the positive electrode, and NaCl–KCl–$MgCl_2$ as the electrolyte.[210] The Mg–Sb cells were tested at 700 °C due to the high melting point of Mg (648 °C) and Sb (630 °C). When cycled at 50 mA cm^{-2}, the LMB exhibited a round-trip coulombic efficiency of 94% and an energy efficiency of 69% (Fig. 20a). It also delivered discharge voltages of 0.35 and 0.21 V at 100 and 200 mA cm^{-2}, respectively (Fig. 20b). However, the high operating temperature, low cell voltage, relatively high cost ($375 kW h^{-1}), and the limited rate capability make Mg–Sb LMBs impractical for real applications.

The combination of Li and Sb is an attractive choice due to the high cell voltage of 0.92 V. In addition, the low melting point of Li and its low solubility in melted lithium halides offer high energy efficiency. However, the high melting point of Sb makes the operating temperature still remain at 500 °C. Alloying Sb with another metal could be an effective strategy to lower the melting point of the positive electrode. Therefore, Sadoway's

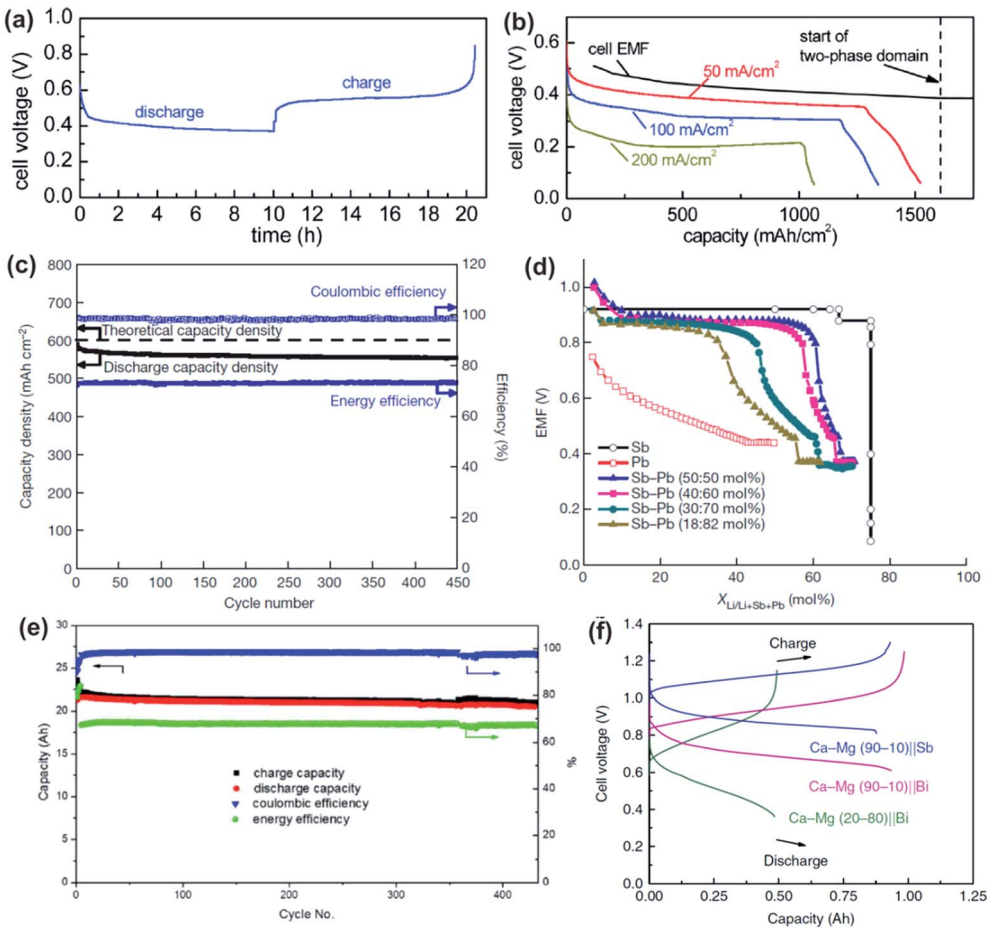

Fig. 20 Electrochemical performance of a Mg||Sb liquid metal battery operated at 700 °C. (a) Variation of the cell voltage with the state of charge over one cycle. The current was set at 50 mA cm^{-2}. (b) Deep discharge results at different current rates. Reproduced with permission.[210] Copyright 2012, American Chemical Society. (c) Coulombic efficiency, energy efficiency, and discharge capacity density of a Li||Sb–Pb cell cycled at 275 mA cm^{-2} with a fully discharged target composition of 45% Li in an Sb–Pb 30 : 70 mol% alloy. (d) Electromotive force (EMF) as a function of Li concentration in Sb–Pb alloys. Reproduced with permission.[49] Copyright 2014, Nature. (e) Charge and discharge capacity, coulombic efficiency, and energy efficiency of a Li||Sb–Sn cell tested at 300 mA cm^{-2}. Reproduced with permission.[218] Copyright 2016, American Chemical Society. (f) Charge–discharge voltage time traces of Ca–Mg (20–80 mol%)||Bi, Ca–Mg (90–10 mol%)||Bi, and Ca–Mg (90–10 mol%)||Sb operated at a current density of 200 mA cm^{-2} and 650 °C. Reproduced with permission.[212] Copyright 2016, Nature.

group further designed a Li–Sb–Pb LMB that used liquid Li and a liquid Sb–Pb alloy as the negative and positive electrodes, respectively.[49] The designed Sb–Pb-based LMBs met the performance requirements for grid energy storage applications. Specifically, the cells were tested at 450 °C and exhibited 98% coulombic efficiency and 73% round-trip energy efficiency at a current density of 275 mA cm^{-2}, retaining 94% of the initial capacity after 450 cycles (Fig. 20c). This capacity fade rate was equivalent to 85% retention of the initial capacity after 10 years. Remarkably, the cells using liquid Sb–Pb as the positive electrode could maintain the high cell voltage of the original pure Sb-based cells even when the Pb ratio was as high as 80%, indicating that the electrode potential was primarily determined by the interaction of Li and Sb (Fig. 20d). When tested at a high current density of 500 mA cm^{-2}, the Sb–Pb based cell still delivered a reversible capacity of 87% of its theoretical value. On the basis of this measured cell performance, the costs of these electrode materials were estimated to be one-fifth that of Mg–Sb cells. Considering the potential environmental concerns of Sb for large-scale application, Wang *et al.* reported an environmentally friendly Sb–Sn positive electrode material for LMBs.[218] The prepared Li||Sb–Sn LMBs showed a high discharge voltage of 0.8 V at 100 mA cm^{-2} when tested at 500 °C. Moreover, they exhibited excellent rate performance, with a 13% capacity loss from 100 mA cm^{-2} to 1 A cm^{-2}, good cycling performance, with 96.7% capacity retention after 430 cycles (Fig. 20e), and a low electrode material cost of \$73 kW h^{-1}. These advantages make Li||Sb–Sn LMBs a potential battery candidate for large-scale energy storage without environmental concerns.

Furthermore, Ca||Sb LMBs using LiCl–NaCl–$CaCl_2$ as the electrolyte were investigated and exhibited a high coulombic efficiency of almost 100% at 650 °C.[217] The Ca||Sb cells had a high discharge voltage (0.75–0.95 V), good cycle performance (<0.01% per cycle), and low material cost (<\$90 kW h^{-1}). In addition, a liquid Ca–Mg alloy negative electrode combined with an Sb positive electrode was assembled into LMBs that demonstrated a high cell voltage of 0.88 V and a high energy efficiency of 74% (Fig. 20f).[212]

6. Conclusions and future prospects

In this review, we have briefly introduced the current status of the energy market and pointed out that high-performance energy storage devices are increasingly demanded for portable electronics, electric vehicles, and stationary storage systems. Designing and synthesizing appropriate electrode materials with high performance, abundant natural resources, and low cost is at present the main challenge for rechargeable batteries. This overview further systematically demonstrated that Sb-based materials have become promising electrode candidates for LIBs, SIBs, and LMBs.

For LIBs and SIBs, the present review has summarized recent developments in Sb-based anode materials, including metallic Sb, Sb-based alloys, antimony oxides, antimony sulfides, and some Sb-based cathode materials. We sequentially and systematically introduced the Li/Na-ion storage mechanisms, some typically and widely used synthesis methods, and the applications of various Sb-based electrode materials.[27,35,42,51,55,56,77,83,105,144] For Sb-based active materials, large volume changes upon charging and discharging processes, which pulverize the electrode and lead to serious capacity fading, remain a key issue.[28,31,36,42,154] The rational construction of advanced electrodes, such as engineering nanostructures with pores and void spaces and combining Sb with carbonaceous or other buffer materials, is an effective strategy to improve the electrochemical performance of Sb-based materials. Numerous Sb-based electrode materials with diverse nanostructures and morphologies have been reported, such as nanocrystals, nanowires, hollow spheres, and porous structures.[36–38,42,197] Benefiting from the high specific surface area, short transport path for electrons and ions, and ability to accommodate large volume changes during cycling, Sb-based electrode materials with these unique structures have demonstrated greatly enhanced rate capability and long cycle stability. Combination with carbonaceous materials such as graphene has proved to be another good approach to improving the properties of Sb-based materials because of the buffer function and excellent electrical conductivity of carbon materials.[27,28,31,144]

Although improvements have been achieved, the relatively low initial coulombic efficiency and capacity decay with cycling remain obstacles to the practical application of Sb-based active materials. Therefore, developing high performance Sb-based electrode materials with high specific capacities, excellent rate capability, and long cycling stability is still the primary task facing researchers. Although nanostructured Sb-based electrode materials significantly enhance the cycling and rate performances, they intrinsically suffer from a low-tap density caused by the large interparticle space and high specific surface area. Besides, the large electrode/electrolyte interface results in excess formation of a SEI layer, which lowers the initial coulombic efficiency. These issues largely offset the merits of nanostructured electrode materials over bulk materials. Designing and engineering nano-micro hybrid structures maybe a promising strategy for Sb-based electrode materials, which would show high specific capacities and excellent rate capabilities provided by their nanoscale structure, while retaining the merits of packing density and SEI formation benefiting from the microscale dimensions. In addition, developing facile, efficient, and controllable synthesis methods suitable for mass production is crucial for commercial applications. Currently, these synthetic strategies mentioned above are mainly based on the laboratory scale, some of which are expensive and complicated. For some potential Sb-based electrode materials, more effort is need to improve the synthetic process before realizing industrial production.

Meanwhile, we should also pay more attention to finding other components to well match the obtained Sb-based active materials in real batteries. As shown in this review, most Sb-based materials have been applied as anode materials for LIBs and SIBs. Some corresponding cathode materials such as P2-$Na_{2/3}Ni_{1/3}Mn_{2/3}O_2$ and $Na_3V_2(PO_4)_3$ have been developed for Sb-based anode materials in SIBs and revealed reasonable electrochemical performance.[28,47,50,55] However, the decent ones,

which can make the most of the high specific capacities of Sb-based anode materials, have not been found. Therefore, the design and synthesis of suitable cathode materials to well work with Sb-based anode materials is another big challenge. Finding electrolytes with a stable electrochemical window or optimizing the electrolyte with some additives is also important to Sb-based anode materials.[35,147] For example, the FEC additive in the electrolyte has been proved to be useful for the formation of a stable and uniform SEI layer on the electrode surface, which contributes good structural and cycling stability. Some effort is also needed for developing appropriate binders in future studies. Sb-based anode materials usually suffer from pulverization because of the large volume changes during cycling, which electrically isolate them from the current collector. A suitable binder can alleviate this issue and ensure the integrity and electrical contact of electrodes.[147] In addition, future research should use calculation, simulation, and advanced characterization technologies to further reveal the reaction mechanisms of Sb-based materials, which will provide a theoretical basis for designing appropriate Sb-based electrodes. Given the remaining issues and previous experience, we expect that Sb-based electrode materials will be developed for next-generation LIBs and SIBs.

For LMBs, this review simply introduced the working mechanism and recent developments in Sb-based LMBs.[7,48,49,212,218] The low cost of the liquid metal electrode and molten salt electrolyte, simple electrode assembly process, and unprecedented cycle life make LMBs attractive for large-scale energy storage. However, the elevated operating temperature required and relatively low cell voltage of LMBs make them impractical for real-world applications.[7,49] The introduction of Sb-based positive electrodes effectively addressed some of these issues through the low cost and high OCV of Sb.[49,218] Alloying Sb with Pb or Sn to form Sb–Pb or Sb–Sn liquid positive electrodes significantly reduced the operating temperature while maintaining the high cell voltage. Based on this, other kinds of Sb-based alloys are worth evaluating for LMBs in further studies. Even though much progress has been achieved by applying Sb-based positive electrodes, more effort is still needed to develop practical LMBs with low cost, high cell voltage, and low operating temperature.

Conflicts of interest

There are no conflicts to declare.

Acknowledgements

This work was supported by the "Human Resources Program in Energy Technology" of the Korea Institute of Energy Technology Evaluation and Planning (KETEP), granted financial resource from the Ministry of Trade, Industry & Energy, Republic of Korea (No. 20174010201240) and Basic Science Research Program through the National Research Foundation of Korea (NRF) funded by the Ministry of Science, ICT (2016R1C1B2007299).

References

1 M. S. Whittingham, *Chem. Rev.*, 2004, **104**, 4271–4301.
2 N. Nitta, F. Wu, J. T. Lee and G. Yushin, *Mater. Today*, 2015, **18**, 252–264.
3 S. P. Ong, V. L. Chevrier, G. Hautier, A. Jain, C. Moore, S. Kim, X. Ma and G. Ceder, *Energy Environ. Sci.*, 2011, **4**, 3680–3688.
4 M. D. Slater, D. Kim, E. Lee and C. S. Johnson, *Adv. Funct. Mater.*, 2013, **23**, 947–958.
5 A. Manthiram, Y. Fu, S. H. Chung, C. Zu and Y. S. Su, *Chem. Rev.*, 2014, **114**, 11751–11787.
6 J. Lu, L. Li, J. B. Park, Y. K. Sun, F. Wu and K. Amine, *Chem. Rev.*, 2014, **114**, 5611–5640.
7 H. Kim, D. A. Boysen, J. M. Newhouse, B. L. Spatocco, B. Chung, P. J. Burke, D. J. Bradwell, K. Jiang, A. A. Tomaszowska, K. Wang, W. Wei, L. A. Ortiz, S. A. Barriga, S. M. Poizeau and D. R. Sadoway, *Chem. Rev.*, 2013, **113**, 2075–2099.
8 S.-W. Kim, D.-H. Seo, X. Ma, G. Ceder and K. Kang, *Adv. Energy Mater.*, 2012, **2**, 710–721.
9 W. Luo, J.-J. Gaumet and L.-Q. Mai, *Rare Met.*, 2017, **36**, 321–338.
10 Q. Yang, J. Zhou, G. Zhang, C. Guo, M. Li, Y. Zhu and Y. Qian, *J. Mater. Chem. A*, 2017, **5**, 12144–12148.
11 Y. Xiao, J.-Y. Hwang, I. Belharouak and Y.-K. Sun, *Nano Energy*, 2017, **32**, 320–328.
12 M. Walter, T. Zund and M. V. Kovalenko, *Nanoscale*, 2015, **7**, 9158–9163.
13 S. Goriparti, E. Miele, F. De Angelis, E. Di Fabrizio, R. Proietti Zaccaria and C. Capiglia, *J. Power Sources*, 2014, **257**, 421–443.
14 D. Deng, *Energy Sci. Eng.*, 2015, **3**, 385–418.
15 Y. Wen, K. He, Y. Zhu, F. Han, Y. Xu, I. Matsuda, Y. Ishii, J. Cumings and C. Wang, *Nat. Commun.*, 2014, **5**, 4033.
16 Y. Xiao, S. H. Lee and Y.-K. Sun, *Adv. Energy Mater.*, 2017, **7**, 1601329.
17 Z. Liu, T. Lu, T. Song, X.-Y. Yu, X. W. Lou and U. Paik, *Energy Environ. Sci.*, 2017, **10**, 1576–1580.
18 J. Liu, Y. Wen, P. A. van Aken, J. Maier and Y. Yu, *Nano Lett.*, 2014, **14**, 6387–6392.
19 Z. Liu, X.-Y. Yu and U. Paik, *Adv. Energy Mater.*, 2016, **6**, 1502318.
20 Y. Wang, X. Guo, Z. Wang, M. Lü, B. Wu, Y. Wang, C. Yan, A. Yuan and H. Yang, *J. Mater. Chem. A*, 2017, **5**, 25562–25573.
21 F. Hu and T. Song, *RSC Adv.*, 2017, **7**, 54203–54212.
22 Z. Liu, T. Song, J. H. Kim, Z. Li, J. Xiang, T. Lu and U. Paik, *Electrochem. Commun.*, 2016, **72**, 91–95.
23 B. Zhao, R. Ran, M. Liu and Z. Shao, *Mater. Sci. Eng., R*, 2015, **98**, 1–71.
24 X. Hu, W. Zhang, X. Liu, Y. Mei and Y. Huang, *Chem. Soc. Rev.*, 2015, **44**, 2376–2404.
25 X. Xu, Z. Dou, E. Gu, L. Si, X. Zhou and J. Bao, *J. Mater. Chem. A*, 2017, **5**, 13411–13420.

26 J. L. Gómez-Cámer, C. Villevieille and P. Novák, *J. Mater. Chem. A*, 2013, **1**, 13011–13016.
27 X. Zhou, Z. Zhang, X. Lu, X. Lv, G. Ma, Q. Wang and Z. Lei, *ACS Appl. Mater. Interfaces*, 2017, **9**, 34927–34936.
28 Y. Lu, N. Zhang, S. Jiang, Y. Zhang, M. Zhou, Z. Tao, L. A. Archer and J. Chen, *Nano Lett.*, 2017, **17**, 3668–3674.
29 R. Jin, H. Jiang, Q. Wang, G. Li and S. Gao, *ACS Appl. Mater. Interfaces*, 2017, **9**, 44494–44502.
30 Q. Liu, Y. Yan, X. Chu, Y. Zhang, L. Xue and W. Zhang, *J. Mater. Chem. A*, 2017, **5**, 21328–21333.
31 J. Song, P. Yan, L. Luo, X. Qi, X. Rong, J. Zheng, B. Xiao, S. Feng, C. Wang, Y.-S. Hu, Y. Lin, V. L. Sprenkle and X. Li, *Nano Energy*, 2017, **40**, 504–511.
32 J. Li, J. Pu, Z. Liu, J. Wang, W. Wu, H. Zhang and H. Ma, *ACS Appl. Mater. Interfaces*, 2017, **9**, 25250–25256.
33 X. Zhou, Z. Zhang, X. Xu, J. Yan, G. Ma and Z. Lei, *ACS Appl. Mater. Interfaces*, 2016, **8**, 35398–35406.
34 J. Cui, S. Yao and J.-K. Kim, *Energy Storage Materials*, 2017, **7**, 64–114.
35 A. Darwiche, C. Marino, M. T. Sougrati, B. Fraisse, L. Stievano and L. Monconduit, *J. Am. Chem. Soc.*, 2012, **134**, 20805–20811.
36 M. He, K. Kravchyk, M. Walter and M. V. Kovalenko, *Nano Lett.*, 2014, **14**, 1255–1262.
37 R. Al-Salman, S. J. Sedlmaier, H. Sommer, T. Brezesinski and J. Janek, *J. Mater. Chem. A*, 2016, **4**, 12726–12729.
38 S. Liu, J. Feng, X. Bian, J. Liu and H. Xu, *Energy Environ. Sci.*, 2016, **9**, 1229–1236.
39 J. Wang, J. Yang, W. Yin and S.-i. Hirano, *J. Mater. Chem. A*, 2017, **5**, 20623–20630.
40 J. Xie, L. Liu, J. Xia, Y. Zhang, M. Li, Y. Ouyang, S. Nie and X. Wang, *Nano-Micro Lett.*, 2018, **10**, 12.
41 C. K. Chan, H. Peng, G. Liu, K. McIlwrath, X. F. Zhang, R. A. Huggins and Y. Cui, *Nat. Nanotechnol.*, 2008, **3**, 31–35.
42 A. Nie, L. Gan, Y. Cheng, X. Tao, Y. Yuan, S. Sharifi-Asl, K. He, H. Asayesh-Ardakani, V. Vasiraju, J. Lu, F. Mashayek, R. Klie, S. Vaddiraju, U. Schwingenschlogl and R. Shahbazian-Yassar, *Adv. Funct. Mater.*, 2016, **26**, 543–552.
43 C. Nithya and S. Gopukumar, *J. Mater. Chem. A*, 2014, **2**, 10516–10525.
44 J. Duan, W. Zhang, C. Wu, Q. Fan, W. Zhang, X. Hu and Y. Huang, *Nano Energy*, 2015, **16**, 479–487.
45 X. Zhou, X. Liu, Y. Xu, Y. Liu, Z. Dai and J. Bao, *J. Phys. Chem. C*, 2014, **118**, 23527–23534.
46 Y. M. Chen, L. Yu and X. W. Lou, *Angew. Chem., Int. Ed. Engl.*, 2016, **55**, 5990–5993.
47 D. Y. Yu, P. V. Prikhodchenko, C. W. Mason, S. K. Batabyal, J. Gun, S. Sladkevich, A. G. Medvedev and O. Lev, *Nat. Commun.*, 2013, **4**, 2922.
48 H. Li, H. Yin, K. Wang, S. Cheng, K. Jiang and D. R. Sadoway, *Adv. Energy Mater.*, 2016, **6**, 1600483.
49 K. Wang, K. Jiang, B. Chung, T. Ouchi, P. J. Burke, D. A. Boysen, D. J. Bradwell, H. Kim, U. Muecke and D. R. Sadoway, *Nature*, 2014, **514**, 348–350.
50 M. Walter, S. Doswald and M. V. Kovalenko, *J. Mater. Chem. A*, 2016, **4**, 7053–7059.
51 L. Wang, C. Wang, N. Zhang, F. Li, F. Cheng and J. Chen, *ACS Energy Lett.*, 2016, **2**, 256–262.
52 V. Renman, M. Valvo, C.-W. Tai, I. Zimmermann, M. Johnsson, C. Pay Gómez and K. Edström, *J. Phys. Chem. C*, 2017, **121**, 5949–5958.
53 Q. Sun, W.-J. Li and Z.-W. Fu, *Solid State Sci.*, 2010, **12**, 397–403.
54 L. Baggetto, P. Ganesh, C.-N. Sun, R. A. Meisner, T. A. Zawodzinski and G. M. Veith, *J. Mater. Chem. A*, 2013, **1**, 7985–7994.
55 N. Wang, Z. Bai, Y. Qian and J. Yang, *Adv. Mater.*, 2016, **28**, 4126–4133.
56 Z. Li, X. Tan, P. Li, P. Kalisvaart, M. T. Janish, W. M. Mook, E. J. Luber, K. L. Jungjohann, C. B. Carter and D. Mitlin, *Nano Lett.*, 2015, **15**, 6339–6348.
57 L. Simonin, U. Lafont and E. M. Kelder, *J. Power Sources*, 2008, **180**, 859–863.
58 Y. Zhao and A. Manthiram, *Chem. Mater.*, 2015, **27**, 3096–3101.
59 B. Farbod, K. Cui, W. P. Kalisvaart, M. Kupsta, B. Zahiri, A. Kohandehghan, E. M. Lotfabad, Z. Li, E. J. Luber and D. Mitlin, *ACS Nano*, 2014, **8**, 4415–4429.
60 L. Yu, J. Liu, X. Xu, L. Zhang, R. Hu, J. Liu, L. Yang and M. Zhu, *ACS Appl. Mater. Interfaces*, 2017, **9**, 2516–2525.
61 Y.-w. Yang, Y.-b. Chen, F. Liu, X.-y. Chen and Y.-c. Wu, *Electrochim. Acta*, 2011, **56**, 6420–6425.
62 E. Allcorn, S. O. Kim and A. Manthiram, *Phys. Chem. Chem. Phys.*, 2015, **17**, 28837–28843.
63 L. Baggetto, E. Allcorn, R. R. Unocic, A. Manthiram and G. M. Veith, *J. Mater. Chem. A*, 2013, **1**, 11163–11169.
64 L. Xiao, Y. Cao, J. Xiao, W. Wang, L. Kovarik, Z. Nie and J. Liu, *Chem. Commun.*, 2012, **48**, 3321–3323.
65 J. Liu, Z. Yang, J. Wang, L. Gu, J. Maier and Y. Yu, *Nano Energy*, 2015, **16**, 389–398.
66 D. Li, D. Yan, J. Ma, W. Qin, X. Zhang, T. Lu and L. Pan, *Ceram. Int.*, 2016, **42**, 15634–15642.
67 W. Luo, A. Calas, C. Tang, F. Li, L. Zhou and L. Mai, *ACS Appl. Mater. Interfaces*, 2016, **8**, 35219–35226.
68 S. Yao, J. Cui, Z. Lu, Z.-L. Xu, L. Qin, J. Huang, Z. Sadighi, F. Ciucci and J.-K. Kim, *Adv. Energy Mater.*, 2017, **7**, 1602149.
69 V. Renman, S. Hu, R. Eriksson, J. Maibach, M. Johnsson, C. Pay Gómez and K. Edström, *Chem. Mater.*, 2016, **28**, 6520–6527.
70 M. K. Devaraju and I. Honma, *Adv. Energy Mater.*, 2012, **2**, 284–297.
71 S. Qiu, X. Wu, L. Xiao, X. Ai, H. Yang and Y. Cao, *ACS Appl. Mater. Interfaces*, 2016, **8**, 1337–1343.
72 X. Zhou, Z. Zhang, J. Wang, Q. Wang, G. Ma and Z. Lei, *J. Alloys Compd.*, 2017, **699**, 611–618.
73 D. Y. Yu, H. E. Hoster and S. K. Batabyal, *Sci. Rep.*, 2014, **4**, 4562.
74 M. Roelsgaard, P. Norby, E. Eikeland, M. Sondergaard and B. B. Iversen, *Dalton Trans.*, 2016, **45**, 18994–19001.
75 J. Ma, X. Duan, J. Lian, T. Kim, P. Peng, X. Liu, Z. Liu, H. Li and W. Zheng, *Chem.–Eur. J.*, 2010, **16**, 13210–13217.
76 J. Xie, Y. Pei, L. Liu, S. Guo, J. Xia, M. Li, Y. Ouyang, X. Zhang and X. Wang, *Electrochim. Acta*, 2017, **254**, 246–254.

77 H. Hou, M. Jing, Z. Huang, Y. Yang, Y. Zhang, J. Chen, Z. Wu and X. Ji, *ACS Appl. Mater. Interfaces*, 2015, **7**, 19362–19369.
78 L. Ji, W. Zhou, V. Chabot, A. Yu and X. Xiao, *ACS Appl. Mater. Interfaces*, 2015, **7**, 24895–24901.
79 J. Liu, L. Yu, C. Wu, Y. Wen, K. Yin, F. K. Chiang, R. Hu, J. Liu, L. Sun, L. Gu, J. Maier, Y. Yu and M. Zhu, *Nano Lett.*, 2017, **17**, 2034–2042.
80 Z. Yi, Q. Han, P. Zan, Y. Wu, Y. Cheng and L. Wang, *J. Power Sources*, 2016, **331**, 16–21.
81 H. Hou, M. Jing, Y. Yang, Y. Zhu, L. Fang, W. Song, C. Pan, X. Yang and X. Ji, *ACS Appl. Mater. Interfaces*, 2014, **6**, 16189–16196.
82 Z. Yi, Q. Han, Y. Cheng, F. Wang, Y. Wu and L. Wang, *Electrochim. Acta*, 2016, **190**, 804–810.
83 S. Yoon and A. Manthiram, *Chem. Mater.*, 2009, **21**, 3898–3904.
84 M. T. Demko, S. Xun, S.-H. Kim, H. Liu, T. Mai, P. Nguyen, R. Featherer, X. Lin, S. Subramoney and K. Warrington, *Electrochim. Acta*, 2016, **217**, 292–298.
85 N. T. Hung, S.-H. Park, J. Bae, Y. S. Yoon, J. H. Kim, H. B. Son, D. Lee, I. T. Kim and J. Hur, *Electrochim. Acta*, 2016, **210**, 567–574.
86 C. S. Johnson, J. T. Vaughey, M. M. Thackeray, T. Sarakonsri, S. A. Hackney, L. Fransson, K. Edstrom and J. O. Thomas, *Electrochem. Commun.*, 2000, **2**, 595–600.
87 A. N. Jansen, J. A. Clevenger, A. M. Baebler and J. T. Vaughey, *J. Alloys Compd.*, 2011, **509**, 4457–4461.
88 M. V. Reddy, G. V. Subba Rao and B. V. R. Chowdari, *J. Mater. Chem.*, 2011, **21**, 10003–10011.
89 H. Honda, *J. Power Sources*, 2003, **123**, 216–221.
90 E. Allcorn, S.-O. Kim and A. Manthiram, *J. Power Sources*, 2015, **299**, 501–508.
91 L. Baggetto, E. Allcorn, A. Manthiram and G. M. Veith, *Electrochem. Commun.*, 2013, **27**, 168–171.
92 G. J. Jung, Y. Lee, Y. S. Mun, H. Kim, J. Hur, T. Y. Kim, K. S. Suh, J. H. Kim, D. Lee, W. Choi and I. T. Kim, *J. Power Sources*, 2017, **340**, 393–400.
93 C.-M. Park and H.-J. Sohn, *Electrochim. Acta*, 2009, **54**, 6367–6373.
94 J.-O. Lee, J.-U. Seo, J. H. Song, C.-M. Park and C. K. Lee, *Electrochem. Commun.*, 2013, **28**, 71–74.
95 I. T. Kim, E. Allcorn and A. Manthiram, *Phys. Chem. Chem. Phys.*, 2014, **16**, 12884–12889.
96 C.-C. Chang, *J. Power Sources*, 2008, **175**, 874–880.
97 A. K. Jibin, M. V. Reddy, G. V. Subba Rao, U. V. Varadaraju and B. V. R. Chowdari, *Electrochim. Acta*, 2012, **71**, 227–232.
98 E. Allcorn and A. Manthiram, *J. Electrochem. Soc.*, 2015, **162**, A1778–A1786.
99 E. McCalla, M. T. Sougrati, G. Rousse, E. J. Berg, A. Abakumov, N. Recham, K. Ramesha, M. Sathiya, R. Dominko, G. Van Tendeloo, P. Novak and J. M. Tarascon, *J. Am. Chem. Soc.*, 2015, **137**, 4804–4814.
100 C. Villevieille, C. M. Ionica-Bousquet, B. Ducourant, J. C. Jumas and L. Monconduit, *J. Power Sources*, 2007, **172**, 388–394.
101 J. T. Vaughey, L. Fransson, H. A. Swinger, K. Edström and M. M. Thackeray, *J. Power Sources*, 2003, **119–121**, 64–68.
102 C. Yang, W. Li, Z. Yang, L. Gu and Y. Yu, *Nano Energy*, 2015, **18**, 12–19.
103 J. Hassoun, G. Derrien, S. Panero and B. Scrosati, *J. Power Sources*, 2008, **183**, 339–343.
104 M. Kundu, S. Mahanty and R. N. Basu, *Mater. Lett.*, 2011, **65**, 1105–1107.
105 D. Yuan, X. Liang, L. Wu, Y. Cao, X. Ai, J. Feng and H. Yang, *Adv. Mater.*, 2014, **26**, 6301–6306.
106 Z. Liu, X.-Y. Yu, X. W. Lou and U. Paik, *Energy Environ. Sci.*, 2016, **9**, 2314–2318.
107 J. M. Mosby and A. L. Prieto, *J. Am. Chem. Soc.*, 2008, **130**, 10656–10661.
108 R. M. Gnanamuthu, Y. N. Jo and C. W. Lee, *Current Applied Physics*, 2013, **13**, 1454–1458.
109 H. Bryngelsson, J. Eskhult, K. Edström and L. Nyholm, *Electrochim. Acta*, 2007, **53**, 1062–1073.
110 S. Sengupta, A. Patra, Y. Deo, K. Das, S. B. Majumder and S. Das, *Metall. Mater. Trans. E*, 2017, **4**, 51–59.
111 C. Zhang, K.-Q. Xu, W. Zhou, X.-F. Lu, R.-Y. Li and G.-R. Li, *Part. Part. Syst. Charact.*, 2016, **33**, 553–559.
112 J. Yang, M. Winter and J. O. Besenhard, *Solid State Ionics*, 1996, **90**, 281–287.
113 E. D. Jackson, S. Green and A. L. Prieto, *ACS Appl. Mater. Interfaces*, 2015, **7**, 7447–7450.
114 K. S. Hong, D. H. Nam, S. J. Lim, D. Sohn, T. H. Kim and H. Kwon, *ACS Appl. Mater. Interfaces*, 2015, **7**, 17264–17271.
115 E. D. Jackson, S. Green and A. L. Prieto, *ACS Appl. Mater. Interfaces*, 2015, **7**, 7447–7450.
116 D.-H. Nam, K.-S. Hong, S.-J. Lim and H.-S. Kwon, *J. Power Sources*, 2014, **247**, 423–427.
117 H. Bryngelsson, J. Eskhult, L. Nyholm, M. Herranen, O. Alm and K. Edstrom, *Chem. Mater.*, 2007, **19**, 1170–1180.
118 L. Liang, Y. Xu, Y. Li, H. Dong, M. Zhou, H. Zhao, U. Kaiser and Y. Lei, *J. Mater. Chem. A*, 2017, **5**, 1749–1755.
119 C. W. Lee, J.-C. Kim, S. Park, H. J. Song and D.-W. Kim, *Nano Energy*, 2015, **15**, 479–489.
120 X. He, W. Pu, L. Wang, J. Ren, C. Jiang and C. Wan, *Electrochim. Acta*, 2007, **52**, 3651–3653.
121 Á. Caballero, J. Morales and L. Sánchez, *J. Power Sources*, 2008, **175**, 553–557.
122 H. Gao, W. Zhou, J.-H. Jang and J. B. Goodenough, *Adv. Energy Mater.*, 2016, **6**, 1502130.
123 X. Zhang, P. Li, R. Zang, S. Wang, Y. Zhu, C. Li and G. Wang, *Chem.–Asian J.*, 2017, **12**, 116–121.
124 H. Hou, M. Jing, Y. Yang, Y. Zhang, W. Song, X. Yang, J. Chen, Q. Chen and X. Ji, *J. Power Sources*, 2015, **284**, 227–235.
125 J. Pan, N. Wang, Y. Zhou, X. Yang, W. Zhou, Y. Qian and J. Yang, *Nano Res.*, 2017, **10**, 1794–1803.
126 G.-Z. Wang, J.-M. Feng, L. Dong, X.-F. Li and D.-J. Li, *J. Alloys Compd.*, 2017, **693**, 141–149.
127 N. E. Drewett, I. M. Aldous, J. Zou and L. J. Hardwick, *Electrochim. Acta*, 2017, **247**, 296–305.
128 L. Baggetto, H.-Y. Hah, J.-C. Jumas, C. E. Johnson, J. A. Johnson, J. K. Keum, C. A. Bridges and G. M. Veith, *J. Power Sources*, 2014, **267**, 329–336.

129 L. Baggetto, K. J. Carroll, H.-Y. Hah, C. E. Johnson, D. R. Mullins, R. R. Unocic, J. A. Johnson, Y. S. Meng and G. M. Veith, *J. Phys. Chem. C*, 2014, **118**, 7856–7864.
130 Q. Sun, Q.-Q. Ren, H. Li and Z.-W. Fu, *Electrochem. Commun.*, 2011, **13**, 1462–1464.
131 K. Shiva, H. B. Rajendra and A. J. Bhattacharyya, *ChemPlusChem*, 2015, **80**, 516–521.
132 H. Lv, S. Qiu, G. Lu, Y. Fu, X. Li, C. Hu and J. Liu, *Electrochim. Acta*, 2015, **151**, 214–221.
133 Y. S. Kim, W. B. Kim and Y. L. Joo, *J. Mater. Chem. A*, 2014, **2**, 8323–8327.
134 C. Chen, K. Fu, Y. Lu, J. Zhu, L. Xue, Y. Hu and X. Zhang, *RSC Adv.*, 2015, **5**, 30793–30800.
135 J.-C. Kim and D.-W. Kim, *Electrochem. Commun.*, 2014, **46**, 124–127.
136 Y. Zhu, X. Han, Y. Xu, Y. Liu, S. Zheng, K. Xu, L. Hu and C. Wang, *ACS Nano*, 2013, **7**, 6378–6386.
137 K. Li, D. Su, H. Liu and G. Wang, *Electrochim. Acta*, 2015, **177**, 304–309.
138 J. Li, K. Du, Y. Lai, Y. Chen and Z. Zhang, *J. Mater. Chem. A*, 2017, **5**, 10843–10848.
139 Q. Ru, X. Chen, J. Li, L. Guo and S. Hu, *Electrochim. Acta*, 2016, **193**, 180–190.
140 L. Shi, H. Li, Z. Wang, X. Huang and L. Chen, *J. Mater. Chem.*, 2001, **11**, 1502–1505.
141 D. Lakshmi and B. Nalini, *J. Solid State Electrochem.*, 2016, **21**, 1027–1034.
142 Y. Wang and J. Y. Lee, *Angew. Chem., Int. Ed. Engl.*, 2006, **45**, 7039–7042.
143 A. Birrozzi, F. Maroni, R. Raccichini, R. Tossici, R. Marassi and F. Nobili, *J. Power Sources*, 2015, **294**, 248–253.
144 J. Gu, Z. Du, C. Zhang, J. Ma, B. Li and S. Yang, *Adv. Energy Mater.*, 2017, **7**, 1700447.
145 W. Luo, P. Zhang, X. Wang, Q. Li, Y. Dong, J. Hua, L. Zhou and L. Mai, *J. Power Sources*, 2016, **304**, 340–345.
146 N. Zhang, Y. Liu, Y. Lu, X. Han, F. Cheng and J. Chen, *Nano Res.*, 2015, **8**, 3384–3393.
147 Y. Yang, X. Yang, Y. Zhang, H. Hou, M. Jing, Y. Zhu, L. Fang, Q. Chen and X. Ji, *J. Power Sources*, 2015, **282**, 358–367.
148 V. G. Pol, J. Wen, D. J. Miller and M. M. Thackeray, *J. Electrochem. Soc.*, 2014, **161**, A777–A782.
149 Y. Zhu, P. Nie, L. Shen, S. Dong, Q. Sheng, H. Li, H. Luo and X. Zhang, *Nanoscale*, 2015, **7**, 3309–3315.
150 S. Fan, T. Sun, X. Rui, Q. Yan and H. H. Hng, *J. Power Sources*, 2012, **201**, 288–293.
151 M. V. Reddy, V. H. Khai and B. V. R. Chowdari, *Solid State Ionics*, 2014, **268**, 277–281.
152 N. Wang, Z. Bai, Y. Qian and J. Yang, *ACS Appl. Mater. Interfaces*, 2017, **9**, 447–454.
153 L. Hu, X. Zhu, Y. Du, Y. Li, X. Zhou and J. Bao, *Chem. Mater.*, 2015, **27**, 8138–8145.
154 N. Li, S. Liao, Y. Sun, H. W. Song and C. X. Wang, *J. Mater. Chem. A*, 2015, **3**, 5820–5828.
155 Y. Zhang, J. Xie, T. Zhu, G. Cao, X. Zhao and S. Zhang, *J. Power Sources*, 2014, **247**, 204–212.
156 J. Ma, Y. Wang, Y. Wang, Q. Chen, J. Lian and W. Zheng, *J. Phys. Chem. C*, 2009, **113**, 13588–13592.
157 G.-Z. Wang, J.-M. Feng, L. Dong, X.-F. Li and D.-J. Li, *Electrochim. Acta*, 2017, **240**, 203–214.
158 L. Nie, J. Xie, G. Liu, S. Hao, Z. J. Xu, R. Xu and Q. Zhang, *J. Mater. Chem. A*, 2017, **5**, 14198–14205.
159 P. V. Prikhodchenko, J. Gun, S. Sladkevich, A. A. Mikhaylov, O. Lev, Y. Y. Tay, S. K. Batabyal and D. Y. W. Yu, *Chem. Mater.*, 2012, **24**, 4750–4757.
160 C.-M. Park and H.-J. Sohn, *J. Electrochem. Soc.*, 2010, **157**, A46–A49.
161 T. Yang, H. Wang, J. Xu, L. Wang, W.-C. Song, Y. Mao and J. Ma, *RSC Adv.*, 2016, **6**, 78959–78962.
162 N. Twu, M. Metzger, M. Balasubramanian, C. Marino, X. Li, H. Chen, H. Gasteiger and G. Ceder, *Chem. Mater.*, 2017, **29**, 2584–2593.
163 X. Ma, K. Kang, G. Ceder and Y. S. Meng, *J. Power Sources*, 2007, **173**, 550–555.
164 N. Twu, X. Li, A. Urban, M. Balasubramanian, J. Lee, L. Liu and G. Ceder, *Nano Lett.*, 2015, **15**, 596–602.
165 C. C. H. Tran, C. Autret, C. Damas, B. Claude-Montigny and J. Santos-Peña, *Electrochim. Acta*, 2015, **182**, 11–19.
166 X. Xu, L. Si, X. Zhou, F. Tu, X. Zhu and J. Bao, *J. Power Sources*, 2017, **349**, 37–44.
167 W. Li, K. Wang, S. Cheng and K. Jiang, *J. Mater. Chem. A*, 2017, **5**, 1160–1167.
168 X. Liu, Y. Du, X. Xu, X. Zhou, Z. Dai and J. Bao, *J. Phys. Chem. C*, 2016, **120**, 3214–3220.
169 Y. Cheng, Z. Yi, C. Wang, L. Wang, Y. Wu and L. Wang, *Chem.–Asian J.*, 2016, **11**, 2173–2180.
170 Z. Yi, Q. Han, S. Ju, Y. Wu, Y. Cheng and L. Wang, *J. Electrochem. Soc.*, 2016, **163**, A2641–A2646.
171 C. Yang, W. Li, Z. Yang, L. Gu and Y. Yu, *Nano Energy*, 2015, **18**, 12–19.
172 C.-M. Park and H.-J. Sohn, *Chem. Mater.*, 2008, **20**, 3169–3173.
173 C.-M. Park, S. Yoon, S.-I. Lee, J.-H. Kim, J.-H. Jung and H.-J. Sohn, *J. Electrochem. Soc.*, 2007, **154**, A917–A920.
174 E. Allcorn and A. Manthiram, *J. Phys. Chem. C*, 2014, **118**, 811–822.
175 Y. S. Mun, Y. Yoon, J. Hur, M. S. Park, J. Bae, J. H. Kim, Y. S. Yoon, I. S. Yoo, S. G. Lee and I. T. Kim, *J. Power Sources*, 2017, **362**, 115–122.
176 A. Dailly, J. Ghanbaja, P. Willmann and D. Billaud, *Electrochim. Acta*, 2003, **48**, 977–984.
177 P. Zhang, Y. Wang, J. Wang, D. Zhang, X. Ren and Q. Yuan, *Electrochim. Acta*, 2014, **137**, 121–130.
178 F. Wan, J. Z. Guo, X. H. Zhang, J. P. Zhang, H. Z. Sun, Q. Yan, D. X. Han, L. Niu and X. L. Wu, *ACS Appl. Mater. Interfaces*, 2016, **8**, 7790–7799.
179 T. Wu, H. Hou, C. Zhang, P. Ge, Z. Huang, M. Jing, X. Qiu and X. Ji, *ACS Appl. Mater. Interfaces*, 2017, **9**, 26118–26125.
180 Y. Yi, H.-W. Shim, S.-D. Seo, M. A. Dar and D.-W. Kim, *Mater. Res. Bull.*, 2016, **76**, 338–343.
181 M. Walter, R. Erni and M. V. Kovalenko, *Sci. Rep.*, 2015, **5**, 8418.
182 H. Hou, M. Jing, Y. Zhang, J. Chen, Z. Huang and X. Ji, *J. Mater. Chem. A*, 2015, **3**, 17549–17552.

183 S. Sengupta, A. Patra, M. Akhtar, K. Das, S. B. Majumder and S. Das, *J. Alloys Compd.*, 2017, **705**, 290–300.
184 C. Chen, G. Li, J. Zhu, Y. Lu, M. Jiang, Y. Hu, Z. Shen and X. Zhang, *Carbon*, 2017, **120**, 380–391.
185 M.-Z. Xue and Z.-W. Fu, *Electrochem. Commun.*, 2006, **8**, 1250–1256.
186 M.-Z. Xue and Z.-W. Fu, *J. Alloys Compd.*, 2008, **458**, 351–356.
187 Y. Pan, X.-J. Wu, Z.-Q. Zhang, Z.-W. Fu and Y.-N. Zhou, *J. Alloys Compd.*, 2017, **714**, 348–355.
188 X. Zhou, Y. Zhong, M. Yang, M. Hu, J. Wei and Z. Zhou, *Chem. Commun.*, 2014, **50**, 12888–12891.
189 C. Hwang, S. Choi, G. Y. Jung, J. Yang, S. K. Kwak, S. Park and H.-K. Song, *Electrochim. Acta*, 2017, **252**, 25–32.
190 L. Simonin, U. Lafont, N. Tabrizi, A. Schmidt-Ott and E. M. Kelder, *J. Power Sources*, 2007, **174**, 805–809.
191 L. Wu, X. Hu, J. Qian, F. Pei, F. Wu, R. Mao, X. Ai, H. Yang and Y. Cao, *Energy Environ. Sci.*, 2014, **7**, 323–328.
192 J.-H. Choi, C.-W. Ha, H.-Y. Choi, H.-C. Shin and S.-M. Lee, *Mater. Lett.*, 2015, **159**, 349–352.
193 S. Y. Son, D. Lee, J. Hur and I. T. Kim, *J. Nanosci. Nanotechnol.*, 2017, **17**, 7575–7578.
194 C. M. Park and H. J. Sohn, *Adv. Mater.*, 2010, **22**, 47–52.
195 J. Han, M. Xu, M. Jia and T. Liu, *Ceram. Int.*, 2016, **42**, 14782–14787.
196 D. Larcher, A. S. Prakash, L. Laffont, M. Womes, J. C. Jumas, J. Olivier-Fourcade, M. S. Hedge and J.-M. Tarascon, *J. Electrochem. Soc.*, 2006, **153**, A1778–A1787.
197 Z. Yi, Q. Han, X. Li, Y. Wu, Y. Cheng and L. Wang, *Chem. Eng. J.*, 2017, **315**, 101–107.
198 C. Yan, G. Chen, D. Chen, J. Pei, J. Sun, H. Xu, Y. Zhang and Z. Qiu, *CrystEngComm*, 2014, **16**, 7753–7760.
199 Z. Yang, J. Sun, Y. Ni, Z. Zhao, J. Bao and S. Chen, *Energy Storage Materials*, 2017, **9**, 214–220.
200 L. Monconduit, J. C. Jumas, R. Alcantara, J. L. Tirado and C. P. Vicente, *J. Power Sources*, 2002, **107**, 74–79.
201 J. Santos Peña, J. Cuart Pascual, A. Caballero, J. Morales and L. Sánchez, *J. Solid State Chem.*, 2004, **177**, 2920–2927.
202 Y. Lin, W. Feng, Z. Li, T. Xu and H. Fei, *Ionics*, 2017, **23**, 3197–3202.
203 M. Kundu, S. Mahanty and R. N. Basu, *Mater. Lett.*, 2011, **65**, 3083–3085.
204 K. P. Lakshmi, K. J. Janas and M. M. Shaijumon, *Carbon*, 2018, **131**, 86–93.
205 P. Li, J. Shu, L. Shao, X. Lin, K. Wu, M. Shui, D. Wang, N. Long and Y. Ren, *J. Electroanal. Chem.*, 2014, **731**, 128–132.
206 L. Nie, Y. Zhang, W.-W. Xiong, T.-T. Lim, R. Xu, Q. Yan and Q. Zhang, *Inorg. Chem. Front.*, 2016, **3**, 111–116.
207 Y. Huang, C. Ji, Q. Pan, X. Zhang, J. Zhang, H. Wang, T. Liao and Q. Li, *J. Alloys Compd.*, 2017, **728**, 1139–1145.
208 K. C. Hewitt, L. Y. Beaulieu and J. R. Dahn, *J. Electrochem. Soc.*, 2001, **148**, A402–A410.
209 P. Cui, Y. Liang, D. Zhan, Y. Zhao and R. Peng, *RSC Adv.*, 2014, **4**, 43821–43827.
210 D. J. Bradwell, H. Kim, A. H. Sirk and D. R. Sadoway, *J. Am. Chem. Soc.*, 2012, **134**, 1895–1897.
211 P. Leung, S. C. Heck, T. Amietszajew, M. R. Mohamed, M. B. Conde, R. J. Dashwood and R. Bhagat, *RSC Adv.*, 2015, **5**, 83096–83105.
212 T. Ouchi, H. Kim, B. L. Spatocco and D. R. Sadoway, *Nat. Commun.*, 2016, **7**, 10999.
213 T. Ouchi and D. R. Sadoway, *J. Power Sources*, 2017, **357**, 158–163.
214 X. Ning, S. Phadke, B. Chung, H. Yin, P. Burke and D. R. Sadoway, *J. Power Sources*, 2015, **275**, 370–376.
215 B. L. Spatocco, T. Ouchi, G. Lambotte, P. J. Burke and D. R. Sadoway, *J. Electrochem. Soc.*, 2015, **162**, A2729–A2736.
216 M. M. Kane, J. M. Newhouse and D. R. Sadoway, *J. Electrochem. Soc.*, 2014, **162**, A421–A425.
217 T. Ouchi, H. Kim, X. Ning and D. R. Sadoway, *J. Electrochem. Soc.*, 2014, **161**, A1898–A1904.
218 H. Li, K. Wang, S. Cheng and K. Jiang, *ACS Appl. Mater. Interfaces*, 2016, **8**, 12830–12835.
219 J. Kim, D. Shin, Y. Jung, S. M. Hwang, T. Song, Y. Kim and U. Paik, *J. Power Sources*, 2018, **377**, 87–92.